

Molecular simulations of capped nanocrystals

PROEFSCHRIFT

ter verkrijging van de graad van doctor
aan de Technische Universiteit Delft,
op gezag van de Rector Magnificus prof. ir. K.C.A.M. Luyben,
voorzitter van het College voor Promoties,
in het openbaar te verdedigen
op dinsdag 26 januari 2010 om 10.00 uur
door

Philipp Zinov'evič SCHAPOTSCHNIKOW

Diplom-Mathematiker (Technische Universität München),
Master of Philosophy (University of Wales)

geboren te Odessa (Oekraïne).

Dit proefschrift is goedgekeurd door de promotoren:

Prof. Dr.-Ing. J. Gross, promotor
Copromotor: Dr. ir. T.J.H Vlugt

Samenstelling promotiecommissie:

Rector Magnificus	voorzitter
Prof. Dr.-Ing. J. Gross	Technische Universiteit Delft, promotor
Dr. ir. T.J.H. Vlugt	Technische Universiteit Delft, copromotor
Prof. dr. D.N. Theodorou	National Technical University of Athens
Prof. dr. P.G. Bolhuis	Universiteit van Amsterdam
Prof. dr. D.A.M. Vanmaekelbergh	Universiteit Utrecht
Prof. dr. J.P.M. van der Eerden	Universiteit Utrecht
Prof. dr. ir. M.T. Kreutzer	Technische Universiteit Delft

The research reported in this thesis was carried out with financial support by the Netherlands Organization for Scientific Research (NWO).

Copyright © 2009 by P. Schapotschnikow

ISBN 978-90-8891-139-2

Typeset by the Author using the L^AT_EX Documentation System. Simulation snapshots were generated using the Visual Molecular Dynamics (VMD) package, available at www.ks.uiuc.edu/research/vmd. Graphs were produced using xmgrace (plasma-gate.weizmann.ac.il/grace).

Cover design by Anna Krylova (www.annakrylova.nl). Cover image is taken from www.tpicks.com. Quotations on the reverse side originate from anonymous referee reports.

Printed by: Proefschriftmaken.nl || Printyourthesis.com
Published by: Uitgeverij BOXPress, Oisterwijk

The Author can be contacted by email: schapotschnikow@gmx.de

Contents

1	Introduction	1
1.1	Nanocrystals as building blocks in nanotechnology	1
1.1.1	The role of organic ligands during synthesis	3
1.1.2	Nanocrystal self-assembly	4
1.2	Modeling and scales	7
1.2.1	Simulation studies of nanocrystals	11
1.3	Molecular simulation techniques	14
1.3.1	The coupling principle	14
1.3.2	Monte Carlo	15
1.3.3	Molecular Dynamics	24
1.4	Scope and outline	26
2	Monolayers of Alkylthiols on Gold Surfaces	29
2.1	Introduction	29
2.2	Molecular model	32
2.2.1	Au-S and Au-C interactions	32
2.3	Coarse-grained model for gold nanocrystals with an organic capping layer	34
2.4	Monte Carlo simulations	39
2.4.1	Biased insertion technique	41
2.4.2	Adsorption isotherm scaling	42
2.5	Adsorption of alkylthiols to Au NCs and to Au (111) surfaces	43
2.6	The structure of the capping layer	51
2.6.1	Systems in vacuum; chain melting	51
2.6.2	Systems with explicit solvent	54
2.6.3	Comparison of the coarse-grained and the full-atom models	58
2.7	Selective adsorption to Au NCs and Au (111) surfaces	60
2.8	Conclusions	63
3	Adsorption of Ligands to CdSe Nanocrystals	65
3.1	Introduction	65
3.2	Interaction model	67

3.3	Methods	69
3.3.1	Molecular Dynamics simulations	69
3.3.2	Monte Carlo simulations	69
3.3.3	Nanocrystal preparation	69
3.4	Binding of ligands follows from electrostatic interactions	71
3.5	Adsorption of alkylamines in two steps	76
3.6	Conclusions	82
4	Interactions between Capped Nanocrystals	83
4.1	Introduction	83
4.2	Model and methods	85
4.2.1	Potential of mean force	85
4.2.2	Sample preparation	88
4.2.3	Comparison of methods	89
4.3	Pair interactions and the Golden Rule	91
4.3.1	Parameterization of effective NC pair interactions	97
4.3.2	Shape memory effects	98
4.3.3	The trouble with coarse-grained NCs	100
4.4	Three-body effects	101
4.4.1	Parameterization of triplet interactions	108
4.5	Equilibrium distance by optimal packing	109
4.5.1	Implications for ligand design	115
4.6	Effective interaction in a good solvent	116
4.7	Conclusions	117
	Abbreviations	119
	References	121
	Summary	131
	Samenvatting	135
	Acknowledgments	141
	Curriculum Vitae	143

Chapter 1

Introduction

1.1 Nanocrystals as building blocks in nanotechnology

The engineering of materials on the nanometer (10^{-9} m) scale is generating much excitement in modern electronics, optics, catalysis, ceramics, magnetic storage, and biophysics.^{1–5} There are several reasons for this development. Modern imaging techniques allow to visualize objects that are too small to be recognized by conventional light microscopy (whose resolution is limited the wavelength of visible light: 380–750 nm).⁶ Having the possibility to visualize these entities, synthetic chemistry has made large advances toward manufacturing of nanomaterials with desired size and shape.^{7–19} Availability of a large new class of materials naturally stimulates scientific curiosity. On the other hand, the ongoing miniaturization of electronic and mechanical devices (Moore’s law) creates demand for low-cost high-quality nanosized functional elements.²⁰

Important classes of nanomaterials with special size- and shape dependent optical and electrical functionality include metal- and semiconductor crystallites of 2 – 10 nm size (see Fig. 1.1). These crystallites are called *nanocrystals (NCs)*; semiconductor NCs are also called *quantum dots (QDs)*. NCs and QDs have exciting quantum mechanical properties that are absent in bulk materials.²¹ Electrons and electron-hole pairs may “jump” between a QD and an adjacent object.^{22,23} This makes them promising materials for improving efficiency of solar cells and for creating novel electronic devices.^{24,25} In metallic NCs, the oscillation of electrons with respect to the atomic lattice generates unusual optical properties.²⁶ For example, the colour of gold particles changes with decreasing size from metallic over green to red. This effect has been known since ancient times, when it was applied to stain glass.²⁷ Another important finite-size phenomenon is the so called Surface-Enhanced Raman Scattering (SERS): gigantic increase of Raman scattering upon adsorption of certain molecules to the surface of a metallic NC. This

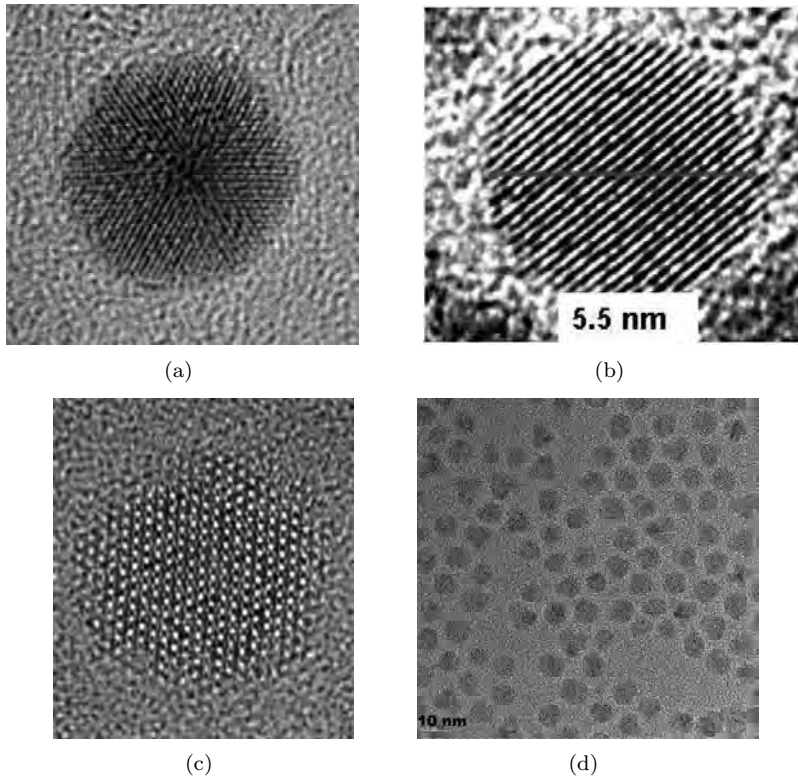


Figure 1.1: High-resolution (HR) transmission electron microscope (TEM) images of gold and CdSe nanocrystals. Organic molecules on the NC surface are not visible because they are transparent to the electron beam. (a) Gold NC (6 nm diameter). (b) Gold NC (5.5 nm diameter). The alternating light and dark lines are atomic planes. (c) CdSe NC (8 nm diameter). Bright dots and darker dots between them are columns of cadmium and selenium atoms, respectively. (d) TEM image of an array of as-synthesized CdSe NCs. Figures (a, c, d) are courtesy of Dr. M. van Huis (Delft University of Technology); Figure (b) is courtesy of Prof. H. M. Jaeger (University of Chicago).

effect makes gold NCs promising for highly sensitive molecular recognition.^{26,28} Due to the very high surface-to-volume ratio, noble metal NCs are promising for catalysis. For example, one of the main factors determining costs and efficiency of fuel cells is nowadays the platinum catalyst, which is needed for the dissociation of hydrogen into protons and electrons.²⁹⁻³¹ It is not surprising that one aims to replace the traditional solid catalyst by platinum NCs to obtain the same effective surface using less of this expensive material.³¹ Another, very recent development is the fabrication of free-standing ultrathin elastic sheets and membranes from NCs.³²⁻³⁴ Practical applications of these new objects have yet to be explored.

1.1.1 The role of organic ligands during synthesis

Due to advances in colloidal synthesis, it is possible to fabricate NCs in a large range of sizes and shapes with a high yield and selectivity.³⁵⁻³⁷ This approach is both elegant and relatively inexpensive as it requires the conventional chemical equipment only. Alternatively, nanosized objects can be produced from bulk materials through a variety of “top-down” techniques,¹⁶⁻¹⁹ which will not be discussed in this work.

Gold NCs are typically produced by the colloidal two-phase synthesis from Ref.³⁸ or a modification thereof.³⁹⁻⁴⁵ First, a gold salt is dissolved in the water phase and an alkylthiol surfactant is dissolved in the oil phase. A phase transfer agent is present: a compound that is soluble in both solvents, and that coordinates weakly to atomic gold (e.g., an alkylammonium salt such as CTAB). Second, the two-phase system is stirred to create an emulsion and thus a large oil-water interface. Third, a water-soluble reducing agent is added. The reduction reaction changes gold ions into elemental gold atoms, and the phase transfer agent acts as a shuttle bringing them into the oil phase. In the oil phase, gold atoms aggregate very quickly into small crystalline nuclei, and simultaneously alkylthiols attach to these nuclei via the strong gold-sulfur bond.⁴⁶ When eventually the entire surface of the nuclei is covered by surfactant molecules, they cannot grow further; for this reason, the method is also called *arrested precipitation*. In this way, one obtains alkylthiol capped gold NCs dispersed in the oil phase. The desired (average) NC size can be obtained by tuning the concentration and the tail length of the alkylthiol. The original synthesis procedure yields a relatively high polydispersity in size (40%), but it can be improved significantly using size-specific centrifugation.⁴⁷⁻⁴⁹ Nowadays, due to advances in the synthesis procedure the polydispersity is typically below 5%.^{15,37}

The synthesis of semiconductor QDs is usually performed in the oil phase using a combination of different ligands.^{35,50-52} This is necessary to (1) dissolve the (charged) anions and cations in the oil phase and (2) control the growth of the nuclei. The chemistry of this process is very complicated as many elementary reactions happen at the same time. The full mechanism of QD formation is far from being understood, and only few recent reports shed some light on this complex process.^{53,54} Moreover, the synthesis of QDs is extremely sensitive to

impurities in the reaction mixture.^{55–57}

There is a fundamental novelty in these recent methods compared to earlier synthesis protocols (starting with the work of M. Faraday⁵⁸). Gold particles synthesized without strongly bound capping molecules are not thermodynamically stable: they have a tendency to slowly but irreversibly agglomerate and flocculate, and once the solvent is removed, the gold particles cannot be redispersed.^{59,60} By contrast, alkylthiol capped NCs are stable for months and years in an organic solvent; and they can be redispersed after drying.^{38,48,49} Therefore, capped NCs behave in a certain sense like large molecules. The capping layer has a large impact on surface properties of NCs and their interactions with the surrounding. Understanding of these interactions is necessary for an efficient integration of NCs into novel materials and devices.

1.1.2 Nanocrystal self-assembly

Nanocrystals can form stable two- and three dimensional superlattices (also called NC films/solids or supra-crystals) with sizes typically in the order of $1\ \mu\text{m}$ – $1\ \text{mm}$,^{32,49,61–72} see Fig. 1.2. The 3D supra-crystals form readily upon solvent evaporation by self-assembly. The Langmuir-Blodgett technique is an excellent tool to fabricate high-quality monolayers of NCs at the air-water interface.^{62,63,73} The optical, electronic and mechanical properties of the NC supra-crystals are different from both individual NCs and the bulk material due to the close vicinity of NCs combined with a high periodicity.^{26,28,69,72} Thus, NC self-assembly is a promising way of creating solids with tailored mechanical and electronic properties. For example, gold and silver NCs films behave either like electric insulators or like metals depending of the interparticle spacing,^{74,75} while the corresponding 3D-structures behave like metals.^{23,66} Periodic arrays made from magnetic NC are promising for data storage application.^{76–78} A large variety of structures is found in binary systems, i.e. systems with NCs of two different sizes and/or materials,^{49,68–71} see Fig. 1.2(c). These binary superstructures are promising because their electronic properties are often superior compared to those of single component structures.^{69,79} It should be noted that fabrication of defect-free large-scale (order of cm) NC supra-crystals remains an open challenge.⁷²

Spontaneous formation of ordered structures is well-known for micron size colloidal particles. For example, it has been shown first in computer simulations⁸⁰ and later in experiments⁸¹ that monodisperse hard spheres form a close-packed crystal at a certain density. As there is no interaction energy in a hard sphere system, the entropy is higher in the ordered crystal than in a disordered fluid above the freezing density. This crucial discovery demonstrates that entropy maximization may lead to self-organization. A large variety of crystal structures can be formed in a binary colloidal system.^{82–84} If the size ratio and interactions are known exactly, the free energies of the possible colloidal crystal structures can be calculated using computer simulations;⁸⁵ and the structure with the lowest free energy is then expected to form. Such calculations are particularly useful

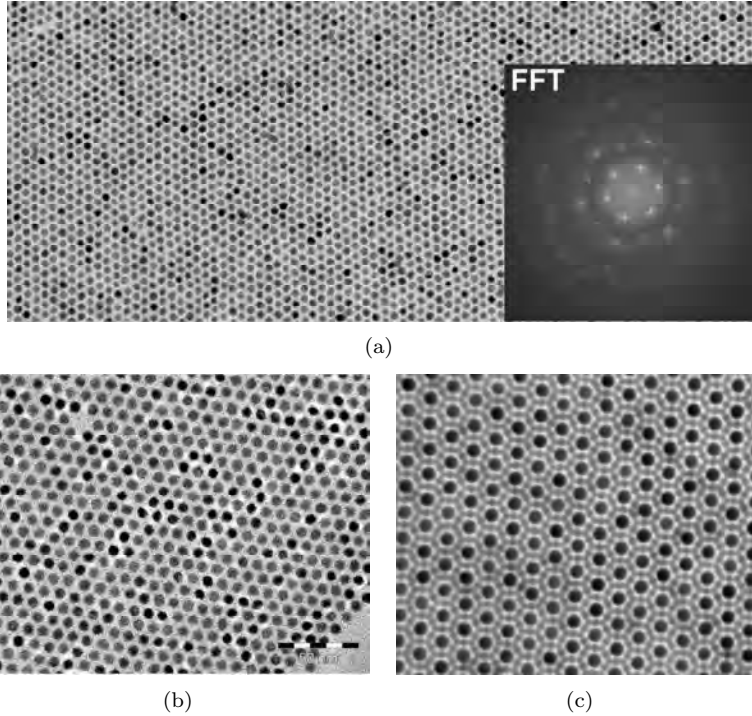


Figure 1.2: TEM images of self-assembled nanocrystal superlattices. The capping layers are not visible. (a) A close-packed monolayer of capped gold NCs (≈ 5 nm diameter). The different shades of the particles originate from different orientations of their atomic planes with respect to the incident electron beam. The inset shows the Fourier transform of the image; the large number of sharp bright dots indicates very high periodicity. Courtesy of H. M. Jaeger (University of Chicago). (b) A close-packed layer of PbSe NCs (≈ 8 nm diameter). Courtesy of Dr. R. Koole (Utrecht University, Philips). (c) Binary superlattice from 8 nm PbSe NCs and 3 nm CdSe NCs. Projection of different stacks of smaller NCs results in a honeycomb around the isolated stacks of larger NCs. The crystal structure is, coincidentally, identical to the one of the alloy CaCu_5 . Courtesy of W. Evers (Utrecht University).

when the interactions can be manipulated in the experiment, as the free energy of these systems is sensitive to the size ratio and interactions. It is then possible to find computationally the necessary conditions for the formation of a desired crystal structure. This approach was demonstrated in Refs.^{86,87} Different crystal structures were predicted first by computer simulation for various values of size and charge in the binary colloidal system. Based on these simulations, electrostatic interactions and size ratio were tuned in experiment and a large number of predicted structures could be obtained.

The work in Refs.^{86,87} is an important step towards rationally guided colloidal self-assembly. In the same way, the knowledge of interactions between NCs would allow a rational, computer-aided design of NC superstructures with desired properties. Unfortunately, most interaction models available for colloids of μm size are not sufficient for 10–100 times smaller NCs, so that the understanding of interactions between NCs is still limited. Due to the “large” size, both the interior of a colloidal particle and the solvent are treated as a bulk continuum during the derivation of theoretical interaction models.^{88,89} However, these approximations have limited validity for NCs, as atomistic and molecular details become important in this case. A large fraction of NC atoms lies at the surface or directly underneath it, which makes the concept of a “bulk NC interior” questionable. Moreover, organic solvent and ligand molecules are typically not much smaller than NCs. For example, if a 1 μm colloidal particle has a 2 nm thick capping layer which does not exhibit significant interactions, then this layer can often be neglected due to its very small size. By contrast, neglecting a 2 nm thick capping layer on a 5 nm small NC would yield a rather incomplete description.

There is another subtle difference between large colloidal particles and NCs, which is often overlooked. The thermal motion of colloids is mainly due to random collisions with solvent molecules (“Brownian motion”),^{59,90} while NCs are small enough to experience some thermal motion by themselves. We illustrate the difference by comparing the effects of thermal motion and Earth gravity on “free” particles. Consider for example a 3.7 nm gold NC Au_{1415} . Its mean thermal velocity is 0.023 m/s at room temperature (calculated from the Maxwell-Boltzmann distribution⁹⁰). This is huge compared to the small size of the NC. With this speed, it would travel the distance equal to its diameter within 164.2 ns. For comparison: during the same time, this NC would fall by 1.3×10^{-13} m due to gravity, which is 0.000035 times its size. Consider now a 100 times larger colloidal gold particle. Its thermal velocity is then 2.3×10^{-5} m/s, which is $100^{3/2} = 1000$ times smaller than that of a NC. At this speed, it would need 16.4 ms to travel the distance equal to its diameter. Within this time, the colloidal particle would fall by 1.3 mm, which is 3500 times its size. As we can see, the factor 100 in size between nanoparticles and typical colloidal particles can drastically alter their behaviour.

This example shows that once the solvent is evaporated, a colloidal crystal (or a disordered precipitate) behaves physically like a stack of balls. Depending on the colloidal interactions, these “balls” may be hard, soft, charged, “sticky” etc. Since

the thermal motion of a large particle inside a dry colloidal crystal is negligible, the physical description of a dry colloidal crystal falls entirely into the field of classical mechanics. On the other hand, a NC inside a dry NC supra-crystal still experiences relevant thermal motion, and its behaviour is similar to the one of an atomic crystal. In this case, one has to consider both the thermodynamic properties of a NC superlattice with and without solvent. To produce large-scale high-quality NC superlattices, it is therefore crucial to achieve thermodynamic stability of these superstructures both in the “wet” and in the “dry” state.

1.2 Modeling and scales

Modeling is a substantial part of the scientific approach to study real-life phenomena. In order to systematize observations and make predictions, one needs to recognize a pattern in a given set of data. Next, one tries to “understand” or “explain” this pattern. This is done by formulating an abstract mathematical and/or symbolic model, which can be embedded in an established theory. Once this has been achieved, the underlying theory provides formalisms for extrapolating the observed pattern to arbitrary situations. In many cases, these formalisms are extremely complex. At this point, computer simulations come into play. Computer simulations can be used to both demonstrate that the proposed model actually puts the pattern into the framework of a theory (“understand”) and to make predictions based on the model and the theory (“extrapolate”).

One of the central goals of material science is to describe macroscopic properties as a result of microscopic phenomena, and therefore bridge the gap between atomic or molecular properties and bulk materials. The size of this gap is given by the Avogadro Number $N_{\text{AV}} \approx 6.02 \times 10^{23}$ molecules/mol, which is the number of atoms in 12.00 g of carbon (which corresponds to the number of molecules in 22.4 l of air at ambient conditions). In very few cases, such a huge gap can be bridged in one single step. Most if not all models are unable to describe properties of a system with N_{AV} particles explicitly due to limited computing power. Therefore, one has to introduce model systems on different intermediate size scales. These model systems represent the inevitable compromise between system size and the level of detail, as the length and time scales are limited by the available computing power. Although large objects in the real world are usually modelled using macroscopic models based on continuous representation of matter, the microscopic details are always manifested in the material properties. For example, the behaviour of fluids is often studied using computational fluid dynamics (CFD).⁹¹ The microscopic properties of the fluid are then manifested in the CFD input parameters such as density, compressibility or viscosity, which can all be obtained from microscopic simulations. Fig. 1.3 shows the hierarchy of various models and methods in computational materials science. In the following, common microscopic models are briefly described.

The highest level of detail is achieved in quantum chemical calculations, such

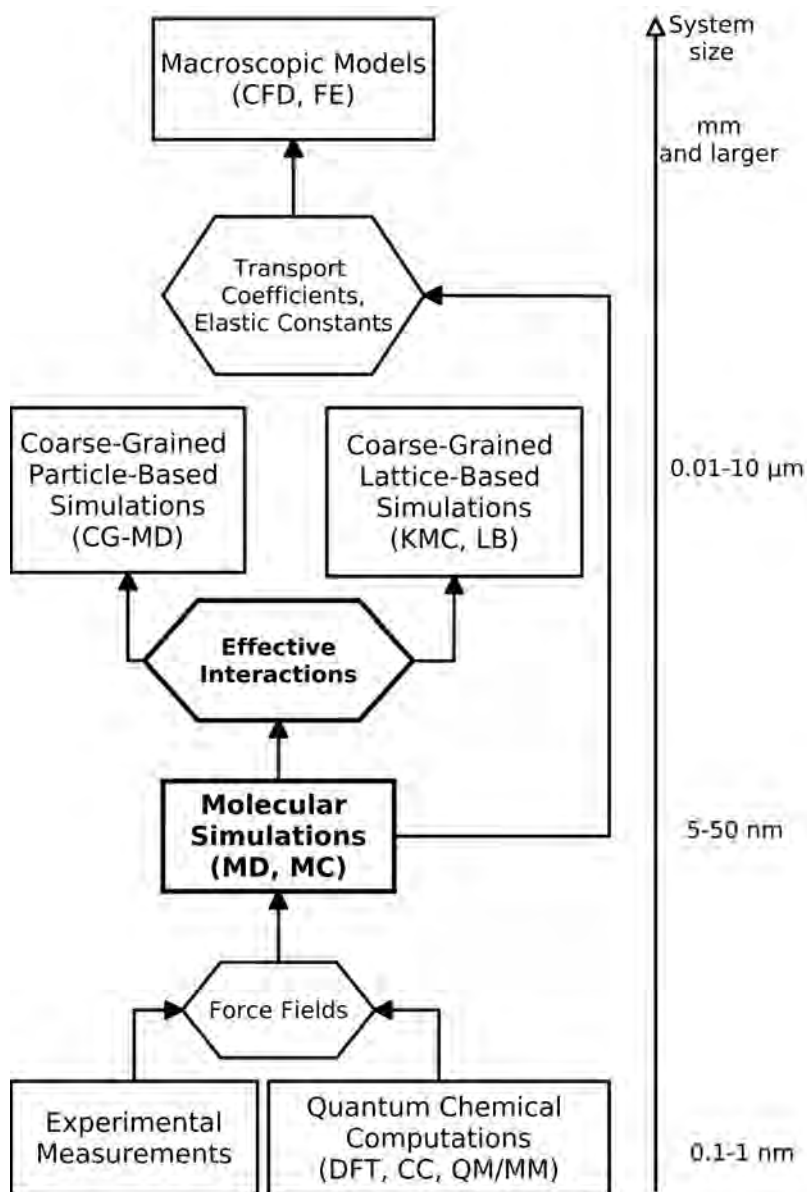


Figure 1.3: Schematic representation of the computation bottom-up approach in materials science. Rectangular boxes represent techniques; hexagonal boxes models or parameters. Some methods are not discussed in the main text: CC (coupled-cluster), QM-MM (Quantum mechanics/Molecular Mechanics), LB (Lattice-Boltzmann) and FE (finite elements). In the present thesis, effective interactions are studied using molecular simulations (bold font in the figure).

as the Density Functional Theory (DFT).⁹² In these calculations, the Schrödinger Equation is solved for systems of up to hundred atoms including their electronic structure. These methods are very accurate in computing geometries and energies of systems consisting of a relatively small number of molecules.⁹³ The indisputable advantages of quantum chemical computations are: *(i)* no a priori unknown input parameters are needed (in principle), and *(ii)* the possibility to study electronic properties and chemical transformations of the matter. One of the limitations of the quantum chemical methods is that dispersion interactions can only be computed accurately when using special techniques like coupled-cluster (CC). These techniques have generally a very unfavourable scaling with the system size.⁹³

The next level are atomistic simulations with a certain interaction model (force field).⁹⁴ This approach will be applied in this thesis. In these simulations, either single atoms (all-atom) or very small groups of atoms (united atoms) are modeled as single sites that interact with each other and experience thermal motion. Interactions between particles in this classical approach are described using analytic functions.⁹⁵ These functions can be completely empirical; but often they have a theoretical background. The parameters for these functions can be obtained from experiment or from quantum chemical calculations. Geometries, bonded interactions and partial charges are usually modeled on the basis of DFT calculations and/or spectroscopic data.^{96–98} The remaining vdW interactions and short-range repulsion are in most cases fitted to reproduce experimental results.⁹⁹ More information on these force-fields can be found e.g. in the recent reviews.^{100–102} It is important to note that classical force fields always have a certain range of applicability. For example, united atom models for alkanes based on their liquid and vapour properties reproduce well their diffusion coefficients and viscosity,⁸⁵ but fail badly to reproduce their solid state properties.^{103,104} Conversely, models based on properties of metals and semiconductors at ambient conditions are not expected to correctly reproduce their boiling temperature. Typical system sizes in atomistic simulations are currently 500-10000 atoms (or 5-50 nm); the recently reported large-scale simulations of biosystems consisting of up to 1000000 atoms are rather exceptional.¹⁰⁵ Once an interaction model is formulated, Monte Carlo (MC) or Molecular Dynamics (MD) simulations can be used to obtain thermodynamic properties of the system using the framework of statistical mechanics.^{85,106} Dynamic properties such as transport coefficients can be obtained from MD simulations.

The size limitation of atomistic simulations can be partly overcome by *coarse-graining* (CG). Large groups of atoms are combined into single particles that interact with each other via effective potentials. The system size in terms of the number of particles is then similar to the one in atomistic simulations; but the associated “real” system size strongly depends on the level of coarse-graining.^{107–111} For example, in the MARTINI force field for biomolecular simulations, groups of 5–12 atoms are combined into CG spheres of ~ 0.5 nm diameter.^{110,111} On a much larger scale, 1 μm large colloidal particles can also be represented by single spherical particles. The solvent is then modeled as an implicit continuous medium

whose properties are manifested in the effective interactions (e.g., as the dielectric constant) between the CG colloidal particles. Typical interaction potentials for colloidal particles include: hard-sphere repulsion, effective vdW interaction,⁸⁸ Yukawa-type screened charged interaction;⁸⁹ the sum of these three terms yields the popular DLVO potential for charged colloids surrounded by an electrolyte double layer.^{89,112} Thermodynamic properties of the coarse-grained systems can be determined from classical MC or MD simulations. Since classical MD does not account for transient interactions with the implicit medium such as friction, the dynamic properties of such systems are studied using special techniques like Langevin,¹¹³ Brownian¹¹⁴ or Dissipative Particle Dynamics.^{115,116} The latter method has the advantage that the total momentum of the system is conserved, which is essential for fluid dynamics of a colloidal suspension.⁸⁵

Kinetic Monte Carlo (KMC) is a useful tool to study the evolution of a system whose microscopic dynamics is governed by rare spontaneous transformations (activated processes) and diffusion. Examples of activated processes are chemical or biochemical reactions, structural transitions or diffusion through narrow pores. In these simulation, the space is coarse-grained into a lattice, and time into (relatively large) time steps. The quality of the predictions strongly depends on the accuracy of the model parameters such as activation energies and diffusion coefficients. Traditional application fields of KMC are nucleation and crystallization, evaporation patterns, diffusion in solids and percolation;¹¹⁷ but it can also be used to model, for example, controlled release of pharmaceutically active compounds.¹¹⁸

Microscopic (interaction) models can be split conceptually into “toy”, “top-down” and “bottom-up” models. A toy model is a hypothetical physical system which has features similar to a real one, but no direct correspondence between the parameters in the model and those in the real world can be given. Thus, toy models are only useful for qualitative predictions or explanations. A common toy model in molecular simulations are “Lennard-Jones particles”: a system of interaction sites with the Lennard-Jones (LJ) pair potential. These systems have thermodynamic features similar to those of simple compounds: solid, liquid and gas phases separated by first-order phase transitions; gas-liquid coexistence below the critical point; etc.^{85,119} In the top-down approach, one imposes an interaction model which is either empirical or based on theory. The model parameters that cannot be measured directly are then chosen to reproduce experimental observations. In the above example, a top-down approach would be to model relatively large molecules (such as benzene) as (coarse-grained) single LJ interaction sites, with interaction parameters fitted to reproduce, e.g., the critical temperature and density. The bottom-up approach requires simulations at different levels of detail, see Fig. 1.3. At each level, the interaction parameters for the next level are computed, unless the interaction form is known from theory and the interaction parameters are measurable directly. In this manner, the final results are derived from first principles. In the above example with benzene molecules modelled as single interaction sites, one would typically first perform an atomistic simulation

of benzene, and then fit the CG interaction to reproduce results of the atomistic simulation. Both the bottom-up and the top-down approach have the potential to make accurate quantitative predictions. The main drawback of the bottom-up approach are the high computational costs required for each level. The gain is then a justified model. The top-down approach requires, typically, much less effort. However, there is a risk that no direct relation between the simulation parameters and the experimental variables can be given, so that the system becomes actually a toy model.

1.2.1 Simulation studies of nanocrystals

We discuss here the two approaches (bottom-up and top-down) with their advantages and drawbacks in view of the existing simulation studies of NCs.

In Ref.,¹²⁰ the bottom-up approach for the computation of thermodynamic properties of cobalt NCs is demonstrated. The study is performed in three steps, each representing a different level of detail. The results of each step were used in the next one. First, an interaction model for Co atoms, surfactant and solvent molecules is developed on the basis of quantum chemical calculations. In such a calculation, all atoms and electrons are considered for systems consisting of 5–30 atoms. Second, this interaction model is used in Monte Carlo (MC) simulations of Co atoms dispersed in a surfactant solution. At this level, a typical system consists of a few hundred Co atoms, and a few thousand solvent molecules, each modeled as a single interaction site, and a few thousand capping molecules each modeled as a chain with 9 beads. It is found that Co atoms aggregate into ≈ 5 nm large clusters (NCs). The size distribution of these clusters depends on the surfactant concentration. An effective interaction $u(r)$ between capped Co NCs can then be computed. Finally, this effective interaction serves as input for a coarse-grained MC simulation. In such a simulation, the capped NCs are modeled as point particles interacting via the effective potential $u(r)$. Aggregation behaviour of hundreds to thousands of Co NCs at varying density can then be studied in the coarse-grained simulations. It is concluded that Co NCs form a hexatic phase which is locally ordered, but shows no long-range order. Note the large increase in system size from the second to the third level. In the MC simulations of the second step, a few hundred Co *atoms* were present, while in the third step the behaviour of a few hundred Co *nanocrystals* could be modeled.

This study is conceptually brilliant, demonstrating the computational bottom-up approach in all its beauty. However, a close inspection reveals several problems associated with this concrete example. First, the authors perform their CG MC calculations not in the continuous space, but on a cubic lattice with a side length comparable to the size of Co atoms. Thus, a lot of detail on the atomistic length scale gets lost. In particular, the entropy is underestimated in such systems. On the other hand, off-lattice simulations would be computationally not affordable.¹²⁰ This is a general problem: atomistic simulations with explicit surfactant and solvent molecules are computationally very expensive. Second, much more

important, the interaction between solvent and surfactant molecules is modeled by a hard sphere repulsion. The reason for this is that the authors were not able to compute the effective interaction with sufficient accuracy using DFT. This means that $u(r)$ is mainly a depletion attraction: when two NCs come close, some additional space becomes available to the solvent molecules, which increases the total entropy; and this induces an effective short-range attraction.¹²¹ We feel, however, that this does not capture the true physical picture of these systems. Depletion effects only become relevant for very large molecules (polymers), but not for the relatively small toluene molecules, as modeled in Ref.¹²⁰ The authors could not obtain more realistic effective interaction $u(r)$ because they originate primarily from solvent–solvent and solvent–surfactant interactions (see also Chapter 4 of the present thesis or Ref.¹²²). These are mainly dispersive interactions in the order of thermal fluctuations, which cannot be resolved accurately using DFT calculations.⁹³

To circumvent the problems of Ref.,¹²⁰ one could use atomistic simulations based on classical force fields. As we have seen, it is rather difficult to obtain all input parameters for molecular simulations of capped NCs accurately from quantum chemical calculations alone. The advantage of classical force fields is that all “strong” interactions (bonded interactions, electrostatics) are derived from quantum chemistry, while the “weak” interactions (mainly vdW interaction) are fitted to experimental data. The objectives of most classical simulation studies of NCs are: (1) determining the equilibrium shape of nanocrystals as a function of size and temperature; (2) structural transitions inside NCs such as melting or change of crystal structure. For example, the energetically preferred morphology of gold NCs has been discussed extensively in atomistic simulation studies; the consensus has not been found yet.^{123–126} In Refs.,^{127,128} the pressure-induced change of crystal structure in CdSe NCs has been studied, and both the mechanism and the transition state could be identified by Grünwald *et al.*^{127,129} The pioneering and very extensive work on gold NCs capped with alkythiols was performed by Luedtke and Landman.^{130–132} These authors have made several important observations, many of which were new and could later be confirmed experimentally:

1. VdW attractions between alkyl chains yield the largest contribution to the total energy of a NC superlattice.^{32,122,133}
2. Capping layers of different NCs strongly overlap in a superlattice.⁶⁶
3. The ratio λ of the ligand length and the NC core radius determines the crystal structure of the Au NC superlattice. For $\lambda < 0.7$, close-packed fcc or hcp structures are formed, while for $\lambda > 0.7$, the bcc structure is preferred.⁶⁵
4. At the boundary $\lambda \approx 0.7$, a temperature-induced transition of the crystal structure of a NC superlattice is possible. Although such a transition has not been observed experimentally so far, it has recently been shown that at different temperatures different crystal structures may form.¹³⁴

5. At low temperatures, tails of the capping molecules bundle, while at higher temperatures a transition to a disordered state occurs. This transition has been observed later in experiments, and the measured transition temperature is in very good agreement with the one predicted by simulations.^{135,136}

These studies provide great insights into the physical properties of capped NCs and their aggregates. However, some questions are still open. It is not clear how mechanical and thermodynamic stability of NC superstructures depends on different parameters such as NC size, ligand length or temperature. The effect of the solvent on the properties of the capping layer remains unclear.

In further classical simulation work, solvation properties of Au NCs were studied in Ref.¹³⁷ It was found that subcritical and supercritical ethane is a good solvent for bare Au NCs, and a poor solvent for capped Au NCs. This study emphasizes the role of the capping layer in the interaction of NCs with the surrounding. In Ref.,¹³⁸ surface properties of capped Au NCs capped by alkythiols were studied. It was found that thiol headgroups tend to “dive” into the NC, and that the state in which the thiol ligands are adsorbed to the NC surface is thermodynamically metastable with respect to the state where the headgroups are inside the NC. Recently, the first attempts to quantify the effective NC–NC interaction were undertaken.^{133,139} Due to the very small number of systems in these studies, no quantitative model for effective NC–NC interaction can be derived on their basis. The state of the art of the bottom-up approach to NC self-assembly is that no reliable first-principles interaction models for capped NCs are available.

Therefore, several attempts to model NC empirically were undertaken. One of the oldest studies of this kind was the work by Sear *et al.*,¹⁴⁰ and we will discuss it in detail to show the advantages and drawbacks of the top-down approach. In this paper, gold NCs at the air-water interface were studied using experiments and molecular simulations. In experiments, spontaneous density-dependent patterning was observed: at low density, NCs formed islands, while at high densities they formed stripes. The authors postulated an effective pair-interaction between capped Au NCs consisting of three terms: hard-core repulsion, strong short-ranged attraction and weak long-ranged repulsion. Particles interacting via this potential form in a simulation density-dependent patterns similar to the ones observed for Au NCs at the air-water interface. Despite the success in reproducing experimental observation, the model of Ref.¹⁴⁰ does not have a solid theoretical or experimental background, and has therefore no predictive power. The long-range repulsion is a particularly dubious part of this model, as it does not have an experimentally confirmed physical origin. Strictly speaking, only one conclusion can be drawn from the modeling results of Ref.:¹⁴⁰ the experimentally observed patterns can be explained by a physical model. Similar interaction potentials were used in Ref.¹⁴¹ to explain formation of NC chains from purely isotropic interactions. We are not aware of any direct indication that these empirical potentials describe the real system.

An attempt to derive the interaction potential purely from theory was under-

taken recently.¹⁴² Different contributions to the total pair potential were adapted from a theory for large colloidal particles with polymers grafted to their surface. However, the latter systems are very different from ligand capped NCs. For instance, polymers in a solvent form random, spherical coils. Any deformation of such a coil reduces its entropy and is therefore unfavourable; the elastic response of a polymer is primarily entropic.¹⁴³ By contrast, surfactant molecules used in NC synthesis have typically alkyltails with less than 20 carbon atoms.³⁷ At room temperature, such molecules are straight zigzag-shaped chains with few so-called gauche defects. A deformation of such a chain leads to unfavourable deformations of bonds and bond angles, and entropy plays only a minor role in the resulting elastic response. Thus, the “phenomenological” interaction from Ref.¹⁴² does not have an adequate physical foundation. The situation is completely different if the underlying interactions originate from the NC cores mainly. In Ref.,¹⁴⁴ the self-assembly of dipolar NCs was studied using experiment and simulations. It was found that the dipole-dipole interactions have the largest contribution to the total energy in this system, so that a model based on these interactions was applied successfully to explain the crystal structures of the NC supra-crystals at different conditions.

The work of Rabani and co-workers^{145,146} on the drying-mediated self-assembly of NCs should also be mentioned in the present context. The goal of these studies was to understand macroscopic observations on self-assembly of NCs as drying patterns at varying solvent evaporation conditions. Three processes are considered simultaneously: solvent evaporation/condensation, solvent diffusion and NC diffusion. The control parameters are temperature, evaporation rate and NC concentration. Several drying patterns could be identified such as formation of NC domains with varying size, fractal aggregates, networks. All these motifs are in good qualitative agreement with experiment, providing a unified picture for a number of different observations. To obtain quantitative agreement with experiment, the effective NC–NC and NC–solvent interactions must be determined for a range of different realistic conditions.

1.3 Molecular simulation techniques

This section contains a brief overview of the methods used in this thesis with some theoretical background. The reader is referred to textbooks^{85,99,106,147,148} for rigorous derivation and details.

1.3.1 The coupling principle

Atomistic models typically represent systems of submicron size. Such tiny entities rarely occur isolated in the real world; the behaviour of these microscopic systems is coupled to their macroscopic environment in some way or another, see Fig. 1.4. For example, the microscopic system and the (implicit) surrounding have

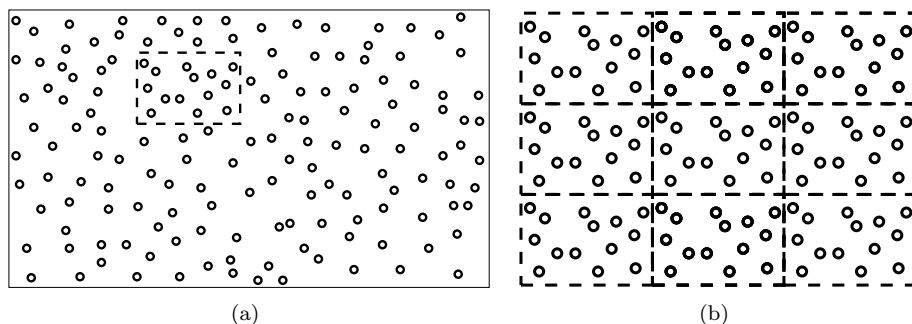


Figure 1.4: (a) Sketch of the microscopic-macroscopic coupling principle. The simulated microscopic system (shown as the dashed box) is considered to be a part of a macroscopic system at given conditions. (b) Periodic boundary conditions: the simulated system (in the center) is surrounded by its copies to mimic the embedding into a bulk phase.

in equilibrium equal temperatures due to heat exchange. One of the central aims of molecular simulations is to mimic this coupling consistently. So, the aforementioned temperature coupling is always present in MC due to its statistical mechanical foundation; in MD simulations it can be realized by a thermostat.

Unless a bulk interface is simulated, the physical environment of a microscopic system is in most cases similar to the system itself. For example, in a glass of water a cubic micron of water (which is a gigantic system for a molecular simulation) is most likely surrounded only by other cubic microns of water; the fraction of such cubelets close to a glass wall is tiny. Therefore, it is natural to implicitly surround a simulated system by its copies using the so called *periodic boundary conditions*, see Fig. 1.4(b). The danger of introducing artificial periodicity can be ruled out by performing control simulations with a larger/smaller size.

1.3.2 Monte Carlo

The objective of the present work is to compute properties of the systems of interest at certain thermodynamic conditions (e.g., fixed temperature). One of the ways to do this is by a MC simulation, which has the following form:

```
{Initialization}
Generate or read in an initial configuration;
Read in simulation and interaction parameters.
{Simulation}
for the given number of cycles do
```

```

    Generate a new configuration according to the imposed thermodynamic conditions;
    Accept or reject this new configuration;
    Compute the desired properties of the current configuration (“sampling”).
end for
{Termination}
Compute and return averages;
Return the final configuration of the system.

```

Statistical mechanical basis

Statistical mechanics studies systems whose state can be characterized by a large but finite number of parameters. In this thesis, the state of a system is often given by the coordinates and momenta of all particles; but there will also be simulations in which the number and/or the identity of particles are necessary to identify a state. A crucial notion is an *ensemble*, which is a set of states satisfying certain criteria (also called *phase space*) and a statistical weight assigned to each state (in other terms, the probability for this state to occur). For example, the state of a set of traffic lights on the crossing of Boltzmannstrasse with Maxwell Drive is at each time point characterized by the signal of each individual stoplight, see Fig. 1.5. A traffic light ensemble would then consist of (1) the phase space of all possible signal combinations (states), and (2) the likelihood for each of these combinations (which is in this case the relative frequency). In a “safe ensemble”, for instance, the statistical weight of all combinations where two cars passing on green can crash should be 0. In a “pedestrian ensemble”, the statistical weight of all states where at least one car signal is green is 0.

The next important concept in statistical mechanics is an *ensemble average*. Consider a property A , which is a function of the state of the system. Then the expected value $\langle A \rangle_{\Upsilon}$ of A in an ensemble Υ is the weighted sum

$$\langle A \rangle_{\Upsilon} = \frac{\sum_{s \in \Upsilon} \pi(s) A(s)}{\sum_{s \in \Upsilon} \pi(s)}, \quad (1.1)$$

where the index s runs over the states of the ensemble; $\pi(s)$ is the likelihood of the state s . If the number of states is small, all states can be considered in the sum of Eq. (1.1). For most molecular systems, the number of states is extremely large and the statistical weight π of the vast majority of states is 0. In this case, special techniques are needed.

Consider our example with the traffic lights. The probability that a pedestrian crossing the Boltzmannstrasse has green light can be expressed as an ensemble average of the property A which is 1 if this pedestrian has green light and 0 otherwise. Another variable that can be expressed as an ensemble average is the “crossing capacity”, i.e. the number of lanes L available to the traffic that goes straight. Imagine that Boltzmannstrasse has one lane in each side and Maxwell Drive has two. In this case, $L_0 = 0$ if cars on both streets have red; $L_B = 2$ if cars



Figure 1.5: Intersection of the Boltzmannstrasse with Maxwell Drive, seen along the Maxwell Drive. The state of the crossing in the traffic light ensemble is defined by the combination of the stoplight signals. Other parameters like the number of cars or the time of the day are not relevant for the definition of a state in this ensemble. The image is taken from <http://commons.wikimedia.org>.

on Boltzmannstrasse have green in both directions; $L_M = 4$ if cars on Maxwell Drive have green in both directions; and $L_{M,B} = 6$ if cars have green on both streets in both directions. The associated weights are then π_0, π_B, π_M and $\pi_{M,B}$, respectively. The last state has $\pi_{M,B} = 0$ probability in the safe ensemble, so that the average number of available lanes is given by

$$\langle L \rangle = \pi_0 L_0 + \pi_B L_B + \pi_M L_M + \pi_{M,B} L_{M,B} = \pi_0 \cdot 0 + \pi_B \cdot 2 + \pi_M \cdot 4 + 0 \cdot 6 = 2\pi_B + 4\pi_M.$$

We assume here that the probabilities are normalized, i.e., $\sum_{s \in \Upsilon} \pi(s) = 1$.

It is important to note that statistical mechanics does not make any statements about the dynamic behaviour of the system. In the example of the traffic lights, no statements can be made about average waiting times since no information about the precise timing of the stoplights is stored in the ensemble formulation.

In thermodynamics, one is interested in a set of N atoms or molecules, whose instantaneous state \mathbf{s} can be characterized by the position \vec{r}_i and momentum \vec{p}_i of each particle i , and the total energy E of this state is given by:

$$E(\vec{r}_1, \vec{r}_2, \dots, \vec{r}_N; \vec{p}_1, \vec{p}_2, \dots, \vec{p}_N) = K(\vec{p}_1, \dots, \vec{p}_N) + U(\vec{r}_1, \dots, \vec{r}_N; \vec{p}_1, \dots, \vec{p}_N). \quad (1.2)$$

where K and U are the kinetic and the potential energy, respectively. Usually, the potential energy is a function of particle positions only, and the dependence on the momenta can be expressed analytically as an “ideal gas contribution”.^{85,106} Consider first the case that the number of particles N and the volume V are fixed, so that the state s of the system is well-defined by the coordinates and the

momenta of the particles. The Hamiltonian \mathcal{H} can then be identified with the energy: $\mathcal{H}(\mathbf{s}) = E(\mathbf{s})$. It is crucial that the Hamiltonian is bounded below, i.e. that there exists an h_0 such that $\mathcal{H}(\mathbf{s}) \geq h_0$ for each state \mathbf{s} .

In order to define an ensemble, one has to assign a probability to each state. The central assumption of statistical thermodynamics is that the likelihood $\pi(\mathbf{s})$ of each state s is a function of the Hamiltonian $\mathcal{H}(\mathbf{s})$ of this state.^{85,149} In other terms, all states in the ensemble with constant number of particles, volume and total energy (NVE) are equally likely. Recall the microscopic-macroscopic coupling principle introduced at the beginning of Section 1.3. Consider a microscopic system (simulation box) with constant volume and number of particles, which exchanges heat with a very large reservoir. Imposing energy conservation for the total system (simulation box plus reservoir), the central assumption yields that the probabilities of two states \mathbf{s}_1 and \mathbf{s}_2 of the microscopic system satisfy^{85,150}

$$\frac{\pi(\mathbf{s}_1)}{\pi(\mathbf{s}_2)} = \exp(-\beta [\mathcal{H}(\mathbf{s}_1) - \mathcal{H}(\mathbf{s}_2)]) \quad (1.3)$$

with a non-negative constant β with units of inverse energy. The underlying probability distribution $\pi(\mathbf{s}) \propto \exp(-\beta\mathcal{H}(\mathbf{s}))$ is called the *Boltzmann distribution*, and the associated probabilities – *Boltzmann weights*. In the limiting cases $\beta \rightarrow \infty$, only the states with the smallest Hamiltonian have a nonzero Boltzmann weight, and therefore the system is in the ground state. On the other hand, if $\beta = 0$, all states become equally likely. This observation rationalizes that the temperature T (in units of K) must be inversely proportional to β . For historical reasons, the thermodynamic temperature is defined as $T = 1/(\beta k_B)$, where $k_B \approx 1.38 \times 10^{-23}$ J/K is the Boltzmann constant. This constant is related to the molar gas constant $R \approx 8.31$ J/(K×mol) via $k_B = R/N_{\text{AV}}$, with the Avogadro number N_{AV} defined earlier in the text. The resulting ensemble with constant number of particles, volume and temperature is called the *canonical ensemble* (NVT).

If the number of states is finite (but very large), the probability of each state is

$$\pi(\mathbf{s}) = \frac{\exp(-\beta\mathcal{H}(\mathbf{s}))}{\sum_i \exp(-\beta\mathcal{H}(\mathbf{s}_i))}. \quad (1.4)$$

For infinite sets, integration naturally replaces summation. Thus, for any observable property A , the ensemble average is given by

$$\langle A \rangle = \frac{\int A(\mathbf{s}) \exp(-\beta\mathcal{H}(\mathbf{s})) d\mathbf{s}}{\int \exp(-\beta\mathcal{H}(\mathbf{s})) d\mathbf{s}}. \quad (1.5)$$

For example, the average energy of the system is given by

$$\langle E \rangle = \frac{\int E(\mathbf{s}) \exp(-\beta\mathcal{H}(\mathbf{s})) d\mathbf{s}}{\int \exp(-\beta\mathcal{H}(\mathbf{s})) d\mathbf{s}}. \quad (1.6)$$

The denominator Z on the right side of this equation is called the *partition function* (or partition sum). It is related to the Helmholtz free energy \mathcal{F} of the system

via

$$\mathcal{F} = -k_B T \ln Z. \quad (1.7)$$

For most systems, \mathcal{F} cannot be computed directly in a single simulation; but free energy difference between different systems can be computed.^{85,147}

Many macroscopic properties can be formulated as observables, and thus they can be expressed directly as ensemble averages: pressure; heat capacity; structural (order) parameters; dielectric constant in polar systems; elastic constants. Naturally, dynamic properties such as diffusion coefficients, viscosity or heat conductivity cannot be expressed as ensemble averages. Some physical variables that are related to Z , such as free energy and entropy, cannot be expressed as ensemble averages. However, the derivatives of the free energy can be expressed as ensemble averages, and thus the free energy can be determined using advanced techniques.

A random walk in the phase space

The canonical ensemble is defined by (1) the phase space, where states are characterized by the positions and momenta of all particles; (2) a Hamiltonian \mathcal{H} ; and (3) the value of β , or equivalently T . Together, the latter two determine the statistical weight of state. The only objective of MC simulations is to compute ensemble averages as in Eq. 1.5. This task is slightly simplified if the potential energy does not depend on momenta, which is the case in classical force fields. Then the integration with respect to the momenta can be carried out analytically, and also the momentum-dependent terms of the observables can be treated separately. Eq. 1.5 becomes

$$\langle A \rangle = \frac{\int A(s) \exp[-\beta U_{\text{pot}}(s)] ds}{\int \exp[-\beta U_{\text{pot}}(s)] ds}. \quad (1.8)$$

where the “reduced” states s depend on positions only. Accordingly, the statistical weight of each state s is proportional to $\exp[-\beta U_{\text{pot}}(s)]$ because the dependence on momenta in Eq. (1.4) cancels.

A naive approach would be to compute the integrals in the numerator and denominator of the right hand side of Eq. (1.8) using a deterministic method (quadrature). Such methods converge with a power of the distance between grid points in the discretized space. Therefore, the number of gridpoints required for a fixed precision grows exponentially with the number of coordinates. For a system consisting of 100 particles in three dimensions, one would need 10^{300} evaluations of the potential when discretizing each degree of freedom by 10 points. This is not feasible. Furthermore, for most grid points in a practical simulation would have a 0 statistical weight. Thus, unless the grid is very fine, the computed integrals in Eq. (1.8) would vanish, and one ends up with a useless “0/0” result.

Stochastic methods are much more efficient for computing high-dimensional integrals. The reason is that the convergence of stochastic methods depends on the number of random grid points, and not on the distance between them. One

therefore performs a discrete random walk (RW) in the (reduced) phase space, such that each state during this walk is visited with a frequency proportional to its Boltzmann weight. In this way, the relevant regions of the phase space are sampled. This is done by defining for each pair of states s, s' the transition probabilities $t(s \rightarrow s')$ and $t(s' \rightarrow s)$ of going in one step from s to s' or vice versa. It is important to impose the *ergodicity* condition on the RW: for each pair of states s, s' with nonzero statistical weights, there is a finite sequence of states (path) between them with a nonzero probability. This condition guarantees that any relevant state can be reached. Note that there is often a nonzero probability $t(s \rightarrow s)$ of staying in the same state. Each state s has a “population” $N(s) \propto \exp(-\beta U_{\text{pot}}(s))$. Consider a pair of states s, s' with non-zero populations, and a (hypothetical) binary RW that goes back and forth between s and s' for a very large number of times M , so that each state is visited M_s and $M_{s'}$ times, respectively. The number M_s can be counted as the number of times that the RW enters the state s from s' , which is $M_{s'} t(s' \rightarrow s)$, plus the number of times that the RW stays in s , which is $M_s(1 - t(s \rightarrow s'))$. This double-counting of M_s yields the following equation:

$$M_s = M_{s'} t(s' \rightarrow s) + M_s(1 - t(s \rightarrow s')). \quad (1.9)$$

It is natural to impose that the number of times each of the states is visited on the binary random walk is proportional to the actual population N of these two states:

$$M_s/M_{s'} = N(s)/N(s') = \exp(-\beta(U_{\text{pot}}(s) - U_{\text{pot}}(s'))). \quad (1.10)$$

Combining Eqs. (1.9) and (1.10), one obtains the so-called *detailed balance* equation:

$$N(s')t(s' \rightarrow s) = N(s)t(s \rightarrow s'). \quad (1.11)$$

Note that this equation also holds in the trivial case when one or more terms become 0.

For the general case of a RW, it can be shown that in order to visit each state with a probability proportional to its Boltzmann factor, it is necessary that the *balance condition* holds:¹⁴⁷

$$\sum_{s' \neq s} N(s')t(s' \rightarrow s) = \sum_{s' \neq s} N(s)t(s \rightarrow s') \quad (1.12)$$

meaning that the total incoming flux to s equals the total outgoing flux from s . If the system is ergodic, then Eq. 1.12 is sufficient to ensure that states are visited with a probability proportional to their Boltzmann weights. Clearly, detailed balance (Eq. (1.11)) is a much stronger condition. Essentially, detailed balance means that all terms in Eq. (1.12) are equal and therefore Eq. (1.12) will hold automatically. Note that, in principle, detailed balance is not necessary.¹⁵¹

In a practical simulation, the term $t(s \rightarrow s')$ is the product of the *attempt probability* $\alpha(s \rightarrow s')$ for trying to move from s to s' and the *acceptance probability*

$\text{acc}(s \rightarrow s')$ that this move is actually performed. Consider the simple case that $\alpha(s \rightarrow s') = \alpha(s' \rightarrow s)$. Then the detailed balance Eq. (1.11) can be rearranged into

$$\frac{\text{acc}(s \rightarrow s')}{\text{acc}(s' \rightarrow s)} = \frac{N(s')}{N(s)} \exp(-\beta(U_{\text{pot}}(s') - U_{\text{pot}}(s))). \quad (1.13)$$

There are infinitely many possible choices for the acceptance probability; however, the original Metropolis criterion¹⁵² has manifested as standard:

$$\text{acc}(s \rightarrow s') = \min(1, \exp(-\beta\Delta U)), \quad (1.14)$$

where $\Delta U = U_{\text{pot}}(s') - U_{\text{pot}}(s)$ is the potential energy difference between the new and the old configuration; the minimum function $\min(a, b)$ is a if $a < b$ and b otherwise. A standard MC step has the following form:

```

{Trial move}
Given an old configuration  $o$  of the system, generate randomly a new configuration  $n$ ;
{Accept or reject the trial move}
Compute the energy difference of the two configurations;
if the new configuration has a lower energy than the old one then
    go from  $o$  to  $n$ ;
else
    go from  $o$  to  $n$  with the probability  $\exp(-\beta\Delta U)$ ;
end if
{Terminate}
if the trial move is accepted then
    update positions and energies.
end if

```

Note that the acceptance rule based on $\exp(-\beta\Delta U)$ is only correct in the case of equal attempt probabilities: $\alpha(o \rightarrow n) = \alpha(n \rightarrow o)$, see the above derivation. If the two attempt probabilities are not equal due to, e.g., a biased trial move generation, such difference must be corrected for in the acceptance rule.

The next question is how to create a new configuration from the old one. The established strategy is to attempt a change of a small, randomly chosen part of the system (e.g., one single particle or molecule). A long sequence of such small changes leads eventually to major changes in the system.

Trial moves

Canonical ensemble In the canonical (NVT) ensemble, the number of particles, volume and temperature are fixed. Our systems of interest consist of atomic clusters (NCs or gold slabs in Chapter 2) and linear chain molecules (capping molecules, n-hexane solvent). To sample the degrees of freedom of such systems, we employ the following “standard” trial moves:

1. Translation of a molecule: all atoms of a single randomly chosen molecule are shifted simultaneously by a vector \vec{d} (generated randomly).
2. Rotation of a molecule: the entire randomly chosen molecule is rotated by a randomly chosen angle around a randomly chosen axis; the center of mass of the molecule remains unchanged.
3. Displacement of a NC atom (Chapter 3): a randomly chosen NC atom is shifted by a randomly chosen vector.
4. Rotation of a NC (Chapter 4): the entire NC is rotated by a randomly chosen angle around a randomly chosen axis; the center of mass of the NC remains unchanged.
5. Cluster rotation (Chapter 4): a NC with all ligands adsorbed to its surface is rotated by a randomly chosen angle around a randomly chosen axis; the center of mass of the NC remains unchanged.

For all these moves, the Metropolis acceptance rule Eq. (1.14) is applied. For a cluster rotation, one has to pay attention that the definition of the “cluster” does not change after the move. If this happens, the move is automatically rejected. Without this additional condition, detailed balance will be violated.

In addition to the “standard” trial moves, we apply the Configurational-bias MC (CBMC) to explore the internal degrees of freedom of the flexible linear chain molecules.^{153–156} This algorithm involves a “smart” generation of a trial move, so that the attempt probability α is not symmetric anymore, which results in a different acceptance rule. The interactions are separated into “bonded” and non-bonded terms; bonded interactions include stretching, bending and torsion of (chemical) bonds; all other interactions, including intramolecular interactions between beads separated by more than three bonds, are considered as non-bonded. A CBMC trial move is performed according to the following protocol:

1. Grow a new configuration and calculate its Rosenbluth factor $W_{\text{new}}^{\text{ext}}$.
2. Grow the old configuration and calculate its Rosenbluth factor $W_{\text{old}}^{\text{ext}}$.
3. Accept the trial move with the probability $\text{acc}(o \rightarrow n) = \min(1, W_{\text{new}}^{\text{ext}}/W_{\text{old}}^{\text{ext}})$.

A new configuration of a linear chain with n beads is “grown” by the following recursive procedure. The bias introduced during such trial move generation is removed exactly in the acceptance rule.^{85,153} Assume that $i - 1$ beads are already grown. For the i th bead

1. Generate K_i trial positions for the i bead with probability proportional to the Boltzmann factor of the bonded interaction energy with the previous beads;

2. Calculate the non-bonded interactions u_j^{ext} for each of the trial positions $j = 1, \dots, K_i$ and the weight $w_i^{\text{ext}} = \sum_{j=1}^{K_i} \exp[-\beta u_j^{\text{ext}}]$;
3. Select one of the trial positions according to probability

$$p_j = \frac{\exp[-\beta u_j^{\text{ext}}]}{w_i^{\text{ext}}}$$

The old configuration of a chain is grown in a similar fashion, but the first trial position is always the old position of the corresponding bead, and it is also the one which always becomes selected. The Rosenbluth factor is defined as

$$W^{\text{ext}} = \prod_{i=1}^n \frac{w_i^{\text{ext}}}{K_i}. \quad (1.15)$$

In a partial regrow move, the headgroup remains fixed while the rest of the chain is regrown.

The computational performance of CBMC can be improved using advanced schemes, e.g. the dual-cutoff CBMC¹⁴⁹ or a biased insertion technique.^{157–159} The CBMC technique can be extended to branched molecules.^{160,161} Further strategies for exploring the phase space of chain molecules include the recoil growth,^{162,163} dynamic pruned-enriched Rosenbluth method,¹⁶⁴ or rebridging MC.¹⁶⁵ The reader is referred to Ref.⁸⁵ for a detailed discussion and comparison of these methods.

Grand-canonical and semigrand ensemble In the grand-canonical (μ VT) ensemble, the volume and temperature are fixed while the number of molecules N_j of species j fluctuates according to its chemical potential μ_j , or equivalently fugacity f_j . This means that the microscopic simulation box and the macroscopic surrounding in Fig. 1.4 not only exchange heat, but also particles. This fluctuating number of molecules represents a dynamic equilibrium between the simulated system and the surrounding bulk phase, in which the species j is at the same temperature and chemical potential. The latter phase is not simulated explicitly. Two examples of such bulk phase are relevant for this work:

1. Unsaturated vapour with a pressure p_j . Away from the boiling temperature, the unsaturated vapour behaves like ideal gas for many compounds. In this case, the ideal gas approximation $f \approx p$ is valid; for a real gas, f and p are related via the equation of state.⁹⁰
2. A dilute solution with concentration c_j . In this regime, Henry's Law is applicable: $c = K_H f$ with a Henry constant K_H , which can be determined from a separate simulation.^{85,94,147}

The sampling of the number of particles N_j is realized using molecule insertion and deletion trial moves, which are attempted with equal probability. An insertion attempt takes the following form:⁸⁵

1. Grow a new molecule of the randomly chosen component j using CBMC and compute the associated Rosenbluth factor $W_{\text{new}}^{\text{ext}}$ of this configuration.
2. Accept or reject with probability

$$\text{acc}(N_j \rightarrow N_j + 1) = \min \left(1, \frac{\beta f_j V}{N_j + 1} \frac{W_{\text{new}}^{\text{ext}}}{W_0} \right) \quad (1.16)$$

where W_0 is the average Rosenbluth factor of a single isolated chain

A deletion is attempted as follows:⁸⁵

1. Select at random a molecule of the randomly chosen component j ;
2. Grow the old configuration of this molecule using CBMC and compute the associated Rosenbluth factor $W_{\text{old}}^{\text{ext}}$ of the old configuration.
3. Accept or reject with probability

$$\text{acc}(N_j \rightarrow N_j - 1) = \min \left(1, \frac{N_j}{\beta f_j V} \frac{W_0}{W_{\text{old}}^{\text{ext}}} \right). \quad (1.17)$$

In the semigrand ensemble, the total number of molecules is fixed, but molecules are allowed to switch their identity according to the chemical potential difference of the two species (or, equivalently, their fugacity ratio).¹⁶⁶ This technique is very efficient when simulating multi-component systems, as mixing or segregation is not limited by diffusion. The associated trial move consists of the following parts:

1. Select the component i at random
2. Select the component $j \neq i$ at random.
3. Remove a randomly selected molecule of component i .
4. Insert a molecule with identity j with identical coordinates of the first bead.

The associated acceptance rule is then⁸⁵

$$\text{acc}(N_i, N_j \rightarrow N_i - 1, N_j + 1) = \min \left(1, \frac{f_i}{f_j} \frac{N_i}{N_j + 1} \frac{W_{\text{new}}^{\text{ext}}}{W_{\text{old}}^{\text{ext}}} \right). \quad (1.18)$$

1.3.3 Molecular Dynamics

The objective of a MD simulations is to construct a representative trajectory in the phase space. It can be used to study the dynamical properties of the system, such as viscosity, diffusivity or heat conductivity. Note that such a trajectory will never be exact: the deviation of a numerical solution of the equations of motion from the exact one always becomes very large very fast.⁸⁵ However, this issue is

not important. The exact dynamics of an experimental system is not reproducible anyway, even if one could track all the particles in the system (which is not possible due to Heisenberg's uncertainty relation). Nevertheless, the dynamical properties of a system can be measured reproducibly, meaning that they do not depend on a particular trajectory. The same holds for MD simulations.

The trajectory is obtained by solving Newton's equations of motion: at each time point t , the total force \vec{f}_i on each particle i equals its mass m_i times acceleration \vec{a}_i :

$$\vec{f}_i = m_i \vec{a}_i. \quad (1.19)$$

This differential equation can be written in terms of the position $\vec{r}_i(t)$ of the particle:

$$\vec{f}_i = m_i \frac{\partial^2}{\partial t^2} \vec{r}_i(t), \quad (1.20)$$

where the force is a function of the positions of all particles. This equation can only be solved approximately by discretizing the time. For a very small time step Δt , the second derivative (acceleration) may be replaced by the central difference:

$$a_i(t) = \frac{\partial^2}{\partial t^2} \vec{r}_i(t) \approx \frac{\vec{r}_i(t + \Delta t) + \vec{r}_i(t - \Delta t) - 2\vec{r}_i(t)}{\Delta t^2}. \quad (1.21)$$

Assume that the trajectory is known for the time points $t - \Delta t$ and t . Combining Eqs. (1.20) and (1.21), the trajectory can be propagated to the point $t + \Delta t$:

$$\vec{r}_i(t + \Delta t) \approx 2\vec{r}_i(t) - \vec{r}_i(t - \Delta t) + \frac{\vec{f}_i}{m_i} \Delta t^2. \quad (1.22)$$

This is the basis of the *Verlet Algorithm*. Other integrators like Velocity-Verlet¹⁶⁷ or Leap Frog algorithms have the same basis and yield rigorously identical trajectories as the Verlet algorithm; but the computed velocities are more accurate.^{85,147,148} On the same basis, special techniques were developed for the systems with constraints (such as fixed bond lengths) or rigid bodies (such as fixed molecular fragments).¹⁶⁸⁻¹⁷⁰ All these algorithms have the following important properties:

1. They are time-reversible.
2. The total energy and the total momentum of the system are conserved.
3. They are symplectic, i.e. the volume in the phase space is conserved.

In practice, these properties were found to be crucial to obtain a representative trajectory.⁸⁵

Most thermodynamic properties are defined for a fixed temperature rather than fixed energy which is conserved by the above integrators. In an MD simulation, the *instantaneous* temperature $T_K(t)$ is related to the kinetic energy:

$$k_B T_K(t) = \frac{1}{N_f} \sum_{i=1}^N m_i v_i(t) \quad (1.23)$$

where v_i is the velocity of the particle i ; N is the total number of particles in the system, and N_f the number of degrees of freedom (typically, $N_f = 3N - 3$ for a three-dimensional system with a conserved linear momentum).⁹⁰ Since T_K is a function of system state, its average value $\langle T_K \rangle$ can be expressed as an ensemble average at a given (thermodynamic) temperature T . It is, of course, desirable to have $\langle T_K \rangle = T$. The fluctuation of the kinetic temperature $(T_K - T)^2$ is another function of state, and its ensemble average vanishes only for very large (macroscopic) systems.^{85,106} Note that in this limit, the NVE and NVT ensembles are identical.

As mentioned at the beginning of Section 1.3, the goal of molecular simulations is to study microscopic systems that are embedded in a bulk macroscopic environment. In MD simulations, the coupling of temperature is realized via a thermostat, which has to fulfill the following requirements:

- The average kinetic energy $\langle T_K \rangle = T$ equals the imposed temperature T .
- The trajectory samples the desired ensemble.
- The thermostat is a small perturbation of the original integrator.

The last condition is necessary to retain the dynamic properties of the system. Several thermostats have been developed; the ones commonly used in atomistic simulations are based on the Andersen or on the Nosé-Hover thermostats.⁸⁵

1.4 Scope and outline

Self-assembly of capped nanocrystals (NC) has attracted a lot of attention over the past decade. Despite progresses in manufacturing of these superstructures, the current understanding of their mechanical and thermodynamic stability is limited. For further applications, it is crucial to find the origin and the magnitude of the interactions that keep self-assembled NCs together, and it is desirable to find a way to rationally manipulate these interactions. NCs are usually protected by an organic capping layer that prevents aggregation, *e.g.* gold NCs are often capped with alkyl thiol molecules.³⁸ These ligands play an important role in the NC self-assembly; however, it is very difficult to assess the properties of the capping layer experimentally. For such systems, molecular simulations are the method choice.

In Chapter 2, we study the formation and structure of an alkylthiol capping layer on Au NCs. To assess the role of the NC surface curvature, a complementary study is carried out for the formation of self-assembled monolayers of alkylthiols on a flat gold surface. The geometry plays a very important role in this formation process, and we find a complex phase behaviour on the planar surface that is absent for the curved NC. We also consider capping exchange, which is an important step in functionalisation of NCs and planar surfaces. We find that the solvent strongly influences the adsorption selectivity, and cannot be ignored in simulations as it was done previously.

In Chapter 3, the attention is turned to semiconductor NCs. The interactions between these NCs and capping molecules are currently poorly understood, although these interactions are the key to their colloidal stability and surface functionalization. Thus, insights from molecular simulations are urgently needed. We study adsorption of capping molecules to CdSe NCs using a pragmatic model based on state-of-the-art force fields without any parameter adjustment. This is the first study of this kind. The computed binding energies are in surprisingly good agreement with earlier quantum chemical calculations and experiment. This provides a crucial proof of principle that it is possible to describe the NC–ligand interactions using classical models. In analogy with Chapter 2, a case study of the formation of a capping layer is carried out. As a result of this case study we are able to formulate some nontrivial and counterintuitive hypotheses that need to be tested further.

We return to gold nanocrystals protected by alkylthiols in Chapter 4. Knowledge on the details of the nanocrystal–nanocrystal interaction is of vital importance to derive a coarse-grained nanocrystal potential. We develop such a potential from atomistic simulations, enabling its use in simulation studies of nanocrystal self-assembly and thus predict nanocrystal superstructure characteristics. We compute the free energy or equivalently the potential of mean force (PMF) as a function of the distance between pairs and triples of interacting capped gold NCs. The influence of several crucial parameters on the PMF is investigated systematically, such as NC size, ligand length, temperature. On the basis of our simulation and modeling results, recommendations are made for the choice of ligand for a desired NC superstructure. This is a small but important step towards rational design of self-assembled structures.

Chapter 2

Monolayers of Alkylthiols on Gold Surfaces

This chapter reports results of Monte Carlo simulations of single gold nanocrystals (NCs) and gold (111) slabs covered with alkylthiols, with and without explicit solvent (n-hexane) at $T = 300$ K. We develop a coarse-grained model for NC–ligand interactions. Adsorption isotherms for propane- and octanethiol show a phase behaviour measured previously in experiments. Comparison of the adsorption isotherm of octanethiol in hexane on a (111) slab with experimental data suggests that in this system no thiolate bond was formed. The geometry of a gold surface strongly influences the formation and structure of the capping monolayer. On a gold (111) surface, attractive interactions between carbon chains are more pronounced than on a NC. This leads to a stronger penetration of the capping layer by the solvent. Adsorption selectivity for binary alkylthiol mixtures is stronger in vacuum than in solution. The convex shape of NCs also reduces the adsorption selectivity of binary thiol mixtures. This result shows that the solvent cannot be ignored in simulations.

2.1 Introduction

Besides the alkylthiol capped gold nanocrystals introduced in Section 1.1, we also consider their bulk analoga in this chapter. On planar gold surfaces, alkylthiols are known to form well organized structures called *self-assembled monolayers* (SAMs). The gold–thiol interaction is very strong, preventing the surfactants from evaporating or dissolving.⁴⁶ As a result, these SAMs are stable at ambient conditions. Gold SAM structures are promising materials for various applications such as controlled wetting, catalysis, sensing and in biotechnology.^{171,172} A large amount of research has been carried out on the preparation, structure and application of SAMs of alkyl thiols on gold. For two reasons gold (111) surfaces

are often studied: they are easy to prepare experimentally¹⁷² and thiols adsorb readily on such surfaces.¹⁷³ In saturated systems, the aliphatic tails align parallel to each other making an angle of 25 – 30° with the surface normal.¹⁷¹ In such systems, thiol heads form a 2D hexagonal overlattice on the flat (111) surface with S–S spacing of ≈ 5 Å. In the *conventional description* of SAMs, a thiol headgroup adsorbs to a hollow site between three Au atoms, so that the S–S spacing is ascribed to the spacing between such hollow sites. A major open question was whether a thiol headgroup dissociates on the gold surface to form a thiolate, or not.^{171,172,174} It is known since early measurements¹⁷⁴ that a thiolate binds much stronger than an intact thiol (45 vs 12.5 kJ/mol); however, it is not clear whether this energy difference is sufficient to break the S–H bond. Early Density Functional Theory (DFT) computations suggested formation of a thiolate,¹⁷⁵ while a later *ab initio* study has shown that the S–H bond only breaks on a Au surface defect.¹⁷⁶ Very recent experimental and computational studies provide evidence for a much more complex gold–thiol(ate) surface structure.^{177–180} The surface gold layer is shown to reconstruct such that some Au atoms are in the same plane as adsorbed thiolate headgroups and bind to two S atoms each (this process was dubbed surface polymerisation¹⁷⁹). On the other hand, very small gold clusters such as Au₂₅ or Au₃₈ coated by thiols behave like giant molecules rather than surfactant capped colloids:^{181–186} they feature well-defined stoichiometry and surface bonds.

Little is known about the formation of SAMs and structure of unsaturated systems. Poirier *et al.* described using scanning tunneling microscopy a coverage-dependent transition from a 2D-liquid to a 2D-crystal during the formation of butanethiol-SAM¹⁸⁷ without the presence of a solvent. For decanethiol, even more coverage-dependent 2D-phases are possible.¹⁸⁸ This complex phase behaviour is in contrast with the simple Langmuir adsorption for octane-thiol in n-hexane solution, observed by Karpovich and Blanchard.¹⁸⁹

While self-assembled monolayers of alkylthiols have been studied extensively, less is known about the structure of these molecules adsorbed on gold NCs. At room temperature, octanethiol and shorter thiols are completely conformationally disordered.¹³⁵ Experiments show that temperature-induced phase transitions of the capping layer of CdSe NCs dramatically alter optical properties of NCs in solution.¹⁹⁰ This is due to the reconstruction of the NC surface, induced by phase transitions in the capping layer. Therefore, it is of considerable importance to study how the internal structure of molecules in the capping layer depends on the geometry (size, shape and curvature) of NCs. It was also observed that the structure of 2D and 3D assemblies of NCs strongly depends on the nature of the surfactant molecules and the solvent, and also on the NC size.^{48,49,191}

As it is difficult to obtain such structural data or information on the adsorption behaviour on NCs from experiments, molecular simulations may provide more insight on this topic. Several molecular simulation studies on gold-thiolate systems have been undertaken. Hautman and Klein developed the first effective potential for the gold (111)-sulfur and gold (111)-carbon interactions.¹⁹² They mimicked

gold as a plane without structure interacting with united atoms. This model was quickly adopted because it correctly describes the structure of SAMs.^{192,193} Furthermore, using the effective potential is computationally relatively cheap, compared to full Au atom models. In Refs.^{158,194,195} the Hautman-Klein (HK) model was used to describe phase behaviour of mixed SAMs using MC, while Refs.^{196–198} used lattice models. In two independent studies,^{131,199} atomistic force-fields for the Au–thiolate interactions were developed. These were based on *ab initio*⁴⁶ calculations and experimental data¹⁷⁴ on Au–thiolate systems. Several experimentally observed phenomena could be reproduced in Molecular Dynamics simulations, such as the chain-melting temperature of a capping layer and the dependence of the structure of a NC superlattice on the chain length of the capping molecules.^{131,132}

In this chapter we study both flat Au (111) surfaces and NCs as sorbates for alkylthiols. We compute adsorption isotherms to understand the thermodynamics and structural properties involved in the formation of self-assembled monolayers and capping layers. We also study the adsorption selectivities of binary mixtures of alkylthiols that differ in tail length to larger NCs. An important aspect in these simulations is the influence of the solvent which we simulate explicitly. Our aim is to determine the difference between (1) systems in solution and in vacuum, and (2) elaborate the formation and structure of capping layers on planar Au (111) surfaces and on gold NCs. We adhere to the conventional description of thiols on gold surfaces, since it very well explains experimentally observed packing, order and thermodynamic properties of SAMs. These properties are not affected by the precise Au–S binding details, and this is why they can be reproduced in molecular simulations using, e.g. the Hautman-Klein potential. We also develop a coarse-grained interaction potential between icosahedral NCs and united atoms that can be used to efficiently compute thermodynamic and structural properties of alkylthiol capping layers adsorbed on gold NCs. This potential can be considered as 3D-analogue of the popular Hautman-Klein potential.¹⁹²

In previous simulation studies, saturated alkylthiol SAMs and capping layers on gold NCs were studied.^{131,137,158,192–195,199} In this case, the Au–S interaction strength is of minor importance as long as it is very strong. In this work, however, we focus on the actual formation of SAMs and NC capping layers using equilibrium Monte Carlo simulations. Here, the Au–S interaction plays a crucial role. The Morse potential used Refs.^{131,137,199} yields almost twice as strong effective interaction compared to the Hautman-Klein (HK) potential. We show in Section 2.4.2 that, as long as the Au–S interaction is by orders of magnitude stronger than thermal fluctuations and $\text{CH}_x\text{--CH}_y$ and Au– CH_x interactions, the results from different adsorption simulations can be related by a simple mathematical transformation (see also Ref.¹⁵⁹).

The remainder of this chapter is structured as follows. We first introduce our interaction model in Section 2.2. In Section 2.3, we develop a novel coarse-grained potential for icosahedral NCs. Our simulation methods are presented in Section 2.4. Section 2.5 is devoted to the computed adsorption isotherms. In

Section 2.6, we focus on the structural properties of adsorbed system at various loadings such as orientation and density profiles. In section 2.7 we investigate selective adsorption of binary mixtures of alkylthiols with different chain lengths.

2.2 Molecular model

We apply a united atom model where groups of atoms are represented by single ‘pseudo atoms’. We use this approach for SH, CH₂ and CH₃ groups in ligand and solvent molecules. We denote the first by S and the last two by C (a C segment at the end of a chain is a CH₃ type and a CH₂ type otherwise). The surfactants (alkylthiols) are referred to as “SC x ”, where x is the number of alkyl chain segments in the linear tail. Solvent and surfactant molecules interact with each other via truncated and shifted Lennard-Jones (LJ) pair interactions ϕ_{TS} between united atoms

$$\phi_{\text{TS}}(r_{ij}) = \begin{cases} \phi_{\text{LJ}}(r_{ij}) - \phi_{\text{LJ}}(r_c) & r_{ij} \leq r_c \\ 0 & r_{ij} > r_c \end{cases}, \quad (2.1)$$

where ϕ_{LJ} is the LJ potential:

$$\phi_{\text{LJ}}(r_{ij}) = 4 \epsilon_{ij} \left[\left(\frac{\sigma_{ij}}{r_{ij}} \right)^{12} - \left(\frac{\sigma_{ij}}{r_{ij}} \right)^6 \right]. \quad (2.2)$$

In these equations, r_{ij} is the distance between two united atoms i and j , and r_c is the cutoff distance (here $r_c = 12.0 \text{ \AA}$). The potential well depth is ϵ_{ij} and σ_{ij} is the size parameter for particles i and j . The parameters for C–C interactions are taken from Ref.⁹⁸ the ones for C–S and S–S from Ref.¹⁹² In surfactant and solvent molecules, we account for intramolecular bond stretching, bond bending and torsional forces with parameters from Ref.⁹⁸ Additionally, we apply a LJ interaction between segments that are separated by more than three bonds. The gold structures are made up from Au atoms that interact with other species via truncated and shifted LJ pair interactions (using $r_c = 12.0 \text{ \AA}$). To keep computational efforts to acceptable levels, all gold structures are considered as rigid.

2.2.1 Au–S and Au–C interactions

To make a fair comparison between the adsorption of alkylthiols on NCs and on flat Au (111) surfaces, interactions with all gold atoms are considered. To derive the parameters for these pair-interactions, we start from the Hautman-Klein (HK) potential

$$V_{\text{eff}}(z) = \frac{C_{12}}{(z - z_0)^{12}} - \frac{C_3}{(z - z_0)^3}, \quad (2.3)$$

where z represents the distance of a united atom to the gold surface, and C_{12} , C_3 , z_0 are parameters that determine the potential well-depth U_m and its position z_m .

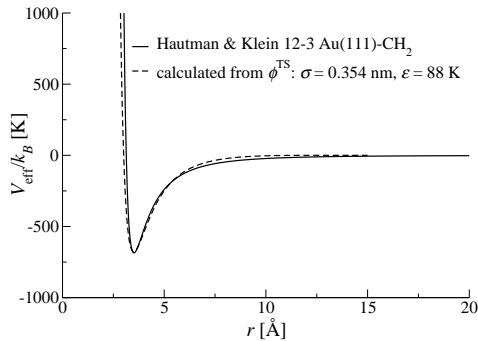


Figure 2.1: Fit of the Au-CH₂ LJ parameters to the Hautman-Klein effective potential Eq. (2.3) for $T \rightarrow \infty$.

We assume that Au atoms interact with other species via a truncated and shifted LJ potential (Eq. 2.1). We find the corresponding LJ parameters ϵ and σ such that it reproduces $V_{\text{eff}}(z)$ by calculating the average interaction energy $\langle U \rangle(z)$ as a function of separation z of a single CH_x or S segment from a sufficiently large gold (111) slab with lattice spacing 4.08 Å. The average interaction at a given separation z is determined by randomly generating a large number N of x_i, y_i ($i = 1, \dots, N$) positions in a plane at distance z and calculating the Boltzmann average energy

$$\langle U \rangle(z) = \frac{\sum_{i=1}^N \mathcal{V}(z, x_i, y_i) \exp[-\beta \mathcal{V}(z, x_i, y_i)]}{\sum_{i=1}^N \exp[-\beta \mathcal{V}(z, x_i, y_i)]}. \quad (2.4)$$

with $\beta = \frac{1}{k_B T}$ (k_B is the Boltzmann constant). Here, $\mathcal{V}(z, x_i, y_i)$ is the effective interaction with the gold slab, given by

$$\mathcal{V}(z, x_i, y_i) = \sum_{j=1}^{N_{\text{Au}}} \phi_{\text{TS}}(r_{ij}), \quad (2.5)$$

where N_{Au} is the number of gold atoms in the slab. A fit of $\langle U \rangle(z)$ to $V_{\text{eff}}^{\text{eff}}(z)$ now determines the LJ parameters for the Au-S and Au-C interactions. We consider two cases: one where we compute $\langle U \rangle(z)$ for the desired temperature $T = 300$ K and another where the effective interaction is calculated for the limit $\beta \rightarrow 0$ ($T \rightarrow \infty$).

For both cases we found force field parameters that closely reproduce $V_{\text{eff}}(z)$; an example is shown in Fig. 2.1. At $T = 300$ K, the Boltzmann weights of the x, y positions on the plane that are just above a hollow site between three Au atoms of the Au (111)-plane have a larger contribution to the average energy $\langle U \rangle(z)$. At $T \rightarrow \infty$, all x, y positions have equal weights in Eq. 2.4. As a result, $\epsilon_{T=300 \text{ K}}$

Table 2.1: Force field parameters for the LJ interactions in our system. The $\text{CH}_x\text{-CH}_y$ interaction parameters are taken from Ref.⁹⁸ The S-CH_x were taken from Ref.¹⁹² Au-S and Au-CH_x interactions were derived using Eqs. 2.4 and 2.5. Note that the Au structures are rigid and therefore we do not include Au-Au interactions.

$\epsilon_{ij}/k_B[\text{K}]$	CH_3	CH_2	SH	$\text{Au}_{T \rightarrow \infty}$	$\text{Au}_{T=300 \text{ K}}$
CH_3	108	78	117	108	108
CH_2	78	56	84	88	88
SH	117	84	126	4260	2795
$\text{Au}_{T \rightarrow \infty}$	108	88	4260	-	-
$\text{Au}_{T=300 \text{ K}}$	108	88	2795	-	-
$\sigma_{ij} [\text{\AA}]$	CH_3	CH_2	SH	$\text{Au}_{T \rightarrow \infty}$	$\text{Au}_{T=300 \text{ K}}$
CH_3	3.76	3.86	4.11	3.54	3.54
CH_2	3.86	3.96	4.21	3.54	3.54
SH	4.11	4.21	4.45	2.40	2.65
$\text{Au}_{T \rightarrow \infty}$	3.54	3.54	2.40	-	-
$\text{Au}_{T=300 \text{ K}}$	3.54	3.54	2.65	-	-

is lower than $\epsilon_{T \rightarrow \infty}$, see Table 2.1. Lowering ϵ leads to a decrease in effective interaction range as a function of z . Hence, a fit to the Hautman-Klein effective potential for $T = 300 \text{ K}$ requires a larger σ parameter compared to $T \rightarrow \infty$. The force field parameters for each interaction type within our system are summarized in Table 2.1.

2.3 Coarse-grained model for gold nanocrystals with an organic capping layer

The popular approach by Hautman and Klein¹⁹² of approximating the Au (111) surface-system interaction by a unidirectional effective potential is unsuitable for gold NCs as they typically have an icosahedral (Ih) shape as in Fig. 2.2(a).^{125,200,201} In this section we develop an analogue of the Hautman-Klein potential for NCs.

We consider a half-line starting from the NC-center. A certain part of this line lies inside the Ih. We denote its length by r_{ico} that obviously depends on the orientation of the half-line. The facet triangle pierced by this line is then the closest facet. If α is the angle between the half-line and the line connecting the center of the closest facet with the NC-center, then $r_{\text{ico}} = R_{\text{in}}/\cos \alpha$, see Fig. 2.2(b). We place a pseudo-atom at each point on this half-line and calculate

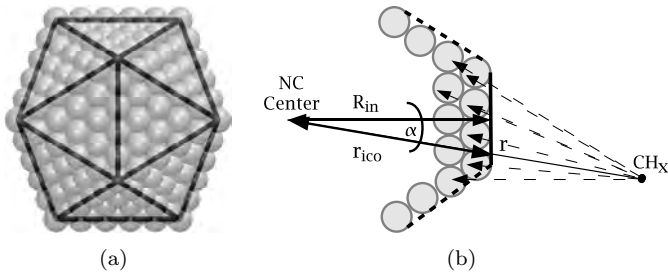


Figure 2.2: (a) Schematic representation of an icosahedral (Ih) nanocrystal: atoms of the NC are represented by grey spheres, edges of the Ih by black lines. (b) A sketch of the effective potential calculation. Gold atoms are represented by large grey circles, a pseudo-atom (CH_x) by the black dot and the closest facet of the Ih by the bold vertical line. The half-line mentioned at the beginning of Section 2.3 connects the NC-center with CH_3 . The bold dashed lines represent other facets. The distance between the pseudoatom (CH_3) and NC-center is r . Dashed arrows represent LJ interactions with the gold atoms, the sum of which is $U_{\text{eff}}(r)$ as in Eq. (2.6). The solid double-sided arrows indicate the in-radius R_{in} and the part of the half-line inside the Ih r_{ico} ; the angle between them is α .

its total interaction with the nanocrystal,

$$U_{\text{eff}}(r) = \sum_{i=1}^{N_{\text{nano}}} \phi_{\text{LJ}}(r_i) \quad (2.6)$$

with r being the distance to the NC-center, r_i the distance to the gold atom i and N_{nano} the number of atoms in the NC. We find that for all orientations we can fit $U_{\text{eff}}(r)$ with the same type of function:

$$U_{\text{eff}}(r) = \frac{5}{3} (2.5)^{\frac{4}{6}} U_{\text{min}} \left[\left(\frac{\tau}{r - r_{\text{ico}}} \right)^{10} - \left(\frac{\tau}{r - r_{\text{ico}}} \right)^4 \right], \quad (2.7)$$

where U_{min} and τ determine the potential well depth and width, respectively. The potential of Eq. (2.7) has a minimum at $r^* = r_{\text{ico}} + \tau \sqrt[6]{2.5}$ with the value $U(r^*) = -U_{\text{min}}$. Just as for r_{ico} (Fig. 2.2(b)), the parameters τ and U_{min} (in principle) depend on the orientation of the half-line. Remarkably, the value of τ differs by only 0.2 \AA for different orientations of the half-line and, therefore, it will be set constant. Fig. 2.3(a) shows that the value of U_{min} is lowest in the direction of a facet center and highest in the direction of a corner, the difference is factor 3. This has also been observed for the effective interactions between an argon atom and a fullerene molecule.²⁰² The $10 - 4$ potential of Eq. (2.7) has the same asymptotic behaviour as the coarse-grained model of Ref.,¹³³ where the

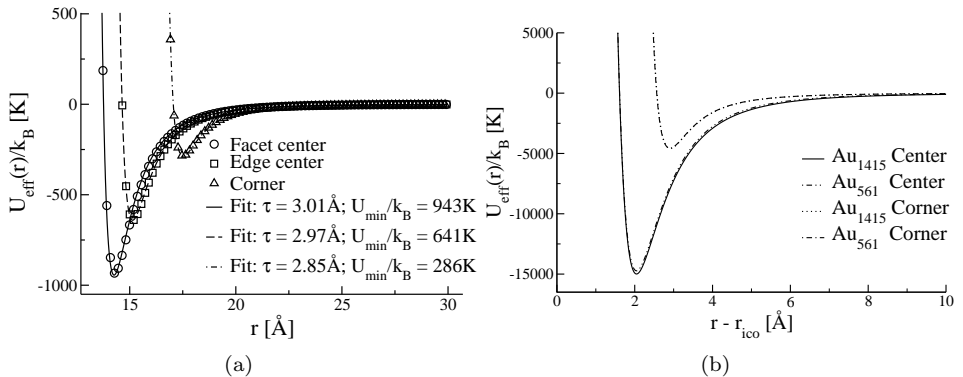


Figure 2.3: Effective interactions of pseudo-atoms CH_3 (a) and SH (b) with nanocrystals. (a) Effective Au_{561} — CH_3 interaction along half-lines through the midpoint, edge center and a corner of a facet (symbols); and fits to the 10 – 4 potential of Eq. (2.7) (lines). Parameters τ and U_{min} result from fitting to the individual curves. (b) Effective Au_{561} — SH and Au_{1415} — SH interactions, respectively, calculated in the direction of a facet midpoint and of a corner. Note that on the horizontal axis r_{ico} is subtracted. The pairs of lines corresponding to same directions coincide.

Au — CH_x interaction is modeled via a 12 – 4 potential. However, it is important to note that in that work the coarse-grained potential has a spherical symmetry (i.e. r_{ico} , τ and U_{min} are constant), and hence the repulsive part of the potential (which results from the shape of the NC) is expected to be different.

We have calculated the effective interactions also for Au_{1415} (diameter $\approx 40 \text{ \AA}$), see Fig. 2.3(b). The size effect on the effective interaction is negligible, i.e. the parameters τ and U_{min} are the same for both NCs. Therefore, our coarse-grained model will also be applicable to all larger icosahedral NCs.

The icosahedral shape influences U_{min} significantly in the following way: at the facet midpoint a particle has more gold atoms in its neighborhood than on the edge, and hence more attractive contributions to the potential, see Fig. 2.2(a). This geometrical difference is expressed primarily by the value of the angle α . The well-depth U_{min} depends also on the atomistic structure of the surface. In the conventional description,^{171,176} a thiol head prefers a hollow site between three gold atoms over a position on top of a gold atom. This makes a convenient analytical expression for U_{min} impossible. This phenomenon can only be taken into account by tabulating U_{min} . We have chosen, instead, to average U_{min} over the surface structure. The same problem arises when modeling extended surfaces, and the popular Hautman–Klein potential implicitly averages over the atomistic structure of bulk $\text{Au}(111)$.

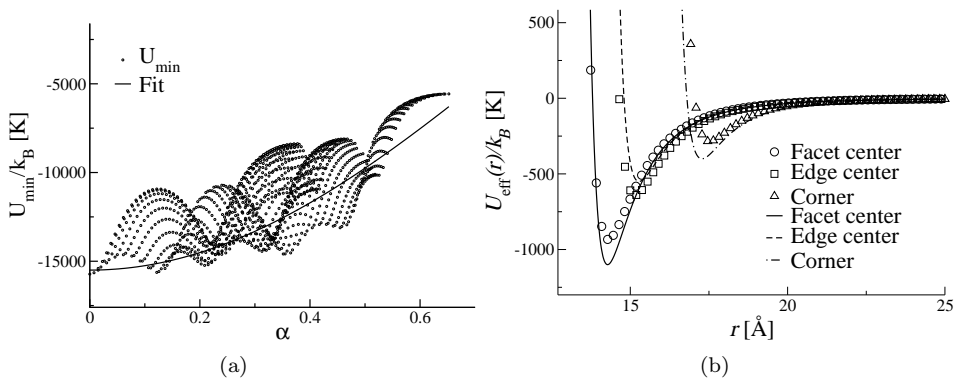


Figure 2.4: (a) The minima U_{\min} of the effective interaction Eq. (2.7) as function of α for a large number of orientations for SH (represented by dots). The orientations are chosen uniformly from the triangle with corners at a facet center, at a corner and at an edge center; other orientations follow by symmetry of the Ih-surface. Circular patterns arise due to atomistic details of the surface. The fit to Eq. (2.8) with parameters from Table 2.2 is displayed by the solid line. The parameters are chosen in a way that low energies are better reproduced than the high ones. (b) Effective Au₅₆₁—CH₃ interaction along half-lines through the midpoint, edge center and a corner of a facet (symbols), and according to Eq. (2.8) with parameters from Table 2.2 (lines), in contrast with Fig. 2.3(a) where the parameters were fitted to individual curves.

Table 2.2: Force field parameters for the coarse-grained interaction potential Eqs. (2.7) and (2.8).

	U_{\min}^C/k_B [K]	η/k_B [K]	τ [Å]
CH ₃	1200	2500	2.9
CH ₂	970	2020	2.9
SH	15500	25000	2.35

We calculate U_{eff} and U_{min} for half-lines going through points of the triangle limited by a facet center, edge center and a corner. Any point on the Ih-surface is equivalent to a point inside such a triangle by symmetry. We fit those minima to the function

$$U_{\text{min}} = U_{\text{min}}^C - \eta \sin^2 \alpha \quad (2.8)$$

with U_{min}^C being the well-depth at the facet center and η a constant fitting parameter, see Fig. 2.4(a). In principle, η depends on a second angle, e.g. the angle between the half-line and the NC-center-corner line. However, we could obtain sufficient accuracy using a constant, averaged η . Parameters for different pseudoatoms are summarized in Table 2.2. Fig. 2.4(b) shows that, due to this averaging procedure, the effective potential is not reproduced as nicely as in Fig. 2.3(a) anymore.

To obtain a quantitative justification of our coarse-graining we compared average $\text{Au}_{561}\text{-CH}_x$ and $\text{Au}_{561}\text{-SH}$ interaction energies in the full-atom model Eq. (2.6) with the ones in the coarse-grained model Eq. (2.8) with parameters from Table 2.2. A large number of random positions at a fixed distance r from the NC-center was generated. For each of these points, the interaction energy with a full-atom NC and the effective potential Eqs. (2.7) and (2.8) were calculated. A normal average and a Boltzmann average (i.e. weighted with $\exp[-U/k_B T]$ at $T = 300\text{K}$) over the values were taken. Relative energy differences of both averages between the two models were less than 20% close to the surface $14 \text{ \AA} \leq r \leq 16 \text{ \AA}$ and less than 5% at large distances $18 \text{ \AA} \leq r \leq 21 \text{ \AA}$. The error is caused by the averaging over the atomistic structure, see Fig. 2.4 and is, therefore, inevitable. Note that the error becomes larger for $r \geq 20 \text{ \AA}$ when truncating the LJ potential in the full-atom model. In Section 2.6.3 we will show that our CG model accurately reproduces structural properties of the capping layer.

It is important to note that our coarse-graining procedure is fundamentally different from the well-known approach by Hamaker.⁸⁸ An analytical expression for the attraction between spherical colloids was derived there. Hamaker assumed that interaction centers are smeared out homogeneously over the object, and integrated the Van der Waals - attractions. In Ref.²⁰³ the same integration has been done for LJ interactions between spherical NCs and point particles. We tried this approach for our system. Along different half-lines, we integrated the LJ-potential $\phi_{\text{LJ}}(r)$ over the Ih instead of the summation over the gold atoms in Eq. (2.6). The resulting effective interactions for SH are up to a factor 1.5 weaker than the ones obtained from Eq. (2.6); for CH_x both approaches yield similar results. Note that a typical distance between a thiol headgroup and the closest gold atom is approximately the same as the distance between two closest gold atoms ($\approx 2.9 \text{ \AA}$),¹⁷⁶ and therefore SH can feel the discrete surface structure. Thus, the Hamaker approach is not always suitable for interactions between NCs and atoms.

2.4 Monte Carlo simulations

To study the adsorption of alkylthiols on gold (with or without explicit solvent), we apply Configurational-bias Monte Carlo (CBMC) simulations.^{153–156} During the simulations, the following MC trial moves are used: molecular translations,¹⁵² molecular rotations,²⁰⁵ (partial) chain regrows, chain insertions/removals (grand-canonical MC), and identity changes²⁰⁶ (semi grand-canonical MC¹⁶⁶), see Section 1.3.2. In Fig. 2.5, our simulation setup is sketched. We simulate separately systems with and without a gold structure. In grand-canonical MC, both systems are allowed to exchange molecules with the solvent reservoir and/or the thiol reservoir. Semi grand-canonical MC moves can be viewed as removal of a molecule of one type and insertion of another type with their difference in chemical potential or fugacity ratio as a driving force.

Note that the Au–S interaction is strongly attractive compared to the other intermolecular interactions (Au–CH_x, S–CH_x and CH_x–CH_y). This high adsorption affinity requires special insertion techniques to sample the number of adsorbed thiol molecules $\langle N \rangle$ in grand-canonical Monte Carlo simulations.

The simulations of the planar Au (111) systems are performed in rectangular simulation boxes in which a gold slab of $N_{\text{Au},x} \times N_{\text{Au},y} \times N_{\text{Au},z} = 12 \times 12 \times 6$ atoms is oriented parallel to the xy -plane and situated at half the boxlength in the z -direction. Periodic boundary conditions are applied. We make sure that molecules cannot interact with each other through the slab, i.e. molecules on one side of the slab cannot “feel” others on the other side of the slab. The simulations of NCs (consisting of 561 or 1415 Au atoms, with a size of 2.7 and 3.7 nm, respectively) are performed in cubic simulation boxes. For both the simulations of the gold slab as well as simulations with a gold NC, we choose sufficiently large box sizes to avoid interactions between periodic images of the (capped) gold structures. To determine the adsorption isotherms, we calculate the number of alkylthiols $\langle N \rangle$ adsorbed on the gold structure as a function of the thiol concentration (c_t , for systems with a solvent present) or thiol density (ρ_t , for systems without a solvent) in the other simulation box at the same fugacity of the thiol molecules, see Fig. 2.5.

In all simulations with explicit solvent (n-hexane), we impose a solvent fugacity of $f_s = 20.0$ kPa corresponding to the experimental n-hexane density (7.598 mol/l at $T = 300$ K and 1 atm²⁰⁴). As the thiol concentration c_t in the box not containing the gold structure is very low, we can use Henry’s law $c_t = K_H f_t$ to determine c_t for a given thiol fugacity f_t . We determine the Henry coefficient K_H via (semi) grand-canonical MC simulations by imposing a thiol fugacity f_t that results in a very low thiol concentration. Fig. 2.6 shows the Henry coefficient K_H as a function of tail length x . The linear relation between $\ln K_H$ and tail length x is due to the fact that $\ln K_H$ is proportional to the interaction energy of a single solute molecule with the solvent, which increases linearly with the alkyl tail length. For simulations without solvent the thiol density ρ_t follows directly from the ideal gas law ($f_t = \rho_t k_B T$).

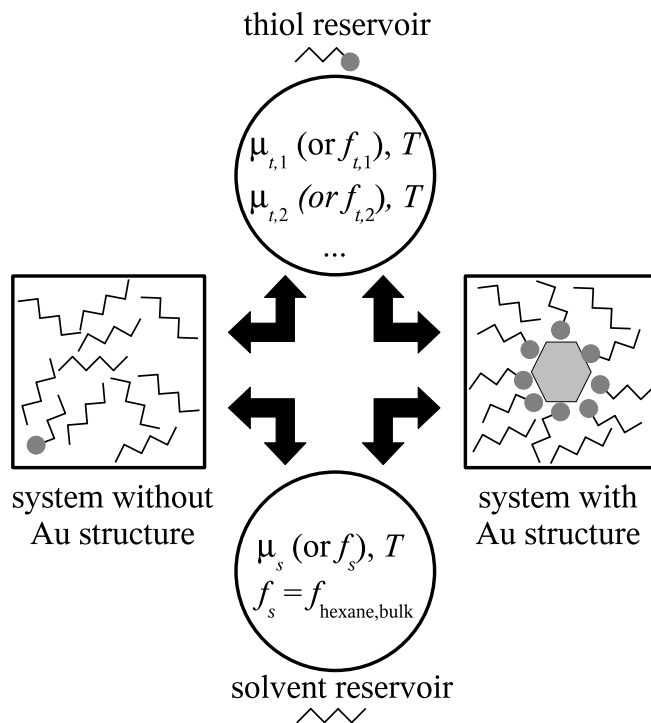


Figure 2.5: General scheme for the type of simulations performed in this work. We have two reservoirs with which we exchange molecules. By tuning the fugacity $f_{t,i}$ of each thiol, we determine the average number of thiols $\langle N \rangle$ in the system with a gold structure (NC or (111) slab) and in the system without a gold structure present. Due to the very attractive Au-S interaction, the values of $\langle N \rangle$ will not be identical for these systems. To estimate the adsorption isotherm as a function of bulk thiol concentration (c_t , for systems with a solvent present) or thiol density (ρ_t , for systems without a solvent), it is therefore necessary to simulate both systems. For systems with a solvent (n-hexane) present, the fugacity $f_s = 20.0$ kPa of the solvent is set such that it reproduces the experimental density of pure n-hexane (7.598 mol/l at $T = 300$ K and 1 atm²⁰⁴).

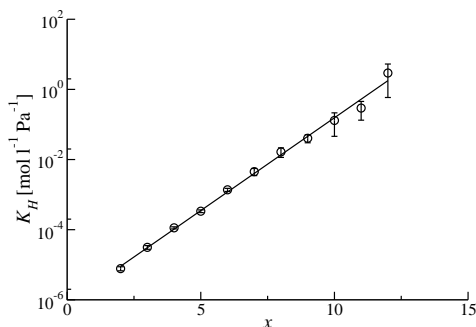


Figure 2.6: Henry's law coefficients K_H as a function of chain length x of alkylthiols SCx in hexane at $T = 300$ K.

2.4.1 Biased insertion technique

Biased insertion can significantly improve the efficiency of conventional grand-canonical MC. Two possible ways to realize this are often used:

1. Generate F trial positions randomly for the first bead and select one of them with a probability proportional to its Boltzmann weight;²⁰⁷
2. Insert the first bead at a trial position (x', y', z') with a probability proportional to a predefined distribution $\rho(x, y, z)$.²⁰⁸

The latter is useful only if favourable positions for particles are known a priori. In our case, thiol heads stay preferably close to the gold surface. We combine the two methods by generating F trial positions for the first bead according to a certain distribution $\rho(x, y, z)$, and then selecting one of them with a probability proportional to its Boltzmann weight. The arising bias is corrected in the acceptance rules. For insertion of a chain ($N \rightarrow N + 1$) the algorithm works as follows:

1. Generate F trial positions for the first bead according to the distribution $\rho(x, y, z)$ and compute their energies $U(1), \dots, U(F)$;
2. Select one of them, n , with coordinates (x_n, y_n, z_n) according to probability $P_{\text{ins}}^{\text{sel}} = \frac{\exp(-\beta U(n))}{\sum_{j=1}^F \exp(-\beta U(j))}$ and set $w_1^{\text{ext}} = \frac{\sum_{j=1}^F \exp(-\beta U(j))}{F}$;
3. Continue with the conventional CBMC-algorithm as in Ref.,^{85,153–156} compute the Rosenbluth weight $W^{\text{ext}} = \prod_{k=2}^m w_k^{\text{ext}}$ where k runs over the beads of the chain;
4. Accept the insertion with the probability

$$P_{\text{ins}}^{\text{acc}} = \min \left(1, \frac{w_1^{\text{ext}}}{V \rho(x_n, y_n, z_n)} \frac{\exp(\beta \mu) V q W^{\text{ext}}}{N + 1} \right). \quad (2.9)$$

in which V is the volume of the box, μ is the chemical potential and q is the kinetic contribution to the partition sum.

The removal of a chain ($N \rightarrow N - 1$) is almost equivalent:

1. The position of the first bead of the selected molecule becomes the first trial position with coordinates (x_1, y_1, z_1) . Generate $F - 1$ others according to the distribution $\rho(x, y, z)$ and compute the energies $U(1), U(2), \dots, U(F)$
2. Continue with the conventional CBMC-algorithm (for an old configuration) and compute the Rosenbluth weight W^{ext}
3. Accept the removal with the probability

$$P_{\text{rem}}^{\text{acc}} = \min \left(1, \frac{V\rho(x_1, y_1, z_1)}{w_1^{\text{ext}}} \frac{N}{\exp(\beta\mu)VqW^{\text{ext}}} \right) \quad (2.10)$$

In Ref.¹⁵⁹ we have shown that this algorithm satisfies detailed balance.

2.4.2 Adsorption isotherm scaling

Sampling efficiency is further improved by artificially weakening the Au-S interaction. We have shown in Ref.¹⁵⁹ that the precise value of $\epsilon_{\text{Au-S}}$ is not important and that isotherms can be rescaled for other values of $\epsilon_{\text{Au-S}}$ under the following assumptions:

1. Molecules are adsorbed to a surface in a single layer;
2. The main contribution to adsorption energy comes from the headgroup-sorbate interaction;
3. Mutual interactions between adsorbed molecules mainly depend on their distances in the direction parallel to the surface.

Assume that we simulate two systems with different values for the Au-S interaction $\epsilon_{\text{Au-S}}^{(1)}$ and $\epsilon_{\text{Au-S}}^{(2)}$. Then the first system at chemical potential $\mu^{(1)}$ is equivalent to the second one at the chemical potential $\mu^{(2)}$ with

$$\mu^{(2)} = \mu^{(1)} + U_m^{(2)} - U_m^{(1)} + k_B T \ln \left(\frac{U_m^{(2)}}{U_m^{(1)}} \right)^\alpha, \quad (2.11)$$

where U_m is the effective potential well-depth ($U_m = -4.42\epsilon_{\text{Au-S}}$ on Au (111), and $U_m = -4.28\epsilon_{\text{Au-S}}$ on a NC); and α is an exponent close to 0.5 (for the HK potential, and thus in this work, $\alpha = 0.55$). Eq. (2.11) is exact when the above conditions are fulfilled; the estimate $\alpha \approx 0.5$ is based on a second-order Taylor expansion of the (effective) adsorption potential around the minimum. The reader is referred to Ref.¹⁵⁹ for the rigorous statistical mechanics derivation and numerical verification of this approach.

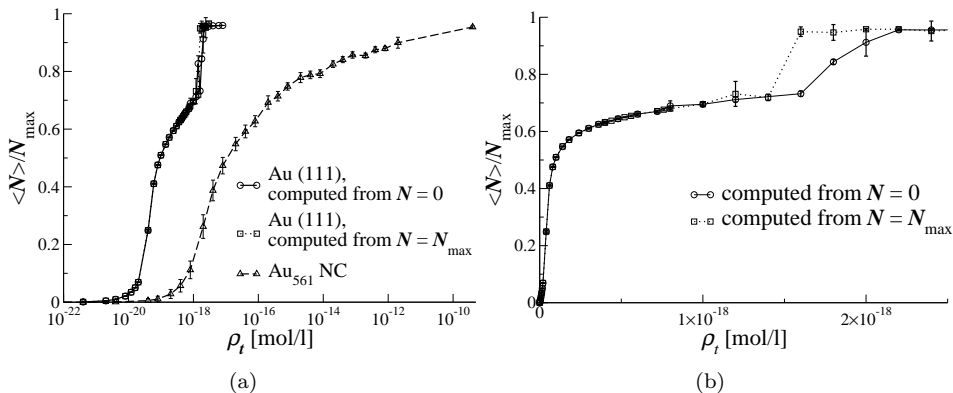


Figure 2.7: (a) Adsorption isotherms for SC3 on a flat Au (111) surface and on an Au₅₆₁ NC in vacuum at $T = 300$ K. (b) Adsorption isotherms for SC3 on a flat Au (111) surface plotted on a linear scale. LJ parameters for the Au–S interaction are $\epsilon/k_B = 2795$ K and $\sigma = 2.65$ Å.

2.5 Adsorption of alkylthiols to Au NCs and to Au (111) surfaces

In this section we present simulation results on the adsorption behaviour of alkylthiols on flat Au surfaces and on Au NCs. We consider two thiol types: SC3 and SC8. To determine the effect of the solvent, we computed adsorption isotherms with and without solvent (vacuum).

Adsorption of SC3 and SC8 in vacuum

By imposing varying surfactant fugacities in separate grand-canonical MC simulations, we determined adsorption isotherms for SC3 and SC8 thiols on Au₅₆₁ NCs and on flat Au (111) surfaces at $T = 300$ K. For these type of simulations, we only considered the thiol reservoir in Fig. 2.5. For both gold systems, we present data where we used $\epsilon/k_B = 2795$ K and $\sigma = 2.65$ Å for the LJ interaction between Au–S (see Table 2.1).

We start the discussion with the SC3 thiol. Comparing the flat surface isotherm to the one for a NC (Fig. 2.7), we see that adsorption at the (111) surface starts at lower thiol concentrations and that the transition to the fully covered surface as a function of ρ_t is much sharper. The first observation is a consequence of the edged nature of the NC surface and the relatively small (111) facets. For this reason, the effective surface–thiol interaction for NCs is lower than for flat Au (111) and therefore thiol adsorption starts at higher ρ_t for NCs. The slower transition to the maximum loading N_{\max} on an NC also is a result of

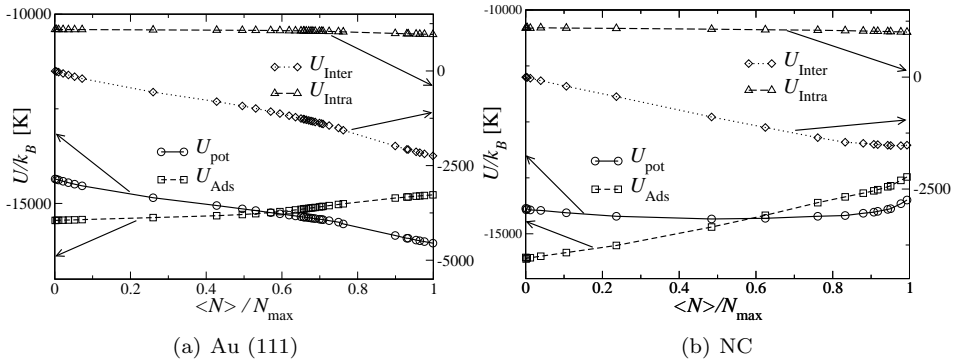


Figure 2.8: Plot of interaction energies per SC3 molecule as function of coverage on a flat Au (111) surface (a) and on an Au₅₆₁ NC (b) in vacuum: total potential energy U_{pot} ; total interactions with the gold substrate U_{Ads} ; interaction energy with other thiol molecules U_{Inter} ; and intramolecular bonded interactions U_{Intra} . Note that the first two terms are plotted on the left vertical axis, while the latter two are plotted on the right one.

its convex shape. When alkylthiols adsorb to flat Au (111) surface, their hydrocarbon tails interact favourably with each other, while on the NC surface these interactions cannot be maintained over the entire surface due to the curvature of the NC. The favourable mutual tail-tail interactions lead to an extra driving force for thiol adsorption and thus make the adsorption isotherm steeper. To verify this effect quantitatively, we plot the interaction energies per adsorbed thiol molecule $\langle U \rangle / \langle N \rangle$ versus coverage in Fig. 2.8. Due to the stronger intermolecular interactions, the total potential energy decreases with increasing loading on the flat Au (111) surface.

For the flat Au (111) surface systems there is a considerable amount of hysteresis between adsorption isotherms computed starting from fully covered ($N = N_{\text{max}}$) surfaces or from empty ($N = 0$) surfaces (see Fig. 2.7(b) where we plotted the isotherms on a linear horizontal axis scale). This points to a first order transition from a 2D liquid to a 2D crystal phase, already observed in experiments.¹⁸⁷ In the crystal phase, sulfur atoms form a well-ordered hexagonal overlattice with an S-S spacing of $\approx 5 \text{ \AA}$ and aliphatic chains stand almost upright and aligned, see Figs. 2.9(a) and 2.9(c). In the liquid phase, thiol heads arrange without a pattern and carbon chains lie closer to the surface, see Figs. 2.9(b) and 2.9(d). Both phenomena are in good agreement with experimental observations on self-assembled monolayers of thiols on Au (111).^{171,187} To illustrate the sampling difficulties around the transition point, we plotted the number of adsorbed thiols as a function of the number of MC cycles in Fig. 2.10. As nucleation and melting are spontaneous events and simulation time is limited, most of the time, the

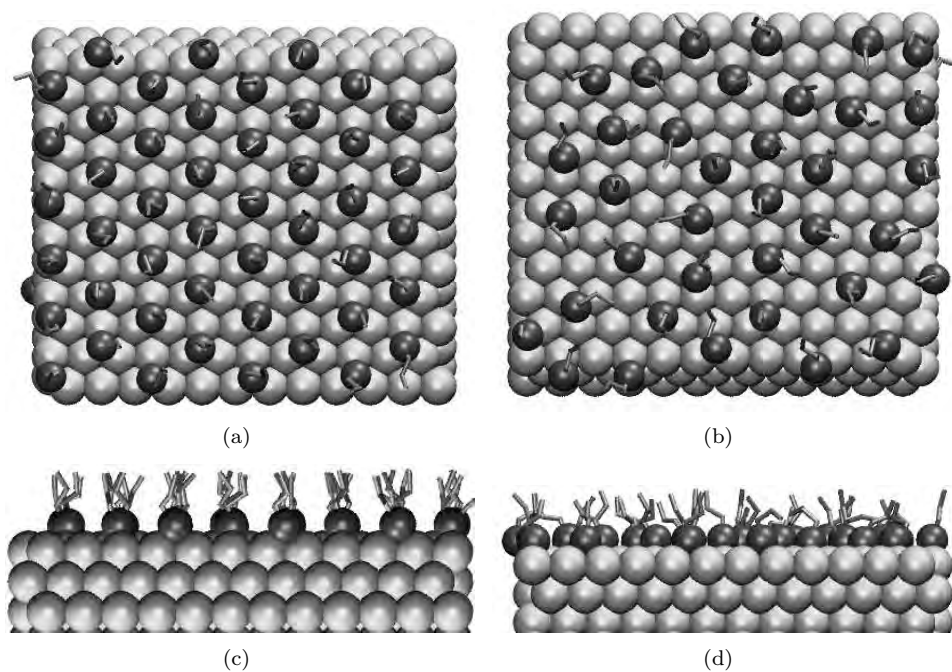


Figure 2.9: SC3 on Au in 2D-crystal (*a,c*) and in 2D-liquid (*b,d*) phases. Gold atoms are represented as large light balls, thiol heads as small dark balls and carbon chains as thin lines. (*a,b*): Top view. (*c,d*): side view. Note that the sulfur atoms are highly organized in the crystal phase (*a*) and do not show a clear structure in the liquid phase (*b*).

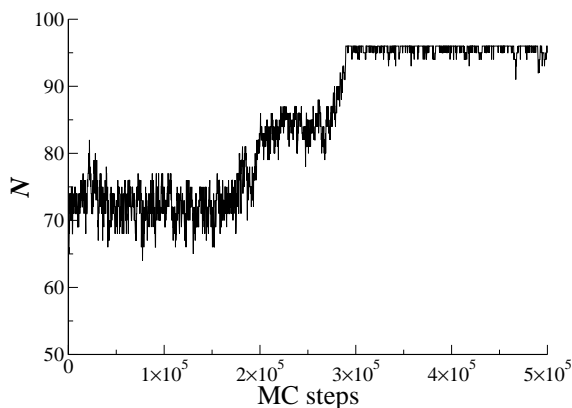


Figure 2.10: Typical behaviour of a GCMC simulation of SC3 on Au (111) around the transition point when the simulation starts from a low coverage. The first terrace corresponds to a 2D-liquid phase, then a phase transition occurs on one of the sides of the slab (second terrace, fictive state due to simulation conditions) and finally the thiols 2D-crystallize on the second side (third terrace).

system resides in one of the (meta)stable states that are separated by sharp transitions.¹⁵⁰ We did not observe this hysteresis loop in the NC isotherms. Again, this is a result of the convex shape of the Au NC.

We also computed the adsorption isotherm of SC3 for infinitely smooth gold substrates in vacuum: the Hautman-Klein potential¹⁹² and the coarse-grained potential from Section 2.3 were used to mimic an infinitely smooth Au (111) slab and Au₅₆₁ NC, respectively. As expected, these isotherms have a similar concentration range where thiol adsorption takes place compared to the explicit atom case, see Fig. 2.11. In the infinitely smooth flat Au surface system, the 2D liquid phase is more stable than for the explicit atom system, and the height of the jump in coverage around phase transition to the 2D solid is smaller. Obviously, a 2D liquid can be compressed much more on an infinitely smooth surface than on a rough surface with explicit atoms. For the same reason, adsorption isotherms are steeper in the full-atom case.

Comparing the SC8 isotherms (Fig. 2.12) to the ones for SC3 (Fig. 2.7), we observe that adsorption of the longer chain thiol starts at lower densities than for shorter chain thiols. This is due to the larger number of attractive Au-CH_x interactions for SC8. Comparing the NC SC8 isotherm to the flat (111) surface SC8 isotherm, we again see that adsorption for the flat surface starts at lower concentrations than for the NC and that the concentration range where adsorption takes place is much narrower for the flat surface system. This can be explained by the same arguments as for SC3.

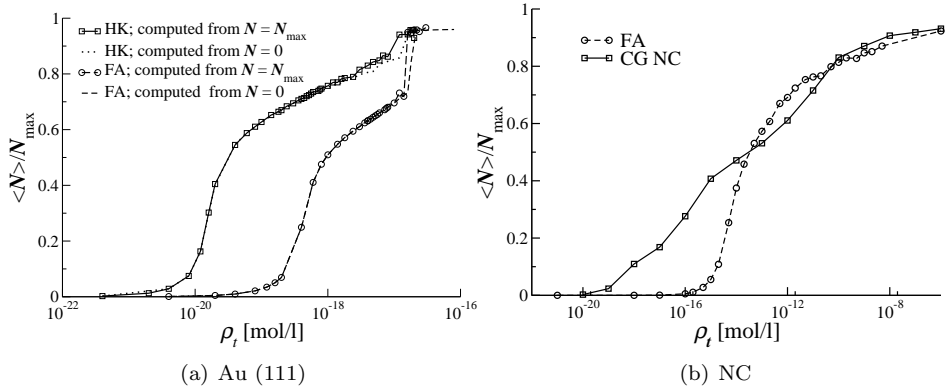


Figure 2.11: Adsorption isotherm for SC3 at $T = 300$ K to an infinitely smooth gold (111) (a) and a Au_{561} NC (b) surface in vacuum computed using the Hautman-Klein (HK) potential and the effective potential from Section 2.3, respectively. The isotherms are compared to the full-atom (FA) results from Fig. 2.7. The adsorption isotherms were computed by increasing and decreasing the loading.

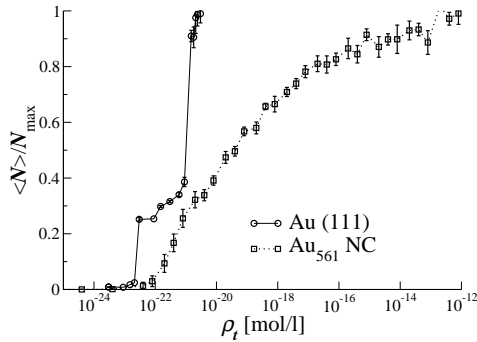


Figure 2.12: Adsorption isotherm for SC8 on a flat Au (111) surface and on an Au_{561} NC in vacuum at $T = 300$ K.

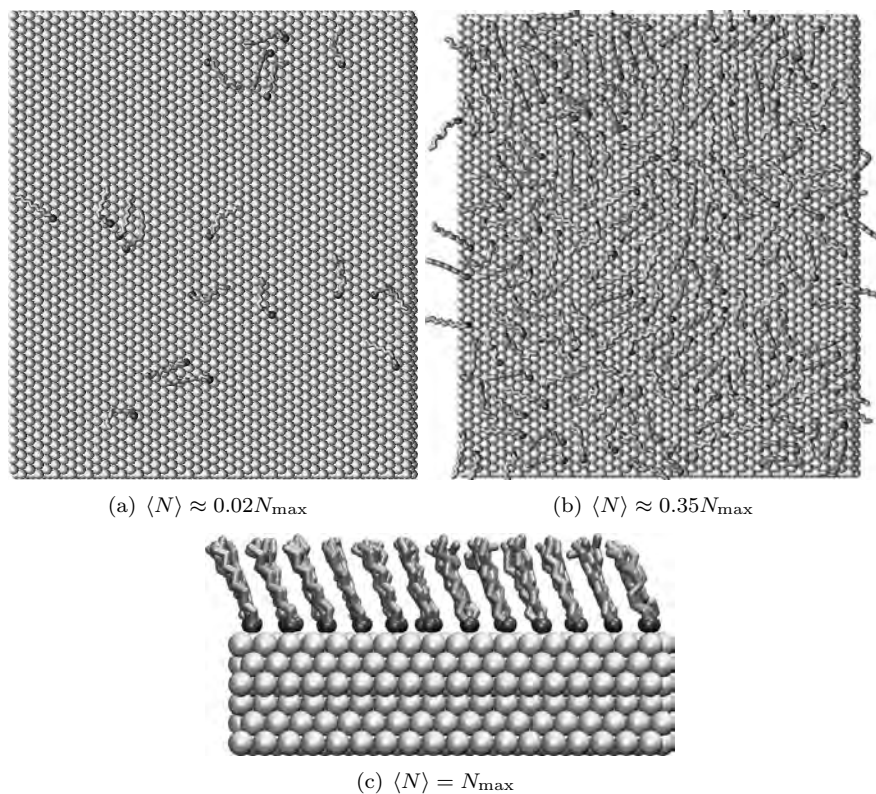


Figure 2.13: Phases of SC8 adsorbed on Au (111) at $T = 300$ K. (a, b) : Top view; (c) : side view; top view similar to Fig. 2.9(a).

The phase behaviour of SC8 on flat surfaces is more complicated compared to SC3 (or to the NC case), see Fig. 2.12. We observe two jumps in the isotherm. During the second jump the coverage doubles. At this point the self-assembled monolayer is formed. At lower loadings, various 2D phases were observed for SC10 due to different packing of alkyl chains on the surface.¹⁸⁸ The 2D liquid phase as in Fig. 2.9 is metastable for long chain thiols in vacuum; the three stable phases are shown in Fig. 2.13. Again, such phase behaviour is not present in the NC systems we studied.

Adsorption of SC3 and SC8 in hexane solution

Using (semi) grand-canonical Monte Carlo (GCMC), we computed adsorption isotherms for the alkylthiols SC3 and SC8 on a Au_{561} NC as well as on a Au (111) surface with explicit solvent (n-hexane). This means that both the solvent

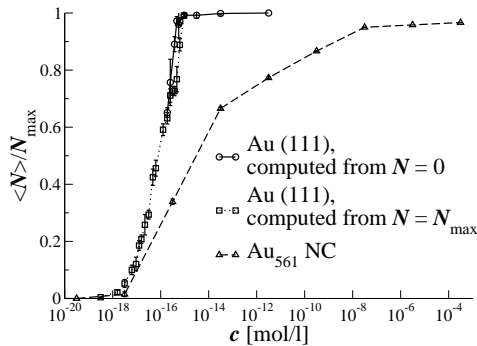


Figure 2.14: Adsorption isotherm for SC3 on a flat Au (111) surface and on an Au_{561} NC in n-hexane at $T = 300$ K.

and the thiol reservoirs (Fig. 2.5) are switched on. Again, for both systems we used $\epsilon/k_B = 2795$ K and $\sigma = 2.65$ Å for the LJ interaction between Au–S.

The SC3 isotherms for the flat Au (111) surface and for the NC are shown in Fig. 2.14. We again observe that adsorption of SC3 on the Au (111) surface starts at lower c_t than on the NC. Similar to the vacuum case, the concentration range of adsorption is considerably larger in NC systems compared to flat gold systems. Explanations for both are given in the previous subsection. The flat Au (111) SC3 system in explicit solvent also shows the hysteresis loop at high $\langle N \rangle$, pointing to a phase transition from a 2D liquid to a 2D solid, already described above for the vacuum case.

There are, however, differences between SC3 systems with or without solvent. For both the NC and the flat surface, the isotherm is shifted towards higher thiol concentrations. We explain this by a competition effect between adsorption of solvent and thiols to gold. The shift is moderate because hexane–gold interactions are far weaker than thiol–gold interactions. An illustration of this competition effect is the difference in adsorption behaviour at low ρ_t between vacuum SC3 systems and those with explicit solvent. In agreement with experiments,¹⁸⁹ the explicit solvent isotherm can be fitted to a Langmuir adsorption isotherm, whereas this is not possible for the vacuum isotherms (see Fig. 2.15). At low loadings, the vacuum isotherm increases superlinear (i.e. $d^2 \langle N \rangle / d\rho_t^2 > 0$, see Fig. 2.15(b)), while the Langmuir isotherm behaves sublinearly ($d^2 \langle N \rangle / d\rho_t^2 < 0$). This difference can be explained as follows. At low loadings in vacuum, alkylthiols gain energy from the attractive interactions between tails, hence the superlinear increase of the isotherm. In hexane solution, energetic gains from surfactant tail-tail interactions are accompanied by energy penalties associated with the loss of solvent–solvent and solvent–surfactant interactions. Thus, effectively, the favourable surfactant tail-tail interactions play a less pronounced role in the explicit solvent systems

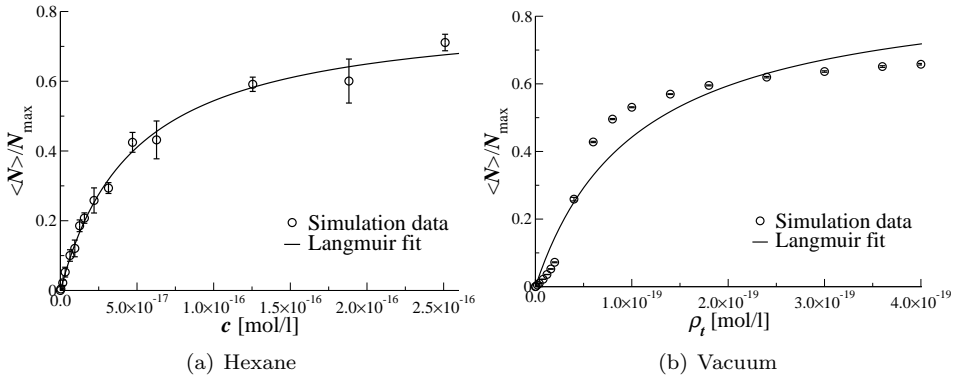


Figure 2.15: Langmuir-fit to the lower part of the adsorption isotherm of SC3 on a gold slab in hexane (a) and vacuum (b).

and therefore the alkylthiol adsorption isotherm shows Langmuir behaviour.

For adsorption of SC8, the solvent effect, or equivalently the shift of the isotherm when including n-hexane as a solvent, is more strongly pronounced (compare Fig. 2.12 to 2.16). If we compare Fig. 2.12 to Fig. 2.16 we see that various 2D phases¹⁸⁸ disappear in the explicit solvent system and the 2D liquid phase is stable in contrast with the vacuum case. In Fig. 2.16 we included the SC8/n-hexane/Au (111) Langmuir isotherm, derived from experiments of Ref.¹⁸⁹ Our isotherm for a flat Au (111) surface also has a Langmuir shape. Obviously, the concentration range of adsorption derived from our simulations (of flat Au (111) as well as of NC) is orders of magnitude lower than the experimentally observed adsorption isotherm for SC8. From the results presented in this chapter, we know that the range of adsorption is mainly determined by the interaction strength between Au and S. Using adsorption isotherm scaling (Section 2.4.2), we estimate the Au-S interaction strength at $\epsilon/k_B \approx 1000$ K for the experimental isotherm instead of the value of $\epsilon/k_B \approx 2795$ K used in our simulations. This raises the question whether or not the Au-S interaction is really that strong as modeled by Hautman and Klein,¹⁹² Landman *et al.*¹³¹ and by us. A possible answer lies in the nature of the Au-S interaction. This interaction could either be a thiolate bond (formed by removal of the thiol-hydrogen)¹⁷⁴ or physisorption of the thiol group to the gold surface. It is still unclear which of the possibilities prevails.¹⁷⁵ The thiolate adsorption energy was used to derive Au-S interaction potentials in previous simulations (for example in Refs.^{131,192}). This interaction is three to four times as strong as for the thiol-gold interaction.¹⁷⁴ Assuming that the SC8 adsorption measurements¹⁸⁹ are accurate, our adsorption isotherm scaling method suggests that alkylthiols are physisorbed to the Au (111) surface rather than chemisorbed in an apolar solvent.

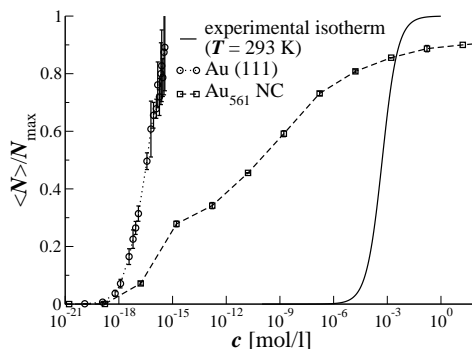


Figure 2.16: Adsorption isotherm for SC8 on a flat Au (111) surface and on an Au₅₆₁ NC in n-hexane at $T = 300$ K, compared to the experimental SC8 isotherm on Au (111) in n-hexane¹⁸⁹ (recorded at $T = 293$ K). Note the large shift in adsorption concentration range between the simulated and the experimental isotherm. Using isotherm shifting (c.f. Section 2.4.2), we can estimate the experimental interaction strength as $\epsilon/k_B \approx 1000$ K, a factor of three lower than the value used in the simulations.

2.6 The structure of the capping layer

2.6.1 Systems in vacuum; chain melting

The properties of alkylthiol monolayers on Au (111) and nanocrystals can be described using several order parameters. We begin with the most common one, namely the radial distribution function (RDF) $g_x(r)$ for a given species x . It is defined as the ratio between the average number density $\rho_x(r)$ at a distance r from any given particle and the ideal gas density of the compound x .⁸⁵

The RDF of the thiol groups $g_{\text{SS}}(r)$ (Fig. 2.17) demonstrates the sulfur arrangement on the Au (111) surface as in Fig. 2.9(a). For a NC, there are more possible adsorption sites, leading to a reduced S-S spacing. Furthermore, on the NC, there is less structure in the arrangement of adsorbed thiol groups. The RDF between the centers of SC3 and SC6 thiol molecules on a NC at full loading is shown in Fig. 2.18(a). Interestingly, the $g(r)$ shows less structure with increasing alkyl tail length. The first three peaks of $g_{\text{SC3}}(r)$ are at 4.8, 9.5 and 13.5 Å, respectively. The second and the third peak are located close to integer multiples of the first one (9.6 and 12.4 Å). This hints to a tendency to exhibit a chain-like alignment of tails. In some simulation snapshots of short chain thiols at high loading we indeed observe formation of rows on some NC facets. Consider, e.g., a snapshot of a fully covered (coarse-grained) Au₁₄₁₅ NC (Fig. 2.18(b)). One can clearly see that surfactant tails form straight rows in the bottom part of the figure. We did not observe anything similar for long tail ligands at $T = 300$ K.

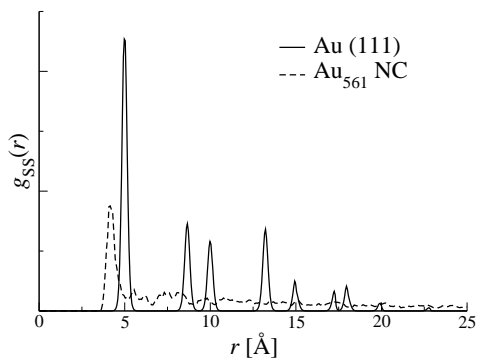


Figure 2.17: Headgroup radial distribution function $g_{SS}(r)$ for SC4 on a gold (111) surface and a Au_{561} NC at full loading.

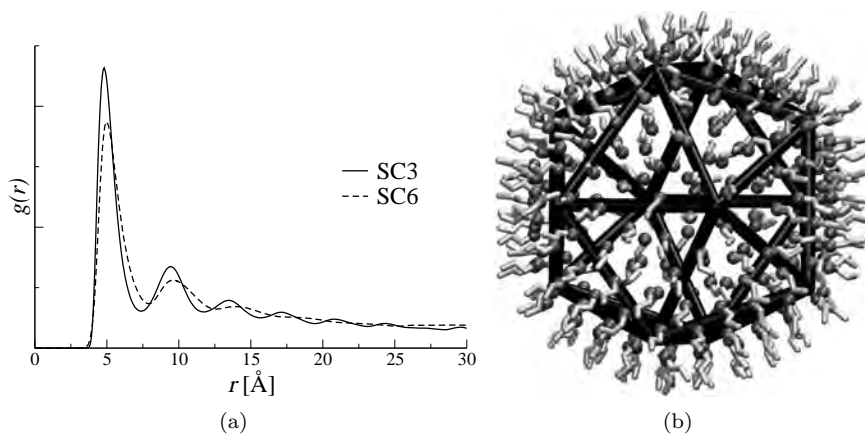
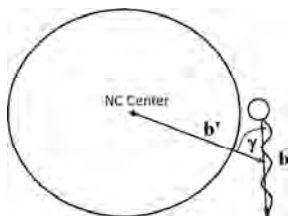
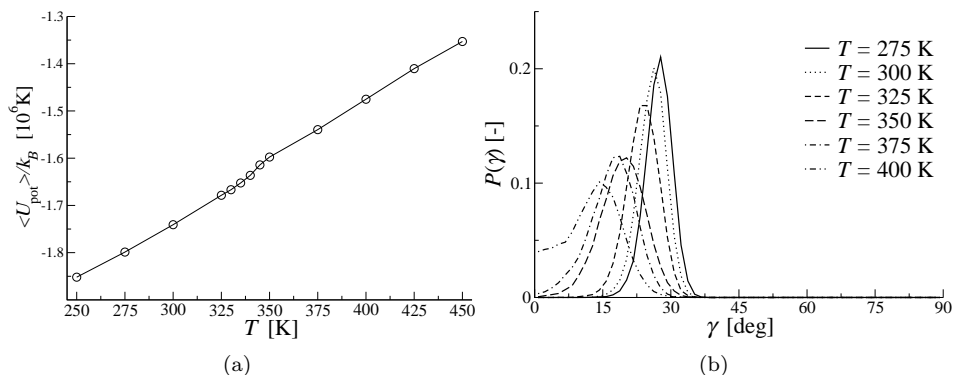


Figure 2.18: (a) Radial distribution function $g(r)$ between centers of mass of adsorbed thiol molecules on a Au_{561} NC at full loading. (b) Snapshot of Au_{1415} NC full covered by SC3 at $T = 300$ K. Computed using the effective potential; the coarse-grained NC is represented by black lines. Note the rows of alkyl tails in the bottom part of the figure.

Figure 2.19: Definition of the angular orderparameter γ on a NC.Figure 2.20: (a) Caloric curve for a SAM of SC10 on Au (111) in vacuum. (b) Angular order parameter $p(\gamma)$ for the same system at different temperatures.

Thus, the capping layer of longer chain thiols is more disordered than a capping layer of short chain ones at the same temperature. The situation is opposite on a flat Au (111) surface: having the same translational order, long chain thiols show additional orientational order that is not present for short chain ones.

We determined the orientations of the system components as follows. For each molecule, we defined the vector \mathbf{b} that connects the first segment to the last. Furthermore, for each molecule, we calculated the vector \mathbf{b}' that connects the NC center of mass to the molecule center of mass. For systems containing a gold slab, \mathbf{b}' is simply the vector $\hat{\mathbf{z}}$ normal to the surface. We subsequently determined the distribution $P(\gamma)$ of the minimal angle $\gamma \in [0, 90^\circ]$ between \mathbf{b} and \mathbf{b}' . Low values of γ represent chains that are oriented perpendicular to the surface, whereas $\gamma \rightarrow 90^\circ$ represent chains that are oriented parallel to the NC or the flat Au (111) surface, see also Fig. 2.19.

For a SAM of SC10 on Au (111), we have computed the caloric curve (potential energy as a function of temperature), see Fig. 2.20(a). A kink is clearly visible at $T = 342$ K, which points to a phase transition inside the monolayer, which

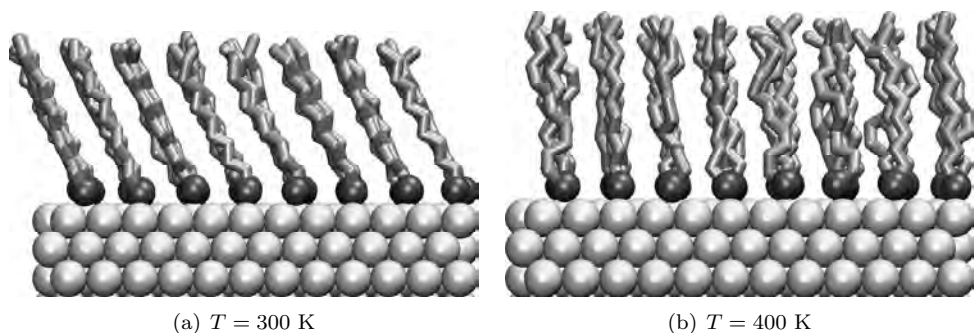


Figure 2.21: SAM of SC10 on Au (111) in frozen (a) and molten (b) state.

is often referred to as chain melting. We plot $p(\gamma)$ at different temperatures in Fig. 2.20(b). The orientations have a well defined peak, which shifts to the right with increasing temperatures by $2^\circ/25$ K. From $T = 325$ to 350 K we observe a sudden broadening of this peak which is correlated with the chain melting, and we conclude that this transition is accompanied by reduction of orientational order in the SAM. Fig. 2.21 shows the SAM in “molten” and “frozen” state. A similar transition takes place on a NC at much lower temperatures (≈ 275 K), which is an effect of the reduced tail-tail interactions on a curved surface. Fig. 2.22 shows NCs in “molten” and “frozen” state. In the frozen state, tails of capping molecules form bundles perpendicular to certain facets, while in the molten state they form a homogeneous layer around the NC core. We will discuss the associated caloric curve in Section 2.6.3. The transition described here has been observed first in MD simulations of Luedtke and Landman^{131,132} and later confirmed experimentally.^{136,209,210}

2.6.2 Systems with explicit solvent

In this section we address the structural properties of thiol and solvent molecules in explicit solvent systems for a gold NC and a flat Au (111) surface. We consider two thiols of different chain length (SC4 and SC10) to address tail length effects. Furthermore, we investigate how the structure of the systems is affected by the loading. Therefore, we consider both surfactants at 30%, 60% and 100% of the maximum surface coverage N_{\max} . From NVT simulations of Au NCs and Au slabs, (partially) capped by thiols in solution, we determined the average orientations of the thiol chains with respect to the Au surface. The solvent structure was analyzed using the radial distribution function $g(r)$ of the solvent, with r the distance from the center of a hexane molecule to the center of the NC or the gold slab.

The orientational distributions of SC4 and SC10 thiols on NCs and flat Au (111)

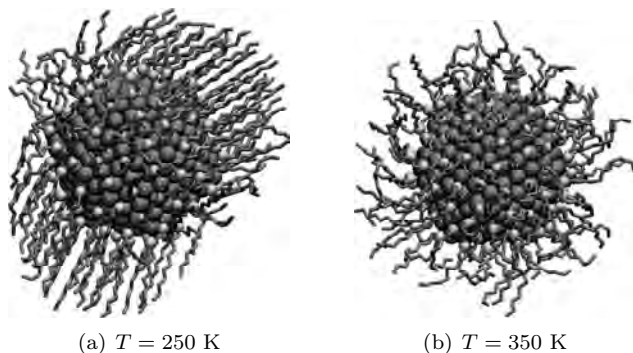


Figure 2.22: Gold NC capped with decane-thiol at two different temperatures. Gold atoms are represented by large dark spheres, thiol heads by small light spheres and carbon segments by lines. (a) The capping layer is frozen ($T = 250$ K). (b) The capping layer is molten ($T = 350$ K).

surfaces are shown in Fig. 2.23. For both Au (111) and the NC, the distributions $P(\gamma)$ of the adsorbed SC4 thiols are almost random at low loading. The distribution $P(\gamma)$ shifts to smaller angles γ by increasing the loading, and at the highest loading it is peaked at small values of γ , indicating that most of the SC4 ligands are oriented perpendicular to the surface. The average orientation of the longer chain SC10 thiols on a NC (see Fig. 2.23(d)) hardly changes as a function of loading (see also the right panel of Fig. 2.23). As our NC is quite small, there is simply not enough space on the surface to accommodate for thiol chains lying parallel to the surface as we observe it for flat Au (111) surfaces (see Fig. 2.23(c)). At full coverage (SAM-regime), SC10 molecules form a 26° angle with the surface normal. Note that this is similar to a SAM of SC8 in vacuum (Fig. 2.13(c)).

Evidently, long chain thiols have a higher degree of configurational freedom compared to the short chain thiols. Therefore, they can lie flat on the Au (111) surface more easily than short chain thiols. For this reason, at low loadings, the SC10 molecules already occupy the Au surface almost completely and SC4 molecules do not.

The solvent structural data for the NC (SC4 and SC10) are shown in Fig. 2.24. At low and intermediate loadings of both SC10 and SC4, the first shell of solvent molecules is present near the Au surface, at regions where there are no thiols. Here, a large fraction orients itself parallel to the Au surface, maximizing the favourable interaction with gold. At high loadings, these vacant sites are occupied by thiols and therefore the first n-hexane solvation shell is shifted to larger distances r .

Fig. 2.24(b) shows that, at low and intermediate loadings of SC4, there are some vacant regions on the flat gold (111) surface where solvent molecules are

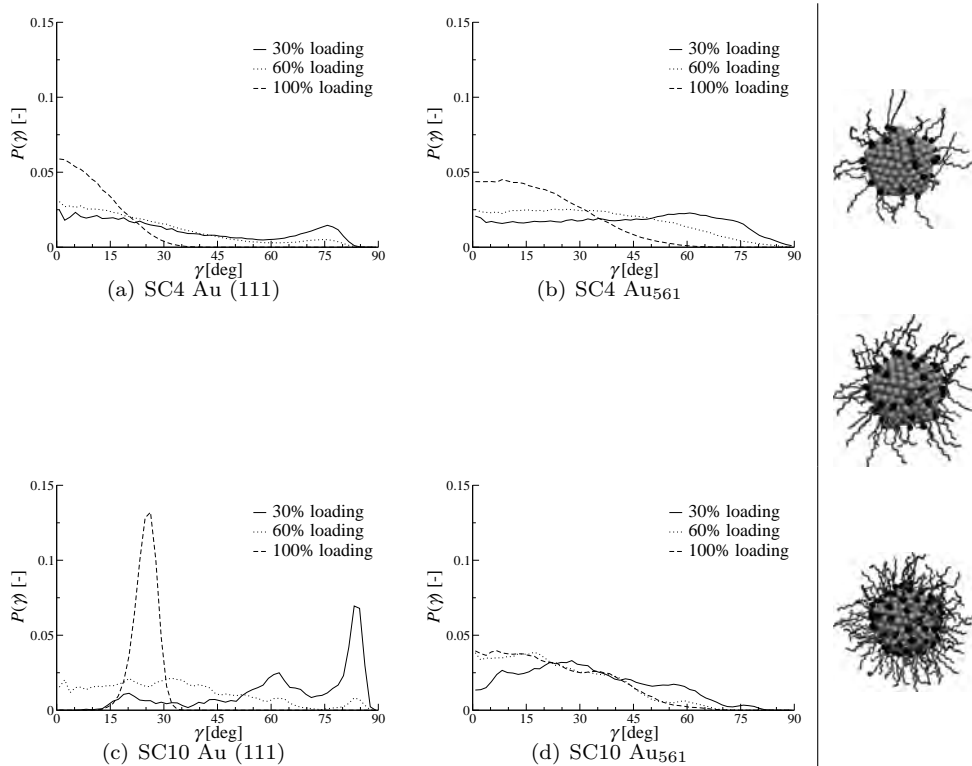


Figure 2.23: Thiol orientational distributions for alkylthiol-hexane systems as a function of loading on a gold (111) slab (left) and on a Au₅₆₁ NC (center). Top: SC4 system. Bottom: SC10 system. The right panel shows simulation snapshots taken from the SC10 simulations on a NC at increasing loading (from top-right to bottom-right).

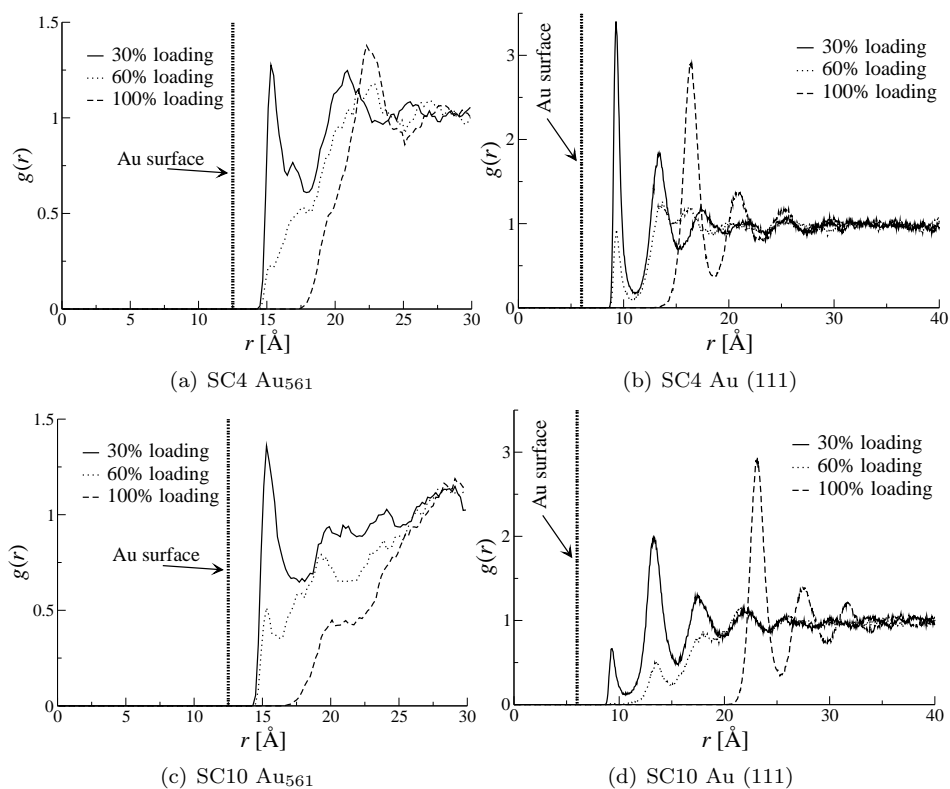


Figure 2.24: Solvent radial distribution functions $g(r)$ between the NC center of mass (or slab center, respectively) and the center of the hexane molecule for alkylthiol-hexane systems with (a,c) a Au₅₆₁ NC and (b,d) a gold (111) slab at $T = 300$ K. (a,b) SC4 system. (c,d) SC10 system.

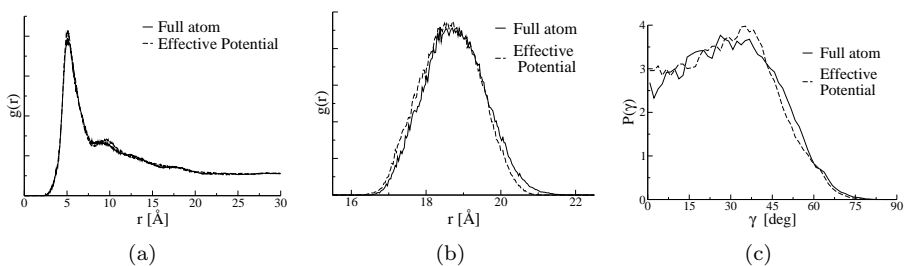


Figure 2.25: Orderparameters at $T = 300$ K calculated using the full atom model and the effective potential: (a) RDF of surfactants, (b) RDF between NC center and surfactants, (c) orientational distribution.

located. However, already at low SC10 loadings on flat Au (111), the surface is covered (almost) completely, leaving no room for solvent molecules to reside near the Au surface. Therefore, the first peak of $g(r)$ at 30% loading for SC10 is low, see Fig. 2.24(d). By increasing the loading of SC4 or SC10 surfactants, the SAM becomes impenetrable for solvent molecules and thus the first solvation shell is shifted to larger r .

2.6.3 Comparison of the coarse-grained and the full-atom models

As the main reason for coarse-graining the interactions between a NC and a united CH_x or SH atom is to reduce the computation times, we investigated the computational efficiency of the potential defined by the Eqs. (2.7) and (2.8) and compared it to the full summation in Eq. (2.6). We found that an evaluation of the effective potential is on average 50 times faster than the explicit summation.

We performed MC simulations in the canonical ensemble (constant number of particles, volume and temperature) for a Au_{561} NC covered with 120 decanethiol molecules for both models. Several order parameters were compared at $T = 300$ K: the radial distribution function (RDF) of surfactant centers of mass, the RDF between NC and surfactants, and the orientational distribution $P(\gamma)$ of surfactants. The results are presented in Fig. 2.25. We conclude that the structure of surfactants is well described by the coarse-grained model.

For the same system, we have calculated the caloric curve, i.e. the potential energy as a function of temperature. The energies (in units of the Boltzmann constant k_B) computed using the effective potential are approximately 100000 K (6%) lower than the ones computed using the full-atom model, see Fig. 2.26. Nevertheless, the shapes and slopes of the two caloric curves are similar. The non-linear, noisy behaviour of both caloric curves around 280 K (encircled in the figure) is due to the melting of the monolayer, see Figs. 2.22(a) and 2.22(b).

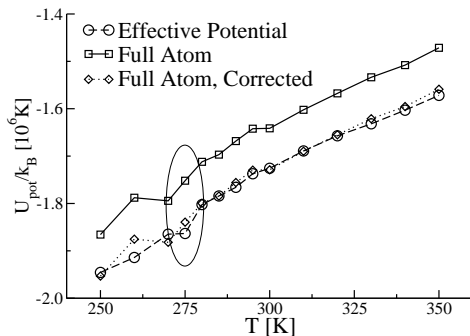


Figure 2.26: Caloric curves for an Au_{561} capped with 120 decane-thiol molecules. The vertical offset is mainly due to cutoff in the full-atom model Eq. (2.1). The corrected curve is obtained by adding the cutoff energy back to the full-atom curve.

At low temperatures, surfactant chains are aligned, while at high temperatures they are disordered. Experiments suggest that this transition should occur slightly below room temperature for decane-thiol.¹³⁶ Previous simulations yield transition temperature of 294 K for dodecane-thiol on a larger NC.¹³¹ We can conclude that our coarse-grained model is consistent with both experiments and full-atom simulations.

It is important to note, that in the full-atom model the LJ-potential was truncated and shifted. We applied a cutoff radius of 12 Å. This yields a shift of each Au-S interaction (which has the largest contribution to the total energy) by $-1.3K$, i.e. $-1.3 \times 120 \times 561 = -87516K$ in total. We have added this number back, and obtained a very good agreement with the full atom model, see Fig. 2.26. Recall that the effective potential was fitted to the full LJ-potential; and no cutoff was applied in simulations with the coarse-grained interactions.

A rough estimate can be made for the efficiency of our coarse-grained potential. In the considered system, there are 561 gold atoms and $11 \times 120 = 1320$ pseudoatoms (SH, CH_x). To calculate the total potential energy, 561×1320 NC-capping layer interactions and 1320×1320 interactions within the capping layer must be computed. Therefore, coarse-graining the NC-capping layer interactions can save $\approx 30\%$ of the computation time. This percentage increases with larger NC size since the number of gold atoms scales with the volume while the number of surfactants scales with the surface area of the NC. The simulations with the effective potential were more than twice as fast than the full-atom ones. The main reason for this additional gain is the higher acceptance probability for trial moves in the coarse-grained model, yielding a faster equilibration and better sampling. Surface roughness causes lower acceptance probabilities in the full-atom model (see also Section 2.3).

2.7 Selective adsorption to Au NCs and Au (111) surfaces

To investigate the composition of co-adsorbed alkylthiols, we carried out simulations of binary thiol mixtures adsorbed on gold in presence of the explicit solvent (n-hexane) for both a flat Au (111) surface and a NC. We compare the results to those from simulations without solvent. The total number of thiol molecules is kept fixed. Identity changes between different thiols are performed (semi grand-canonical MC). During simulations with explicit solvent, we also allowed for solvent molecule exchange moves with the solvent reservoir (see Fig. 2.5), but we did not allow for identity changes between solvent and surfactants. We discuss the following mixtures: SC3–SC4; SC3–SC7; SC9–SC10 and SC9–SC11.

Shevade *et al.*¹⁵⁸ performed similar simulations in which they assumed that the alkylthiol solubility does not significantly change as a function of chain length, a situation resembling vacuum conditions. However, in Fig. 2.6 we showed that the Henry coefficient of thiols in n-hexane increases exponentially with the tail length, and this will influence the selectivity. We performed simulation with *and* without solvent to assess solvent effects.

For the system containing the gold structure, we computed the average number of shorter chain thiols (type 1) and longer chain thiols (type 2), $\langle N_1 \rangle$ and $\langle N_2 \rangle$, respectively, as a function of the ratio of their fugacities f_1 and f_2 from the simulation data. This ratio is converted to the concentration ratio $\langle N_1 \rangle / (\langle N_1 \rangle + \langle N_2 \rangle)$ for the other simulation box according to the procedure outlined in section 2.4. To investigate how NC size affects selective adsorption, we studied two NCs: Au₅₆₁ and Au₁₄₁₅ that have $N_{\max} = 124$ and $N_{\max} = 212$ adsorbed thiols at their surfaces, respectively. The simulations with flat Au (111) surfaces were also performed at full coverage ($N_{\max} = 96$ thiol molecules, arranged in a hexagonal overlattice).

The results are shown in Figs. 2.27 and 2.28. In vacuum, the longer chain thiol is always preferentially adsorbed compared to the shorter chain one. This effect is more pronounced for longer alkyl chains and increases with difference in chain length.¹⁵⁸ This selectivity can be explained as follows. When a thiol molecule is transferred from the ideal gas reservoir to the system with gold structure, it gains energy from interactions with gold and from Van der Waals interactions between carbon tails. This energy gain is larger for longer chain thiols and, therefore, they are preferably adsorbed. The difference in these energy gains is the driving force for selectivity. On Au (111) the surfactants are ordered and adopt a tilted configuration, while on a NC this tilted structure is frustrated and destroyed by the convex shape of the NC. This frustration becomes less for larger NCs. Therefore, the selectivity is strongest on the flat (111) surface and least on the small NC (compare the data for Au₅₆₁ and Au₁₄₁₅ NCs in Fig. 2.27).

The situation is crucially different for systems with explicit solvent. Longer chain thiols are again preferred over the shorter chains a flat Au(111) surface, but

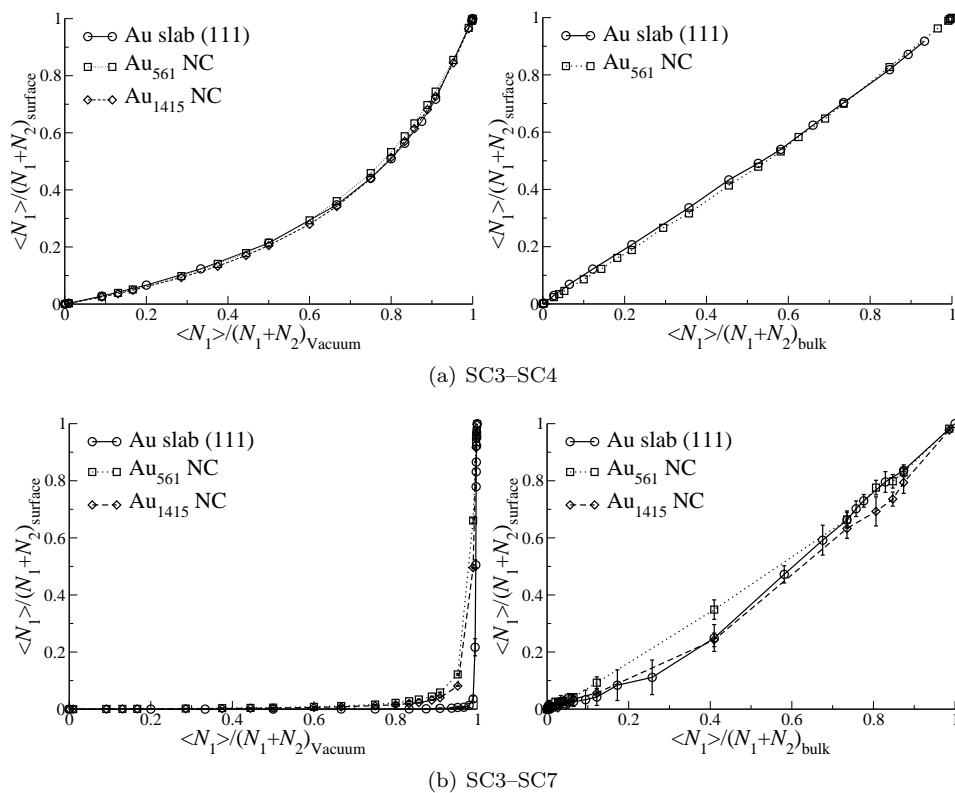


Figure 2.27: Adsorption selectivities for different alkylthiol pairs: (a) SC3-SC4 and (b) SC3-SC7. Left: Results from vacuum simulations. Right: Results from simulations with explicit solvent.

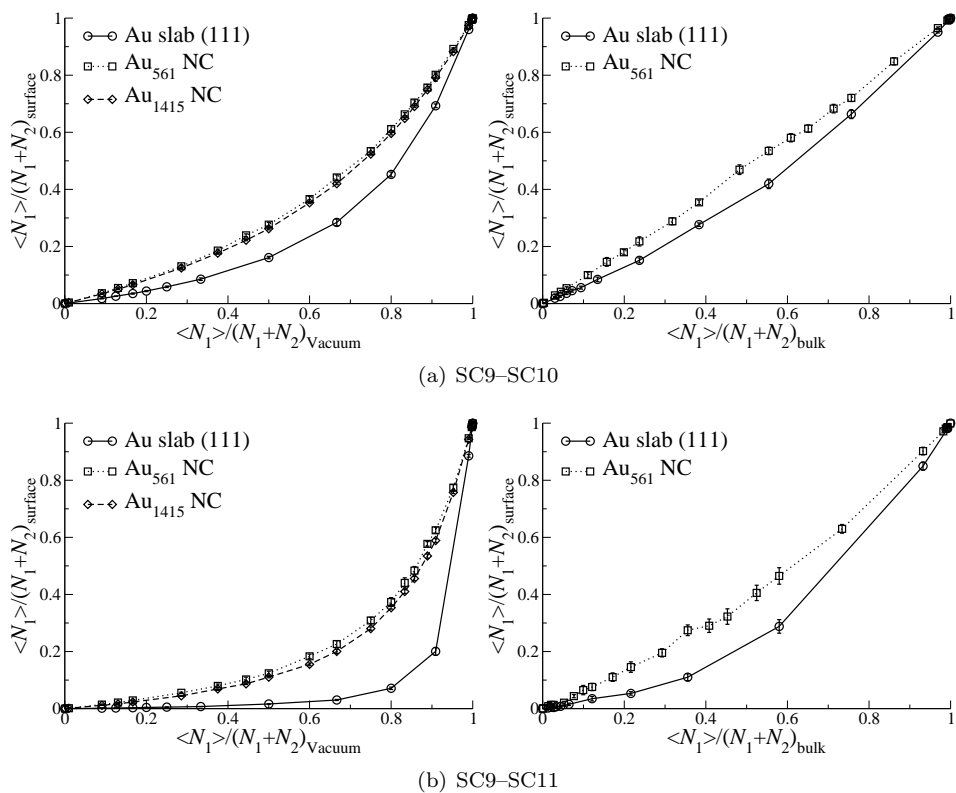


Figure 2.28: Adsorption selectivities for different alkylthiol pairs: (a) SC9-SC10 and (b) SC9-SC11. Left: Results from vacuum simulations. Right: Results from simulations with explicit solvent.

the effect is much less pronounced than in vacuum. On NCs, selectivity is hardly present at all. To understand this, consider the setup of our simulations in Fig. 2.5. When attempting a ligand exchange, we have to transfer a thiol molecule from the bulk solution to the system with gold structure for both thiol types, and compare the energetic gains due to this transfer. These energy gains originate from interactions with gold and from Van der Waals attraction of aliphatic chains, but they are accompanied by the loss of attractive solvent–gold and solvent–thiol interactions. Gold–thiol interaction are almost identical for both thiol types and hence not significant for selectivity. Aligned tails on a flat surface have a stronger effective interaction than they would have in a solution, and this difference increases with chain length. On a NC, tails do not benefit from the arrangement in this way. Therefore, only tail–tail interactions between alkylthiols on the flat (111) surface have a significant contribution to the difference in energetic gains. This explains why NCs show almost now selectivity and the selectivity on flat (111) surfaces is weaker than in vacuum.

Our simulation results show that a solvent plays a large role in the selective adsorption of alkylthiols to gold structures. Such solvent effects have previously been overlooked.¹⁵⁸ For the exchange of thiol capping layers on NCs, the key property to adjust is the concentration ratio of two thiol types in solution, not so much the chain length. Another possibility would be to use surfactants with different headgroups. Exchange will then be observed if the two headgroups exhibit different adsorption behaviour.

2.8 Conclusions

We have computed the total interaction energy between an icosahedral gold NC and Lennard-Jones particles. This interaction can be described by an effective 10-4 potential Eq. (2.7) with an isotropic (constant) value for τ . It turns out that the effective interaction is the same for all icosahedral Au–NCs with more than 500 atoms. The interaction strength (U_{\min}) is highly anisotropic as a result of the faceted surface. Averaging over the surface roughness, we obtained a coarse-grained interaction model Eqs. (2.7) and (2.8) that accurately describes interactions of united CH_x or SH atoms with a NC. This model was applied to a system with Au_{561} capped by decane-thiol and we found that the computed thermodynamic properties hardly differ from those computed using the full atom model.

Our adsorption studies show that the solvent plays an important role in the thermodynamic properties of thiol monolayers on both flat (111) gold surfaces and NCs. Two major solvent effects are (1) competitive adsorption between surfactants and solvents and (2) reduction of attractive interactions between aliphatic tails. Moreover, the phase behaviour of unsaturated monolayers of long chain thiols changes in presence of a solvent. Therefore, phenomena observed in vacuum may be different from those observed in solution; in the latter case the solvent

cannot be neglected in computer simulations.

Our studies of the structure of the capping layer confirm that alkyl thiols SC_x adopt a tilted confirmation in SAMs on planar gold (111) for $x > 6$ while capping layers of SC_x on nanocrystals are conformationally disordered for $x < 12$.

On the NC surface, there is more space between aliphatic tails which leads to weaker interactions and allows for a stronger interpenetration of the capping layer. This reduces the adsorption selectivity of thiol mixtures compared to the gold (111) surface and to vacuum.

Chapter 3

Adsorption of Ligands to CdSe Nanocrystals

CdSe nanocrystals (NC) capped by organic ligands are studied at the atomistic level using classical molecular simulations. We show for the first time that the NC–ligand bond strength can be explained using a simple model based on electrostatic interactions. The computed binding energies in vacuum for amine, thiol, thiolate and phosphine oxide ligands are 86.8, 34.7, 1283 and 313.6 kJ/mol, respectively. These values are in good agreement with available quantum chemical calculations and experiments. It is crucial that one corrects for the dielectric constant of the solvent used in the experiment. We also show that the amine capping layer is formed in two stages: first, amine molecules binds to a single surface cation each, and then additional amines bind to less favourable sites forming hydrogen bonds with already adsorbed ligands. The cross-over between these mechanisms can occur at ambient conditions. We speculate that this cross-over may be responsible for transitions in optical properties reported earlier. The calculated adsorption isotherms show that amine ligands desorb from the nanocrystal surface under ultra-high vacuum at ambient temperatures.

3.1 Introduction

Surface passivation of semiconductor nanocrystals (NC) by organic ligands strongly influences their properties. These ligands (also referred to as surfactants or capping molecules) accelerate or inhibit growth of some facets during colloidal synthesis, yielding a large variety of sizes and shapes.^{7,13,36,50,51,55,211–216} The solubility of NCs in a desired solvent depends on the nature of the capping layer. Typically, hydrophobic capping molecules are used during colloidal synthesis; and one has to exchange those surfactants by hydrophilic ones to make the NCs soluble in polar solvents.^{217,218} Furthermore, optical properties of semiconductor NCs strongly

depend on the nature and degree of passivation. For example, the quantum yield (QY) of CdSe NCs could be increased from 5-15% to over 50%, and in some cases to almost unity, just by adding alkylamine ligands during synthesis.^{51,52,219} Conversely, removing capping molecules from the NC surface leads to a decrease of the QY to less than 5%.^{220,221} Addition of amines to washed CdSe NCs is known to increase their QY,^{220,222} while it has no effect on the NCs that are capped by original ligands.²²³ Addition of thiols reduces the QY of CdSe NCs and increases the QY of CdTe NCs.²²⁴ Despite the evident importance, little is known on the nature or strength of the NC–ligand bond, or on the structure of the capping layer. In some cases, this lack of understanding may hinder the correct interpretation of experimental data.

A few attempts were undertaken to link experimental observations to microscopic properties of the NC capping. In Ref.,²²⁵ Aldana *et al.* correlated precipitation and re-dispersion of NCs with the thiol/thiolate equilibrium in aqueous solution. Using this information, the Gibbs free energies for binding of thiolates to Cd chalcogenide NCs with different size were estimated. Photoluminescence (PL) quenching of CdSe NCs by alkylthiols was related to surface coverage and used to estimate binding energies and capping exchange rates in Refs.^{221,223,226} However, the exact correspondence between coverage and PL is still under debate, and recent findings are in contrast to earlier used assumptions.^{54,227} In Ref.,²²² the increase of PL QY due to adsorption of alkylamines to washed CdSe NCs was used to estimate the binding energy. Complementary NMR measurements were employed in this study to verify the relation between coverage and PL.

Computational methods provide a powerful tool for studying ligand adsorption. *Ab initio* quantum chemical calculations have the potential to deliver the most accurate results; but they are limited to very small systems and do not account, typically, for thermal fluctuations. In Refs.,^{228,229} binding energies for capping molecules were computed for different surface sites of very small (CdSe)₁₅ and (CdSe)₃₃ NCs, while in another Density Functional Theory (DFT) study,²³⁰ adsorption of ligands to bulk CdSe crystal planes was investigated. The knowledge of binding details is crucial for understanding of the size and shape control during nanocrystal growth. However, NCs typically used in experiments have diameters $\approx 2\text{--}5$ nm, and thus $\approx 100\text{--}1600$ CdSe ion pairs and $\approx 40\text{--}250$ capping molecules. Classical molecular simulations are an excellent tool to efficiently compute properties at the atomistic level of systems of this size at finite temperatures, while DFT calculations would be computationally very expensive. For example, classical simulation studies of bare CdSe NCs have resolved the mechanism of surface relaxation²³¹ and of pressure induced phase transitions.^{127,128} CdSe NCs capped by trioctylphosphine oxide (TOPO) were considered by Rabani,²³² describing the surface packing and the total dipole moment of the capped NC. We are not aware of further classical molecular simulation studies of capped CdSe NCs.

In the present work, we use classical molecular simulations to study adsorption of ligands to CdSe NCs commonly used during and after synthesis: amines, thiols and thiolates, phosphine and phosphine oxide (PO). We would like to emphasize

that no additional force field parameter fitting and adjusting is used in this work, and none of the interaction models used here has been developed specifically for capped semiconductor NCs. Binding of surfactants is considered mainly as an effect of electrostatic interactions between atoms of ligand molecules and of a NC; and we compare the binding energies with quantum chemical and experimental data from literature. Our primary goal is to demonstrate that binding of most ligands can be accurately described in terms of relatively simple physical interactions. Next, following previous studies of adsorption of alkylthiols to gold NCs,^{159,233} we compute adsorption isotherms of hexylamine to CdSe NCs. The objective is to relate the number of adsorbed ligand molecules to their chemical potential or vapor pressure. This information is crucial for experimental studies of bare NCs since it is not possible to verify desorption of ligands under ultra-high vacuum (UHV) (10^{-12} – 10^{-9} kPa) directly.²³⁴ In previous studies, it was often assumed that one ligand binds to each surface Cd atom, and then saturation occurs.^{221–223,226,229} Our adsorption isotherms show that this is not the case; and comparing radial distribution functions and snapshots we describe the mechanism that allows adsorption of additional molecules at high loadings.

The remainder of this chapter is structured as follows. In Section 3.2, the model used in our simulations is described; Section 3.3 contains details of our simulation techniques and the NC preparation procedure. In Section 3.4 we present and discuss our calculated binding energies for single capping molecules of different types. Formation mechanism and structure of an amine capping layer is studied Section 3.5. In Section 3.6 we summarize our findings.

3.2 Interaction model

The philosophy of our approach is to avoid any fitting of interactions between NC and ligands. Instead, the existing atomistic force fields for *bulk* CdSe and *bulk* ligands are adopted, and the cross-interactions are derived from the conventional combining rules. In the force fields used here, bonded interactions and partial charges are derived from quantum chemical calculations, while remaining interactions are fitted to reproduce desired bulk properties. We apply the united atom model to alkyl tails of capping molecules: CH₂ and CH₃ groups are represented by single pseudo-atoms. Hydrogen atoms in SH and NH₂ groups are modeled as point charges, while all other atoms (Cd, Se, N, S, P, O) are simulated explicitly. The model used in this work does not account for polarization or charge transfer; it is not clear from literature, however, whether this is important for NC–ligand systems.²²⁸

All non-bonded atoms interact via the Lennard-Jones (LJ) and the Coulomb potentials

$$U_{ij}(r_{ij}) = \phi_{\text{LJ}} + \phi_{\text{Coulomb}} \quad (3.1)$$

Table 3.1: Partial charges of (pseudo)atoms in the model.

Atom	Charge	Source
C (at N)	0.18	TraPPE ²³⁵
C (at S)	0.171	TraPPE ²³⁶
C (at P)	-0.1	MM3, MM4 ^{96,237}
C other	0	TraPPE ^{97,235,236}
Cd	1.18	Ref. ²⁰³
H (at N)	0.356	TraPPE ²³⁵
H (at S)	0.206	TraPPE ²³⁶
N	-0.892	TraPPE ²³⁵
O	-0.77	MM3 ⁹⁶
P (TBP)	0.3	MM4 ²³⁷
P (TBPO)	1.07	MM3 ⁹⁶
S	-0.377	TraPPE ²³⁶
S ⁻	-1.171	TraPPE ^a
Se	-1.18	Ref. ²⁰³

^a The charge of S⁻ was defined by removing a proton from an SH group in the TraPPE force field.

with

$$\phi_{\text{LJ}} = 4\epsilon_{\text{LJ}} \left[\left(\frac{\sigma_{\text{LJ}}}{r_{ij}} \right)^{12} - \left(\frac{\sigma_{\text{LJ}}}{r_{ij}} \right)^6 \right] \quad (3.2)$$

and

$$\phi_{\text{Coulomb}} = \frac{1}{4\pi\epsilon_0} \frac{q_i q_j}{r_{ij}}, \quad (3.3)$$

where r_{ij} is the distance between beads i and j ; $\epsilon_{\text{LJ}}, \sigma_{\text{LJ}}$ are the Lennard-Jones parameters; ϵ_0 is the dielectric constant of vacuum; q_i, q_j are the partial charges on atoms i and j , respectively. In ligand molecules, we account for intramolecular bond stretching, bond bending and torsional forces. Additionally, segments that are separated by more than three bonds interact via intramolecular LJ and charged interactions. The LJ potential was truncated and shifted at 10 Å.

The parameters for Cd and Se are taken from Ref.²⁰³ They are derived such that the geometry and mechanical properties of bulk CdSe are reproduced accurately. Moreover, the computed transition pressure from wurtzite to rock-salt crystal structure agrees with experimental measurements. The TraPPE force field^{97,235,236} is used for thiols, amines and alkyl tails of TBP and TBPO molecules. This force field is known to accurately reproduce properties of (multi-component) liquids and vapors. Parameters for the phosphorus and oxygen containing headgroup of TBPO are taken from the MM3 force field⁹⁶ as in Ref.,²³²

the ones for TBP are taken from its successor (MM4 force field).²³⁷ These parameters were developed to reproduce the geometry of isolated molecules; we are not aware of any force field for phosphines or POs that was designed or tested for bulk compounds. LJ cross parameters are obtained using the Lorentz-Berthelot combining rules.¹⁴⁷ Charges of different (pseudo)atoms in the model are summarized in Table 3.1.

3.3 Methods

3.3.1 Molecular Dynamics simulations

In Molecular Dynamics (MD) simulations, the equations of motion were integrated using the velocity Verlet (VV) algorithm^{85,167} with the timestep of 2 fs. Velocities were rescaled to the desired temperature T during the equilibration time; afterwards T was kept constant using the Andersen thermostat.²³⁸

3.3.2 Monte Carlo simulations

To study the adsorption of capping molecules on a CdSe NC, we apply Configurational-bias Monte Carlo (CBMC) simulations in the grand-canonical ensemble.^{85,153} During the simulations, surfactant molecules are exchanged between the simulation box and a reservoir at an imposed chemical potential μ or, equivalently, fugacity f . The following MC trial moves are used to sample the degrees of freedom of the system: translations of molecules and individual NC atoms,¹⁵² molecular and pivot rotations,^{239,240} (partial) chain regrows and chain insertions/removals (grand-canonical MC). For linear parts of ligand molecules, we apply the conventional CBMC algorithm,^{85,153} while for branched fragments the coupled-decoupled CBMC method¹⁶¹ is used. Insertions and removals in the grand-canonical ensemble are performed using the biased insertion technique developed in Section 2.4.1 (see also Ref.¹⁵⁹). The grand-canonical simulations were between 80000 and 500000 MC cycles¹ long to ensure sufficient sampling. The first 10% of them suited equilibration.

3.3.3 Nanocrystal preparation

Quasi-spherical CdSe nanocrystals were prepared using the following procedure. First, a sphere with a given radius is cut out from the bulk CdSe wurtzite lattice. All atoms with one nearest neighbor (NNb) are removed.^{127,241} The structure is accepted only if the numbers of remaining Cd and Se atoms are equal. Varying the (initial) sphere radius and center, we were able to generate 16 different candidate structures ranging between (CdSe)₁₀₂ and (CdSe)₁₅₄₁, corresponding to

¹The number of trial moves in a MC cycle is (10 + the number of NC atoms + the number of capping molecules present in the system.)

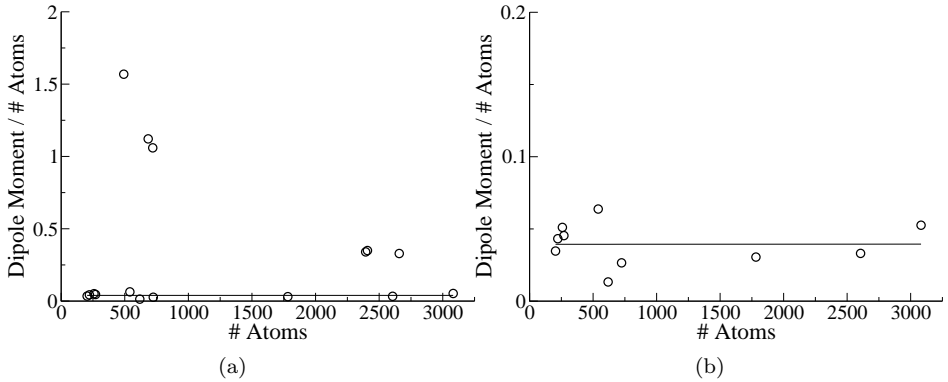


Figure 3.1: Dipole moment of annealed CdSe nanocrystals (NC) in atomic units divided by the number of atoms in the NC versus the number of atoms in the NC. (b) is a tenfold zoom of (a). The solid line is linear regression to the ten data points in the bottom part of the figure.

2.1–5.5 nm diameter. Next, we equilibrated the structures and allowed the surface to relax. The importance of this step was emphasized in the previous DFT and MD studies on CdSe NCs.^{228–232} For each structure, we carried out a 1 ns long MD simulation at 450 K; and we then cooled the structures down to 300 K in steps of 25 K, 0.1 ns each. During the equilibration procedure, we observed similar behaviour to what was reported in previous MD simulation studies on wurtzite nanocrystals.^{127,231,232} The electric dipole moment p_{NC} of the NC decreased significantly compared to the initial structure. The decrease of potential energy was less pronounced. While small NCs become elongated and faceted, larger ones appear to be almost spherical. As in Ref.,¹²⁷ during our simulations we monitored the coordination statistics: the fraction of atoms with a given number of NNbs.² Atoms with one or two NNbs are identified as surface defects; with three NNbs as interface atoms; with four NNbs as interior atoms; and with five or more atoms as lattice defects. The number of surface defects drastically reduced in all cases during our simulations. The fraction of threefold coordinated atoms increased while the fraction of fourfold coordinated atoms slightly decreased; both numbers strongly fluctuate during simulations. The reader is referred to Ref.²³¹ for a detailed description of the complex reconstruction of surface layers in NCs during relaxation. At the end of the equilibration, the potential energy, dipole moment and coordination numbers reached constant values (up to thermal fluctuations). This indicates that the surface has reached its equilibrium structure.

²Two atoms are defined as nearest neighbours if their distance is less than a certain radius R_{NNb} (we choose $R_{\text{NNb}} = 2.9 \text{ \AA}$). Note that the obtained coordination number depends on the value of R_{NNb} , but trends such as in Fig. 3.9(a) are not affected by the precise choice of R_{NNb} .

Finally, we plot $p_{\text{NC}}/N_{\text{NC}}$ versus N_{NC} , where N_{NC} is the total number of Cd and Se atoms in the NC. The dipole moment of CdSe nanostructures is expected to derive from the asymmetry of its wurtzite unit cell leading to a linear scaling with volume.^{242,243} However, the origin, magnitude and precise scaling with NC size of p_{NC} are still debated in experimental reports.^{242–245} A linear dependence of p_{NC} on N_{NC} has been shown in a MD study of equilibrated wurzite NCs,²³¹ and the ratio $p_{\text{NC}}/N_{\text{NC}}$ should therefore be constant. For the 16 generated structures, 10 satisfy the expected relation, while 6 non-systematically deviate from it having clearly larger dipole moments (see Fig. 3.1). This is most likely due to an unsuccessful relaxation, and we discard therefore these samples. Two further structures were discarded due to their unusually high potential energy.

We define the size of a nanocrystal as follows. The total number of atoms is divided by the number density of bulk CdSe to obtain the NC volume. The NC diameter is then defined as the diameter of a sphere with the same volume; and the NC surface area as that of this sphere.

3.4 Binding of ligands follows from electrostatic interactions

Binding energies of hexylamine (C6NH₂), hexylthiol (C6SH), hexylthiolate (C6S⁻), tributylphosphine (TBP) and tributylphosphine oxide (TBPO) ligands were computed using MD simulations of an isolated NC with one single ligand molecule in vacuum at $T = 300$ K. The binding energy U_B is defined as the sum of electrostatic and LJ interactions between the capping molecule and NC atoms. The positive sign of U_B corresponds to the energy gain of the system due to ligand adsorption. Since the main contribution to U_B in our simulations originates from electrostatic interactions, the obtained values should be divided by the relative dielectric constant ϵ_r of the medium to make comparison with experimental results. One should also keep in mind that in corresponding experiments reaction constants and, thus, free energies are derived.

The quasi-spherical stoichiometric equilibrated NCs were taken from the annealing procedure described in Section 3.3.3. The initial coordinates of the capping molecule are generated using CBMC. Once a surfactant is adsorbed to the NC surface in a MD simulation, it does not change binding site during typical simulation time. Some representative snapshots are shown in Fig. 3.2. Negatively charged atoms of the amine, thiol and PO headgroups adsorb to one surface Cd atom (also referred to as surface cation) without changing the surface structure significantly. By contrast, the sulphur atom in a thiolate headgroup binds to a pair of Cd atoms, and becomes part of the NC surface. This reconstruction is a result of the partial charge of S⁻, which is almost the same as of Se, c.f. Table 3.1.

For each NC, we performed 50 simulations with random initial coordinates of the capping molecule to resolve the binding energy at surface sites. Each simulation was 100 (200) ps long for C6NH₂/C6SH/C6S⁻ and TBP/TBPO, re-

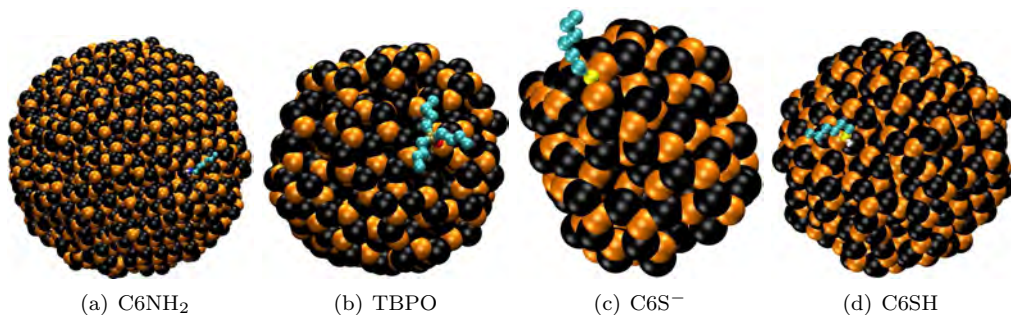


Figure 3.2: Snapshots of CdSe nanocrystals with one capping molecule adsorbed. (a) (CdSe)₁₅₄₁ with C6NH₂; (b) (CdSe)₂₇₀ with TBPO; (c) (CdSe)₁₀₂ with C6S⁻; (d) (CdSe)₃₆₂ with C6SH. The colour coding is: black - Se; orange - Cd; light blue - C; dark blue - N; white - H; yellow - S; brown - P; red - O.

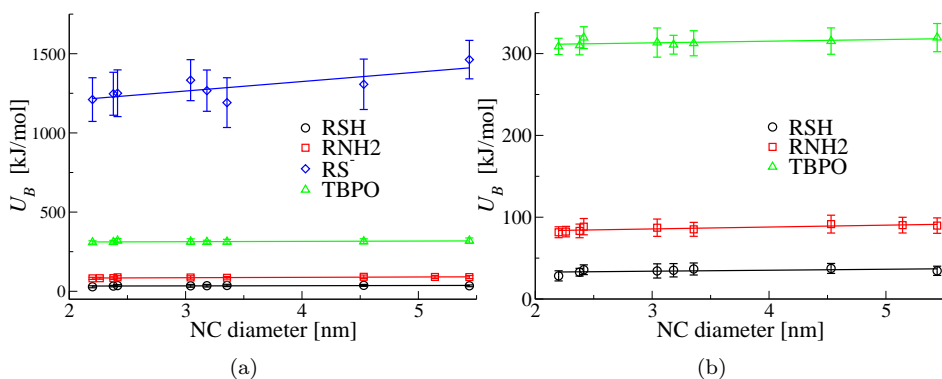


Figure 3.3: Computed binding energies for hexylamine, hexylthiol, hexylthiolate and TBPO to a CdSe nanocrystal (NC) as a function of the NC diameter. (b) is a fivefold zoom of (a). Error bars represent the distribution of binding energies at different binding sites.

Table 3.2: Average binding energies U_B and specificities S_B of different ligands on CdSe nanocrystals of different sizes.

Ligand	U_B [kJ/mol]	S_B [%]
C6NH ₂	86.8	7.5–12
C6SH	34.7	15–20
C6S ⁻	1283	7–12
TBPO	313.6	3–5

spectively; equilibration times were accordingly 20 (50) ps. Few simulations in which the ligand had not reached the NC surface were discarded. The remaining ones were used to collect statistics for each NC. It is important to note that differences between simulations originate from the differences in binding energy at various binding sites. We define the *binding specificity* S_B as the ratio between the standard deviation and the (average) binding energy. A low value of S_B means that the the corresponding ligand adsorbs equally likely to any site on a NC, while a large value of S_B corresponds to a ligand that prefers certain sites over the others. Hence, a ligand with low S_B can be used to synthesize spherical NCs, while the one with a high S_B could inhibit growth along a certain direction and, therefore, yield more specific shapes. The results are shown in Fig. 3.3, and the average binding energies and specificities are summarized in Table 3.2. We have verified that the main contribution to the binding energy originates from the electrostatic interactions with the surfactant headgroup; and the magnitude of U_B for different compounds increases, therefore, with the partial charge of their headgroups, c.f. Table 3.1. The binding energy increases with NC size for C6S⁻ and TBPO, and it remains approximately constant for C6SH and C6NH₂ ligands. The binding specificity S_B is between 7 and 12% for amine and thiolate; 15–20% for thiol; and 3–5% for TBPO. In all cases we found that S_B is independent of the NC size. The apparently high specificity of the thiol ligand is because the fluctuations in binding energy at different sites are, for this ligand, of the order of the thermal energy.

Puzder *et al.* obtained 0.91–1.05 eV (87.8–101.3 kJ/mol) from DFT calculations for trimethylamine on a (CdSe)₁₅ NC.²²⁸ Similar values (1.08–1.12 eV) have been reported in the DFT study of amines at a bulk CdSe surface.²³⁰ Kilina *et al.* obtained average binding energies of 0.67–0.69 eV (64.6–66.6 kJ/mol) for methylamine on (CdSe)₃₃ from DFT calculations.²²⁹ These values are in very good agreement with our results for C6NH₂. Ji *et al.* estimated Gibbs free energies of 9.8–11.0 kJ/mol for binding of octylamine to 3.5 nm CdSe NCs in pyridine from a combination of NMR and PL measurements;²²² while Bullen *et al.* obtained Gibbs free energies of 24.3 kJ/mol for binding of decylamine to 3.5 nm CdSe NCs using the same method, but with chloroform as solvent.²²⁶ Dividing our value by the relative dielectric constants of pyridine and chloroform at room temperature

($\epsilon_r \approx 12$ and 4.8, respectively), we obtain binding energies of 7.3 kJ/mol and 18.1 kJ/mol, respectively. The agreement with each of the two studies is within typical model accuracy. We conclude that the binding of amines to CdSe NCs can be understood as a result of electrostatic interactions between partially charged atoms.

The fact that our binding energy for TBPO is larger than the one for C6NH₂ is in qualitative agreement with Ref.,²²³ where TOPO was shown to bind stronger than amines. Interestingly, TBPO has a lower binding specificity than amine and thiolate ligands. Puzder *et al.* reported 0.63–1.37 eV (60.8–132.2 kJ/mol) from DFT calculations for trimethylphosphine oxide on a (CdSe)₃₃ NC,²²⁸ while Kilina *et al.* obtained 0.64–0.77 eV.²²⁹ The disagreement between these and our values for TBPO (313.6 kJ/mol) may indicate that partial charges on O and P atoms could be overestimated in the MM3 force field. Nevertheless, it is clear that binding of the PO headgroup to CdSe NCs can be fully explained by Coulombic interactions between partially charged atoms.

Aldana *et al.* correlated precipitation and re-dispersion of NCs to the thiol/thiolate equilibrium in aqueous solution.²²⁵ From this information, the Gibbs free energies for binding of thiolates to Cd chalcogenide NCs with different size were estimated. For CdSe, binding energies in the range of 23–35 kJ/mol were found. Correcting our results by the relative dielectric constant of water ($\epsilon_r \approx 80$) yields binding energies of 0.43 kJ/mol and 16.0 kJ/mol for C6SH and C6S⁻, respectively. Thus, the interaction between a thiol molecule and a CdSe NC in water is weaker than thermal energy, and thiols are expected to dissolve from the NC surface yielding precipitation of NCs. Our corrected value of U_B for C6S⁻ (16.0 kJ/mol) is of the same order of magnitude, but somewhat lower than the ones measured in experiment. The binding strength decreases with increasing NC size for all materials in Ref.²²⁵ (c.f. Fig. 3.4), which is in contrast with the slightly increasing U_B observed in the present work (c.f. Fig. 3.3). This difference in trend needs a separate explanation.

A covalent bond between a thiolate and a NC was suggested in Ref.²²⁵ It was then speculated that this bond becomes weaker with increasing NC size and vanishes in the bulk limit. However, this argument has been undermined by semiempirical calculations of the binding energy of thiol ligands to CdSe NCs with varying size.²⁴¹ The explanation suggested without proof in the latter paper is that U_B decreases due to changes in the distribution of facets. However, this would imply a systematic trend in binding specificity S_B with NC size, which we did not observe in our simulations. A possible explanation can be derived from the electrostatic model of the present work. In contrast to *charge neutral* NCs considered here, Aldana *et al.* study *positively charged* NC cores, such that their charge is compensated by the adsorbed thiolates. In this case, the electrostatic binding energy is expected to decrease with increasing NC size. Consider, namely, a small charged hard sphere touching a large oppositely charged hard sphere with equal charge, where in both cases the charge is spread homogeneously. Then, obviously, the interaction will weaken with increasing size of the large sphere due

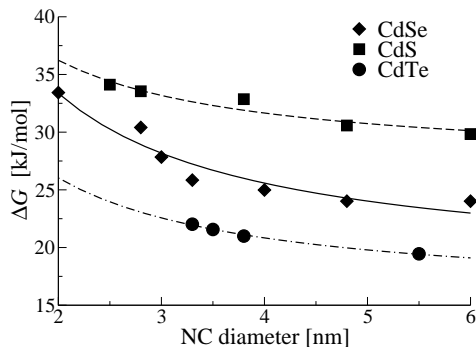


Figure 3.4: Gibbs free energies ΔG of binding of thiulates to CdSe, CdS and CdTe nanocrystals (symbols) and fits to Eq. (3.4) (lines). Data was taken from Ref.²²⁵

to the increasing separation between the centers of charge. The interaction energy U_B as a function of NC radius R would then scale as

$$U_B(R) = U_B^0 + C/R \quad (3.4)$$

with a size-independent binding energy U_B^0 and a constant C . Fig. 3.4 shows the two-parameter fit of the data from Ref.²²⁵ to Eq. (3.4). The deviations of data points from the curves lie within experimental error for all three curves corresponding to the three different NC types considered in that work. Interestingly, the value of U_B for a very large CdSe NC (i.e., U_B^0) of 18 kJ/mol is very close to our value corrected for ϵ_r (16 kJ/mol).

In several studies, PL quenching by thiols was used to obtain both qualitative and quantitative information on binding of different ligands.^{221,223,226} Addition of a small amount of thiol leads to significant reduction of PL yield, suggesting that thiol molecules bind to the NC surface replacing native ligands (amines, phosphines and their oxides). As mentioned earlier, the quantitative data from these papers may be not reliable due to the oversimplified modeling of quenching.^{54,227} We argue that the observed decrease of PL QY is instead affected by the thiol–thiolate equilibrium. In fact, both S^- and SH can act as PL quenchers. First, it has recently been shown using NMR that thiol surfactants displace native ligands only after deprotonation by an amine.⁵⁴ Second, individual CdSe NCs show non-uniform (blinking) behaviour upon thiol addition.²²⁷ This is in sharp contrast with the main assumptions of Refs.^{221,223,226} that quenching is uniform and depends continuously on the number of adsorbed thiols. Third, deprotonation of thiols by amines follows from simple considerations: alkylthiols are weak acids ($pK_a \approx 10$), while alkylamines are intermediate bases ($pK_b \approx 3.5$). Finally, the binding strength of a thiol ligand in apolar media ($\epsilon_r \approx 2.5$) is 13.5 kJ/mol according to the present work. This is sufficient for adsorption to the NC surface, but

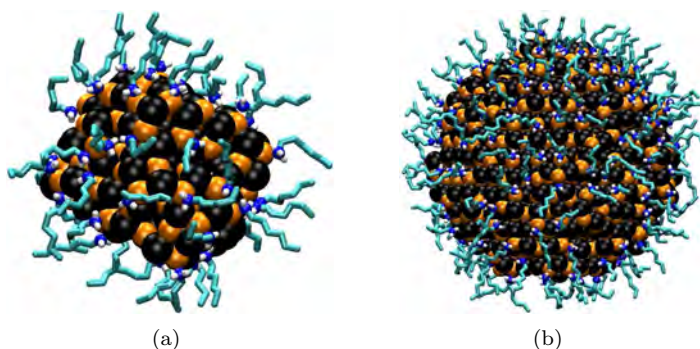


Figure 3.5: Typical simulation snapshots for (a) $(\text{CdSe})_{102}$ capped by 47 C_6NH_2 molecules and (b) $(\text{CdSe})_{891}$ capped by 187 C_6NH_2 molecules, both at $T = 300$ K. The colour coding is same as in Fig. 3.2.

not sufficient to replace the native ligands if no thiolate is formed. Furthermore, there is some indirect evidence for thiol dissociation during ligand exchange. In Ref.,²²¹ e.g., PL quenching due to addition of thiols is much stronger in systems with amines. In Ref.,²²³ it has been observed that additional amines accelerate adsorption of thiols. In view of the above arguments, it is crucial to account for the thiol–thiolate equilibrium when considering ligand exchange by thiols.

The binding energy of TBP is of order of thermal fluctuations (not shown), which is in sharp contrast with the recently reported value of 3 eV (289.5 kJ/mol).²³⁰ This shows that the interaction between phosphine surfactants and CdSe goes beyond the model presented in Section 3.2.

3.5 Adsorption of alkylamines in two steps

After having investigated the binding of single capping molecules, we proceed by studying the properties of an amine capping layer. By imposing varying ligand fugacities in grand-canonical MC simulations, we determined the adsorption isotherms of C_6NH_2 for isolated CdSe NCs at different temperatures. In these simulations, we calculate the average number of (adsorbed) capping molecules at a given fugacity (or, equivalently, chemical potential). We computed the isotherms on $(\text{CdSe})_{102}$, $(\text{CdSe})_{111}$ at different temperatures; and on $(\text{CdSe})_{891}$ at $T = 300$ K. For a convenient comparison, we express *loading* as the number of adsorbed molecules divided by the surface area of a sphere with the same volume as the NC.

Typical simulation snapshots at high loading are shown in Fig. 3.5. Amine surfactants adsorb to Cd atoms on the surface, and alkyl tails point outwards. The capping layer on the larger NC $(\text{CdSe})_{891}$ is denser due to the smaller sur-

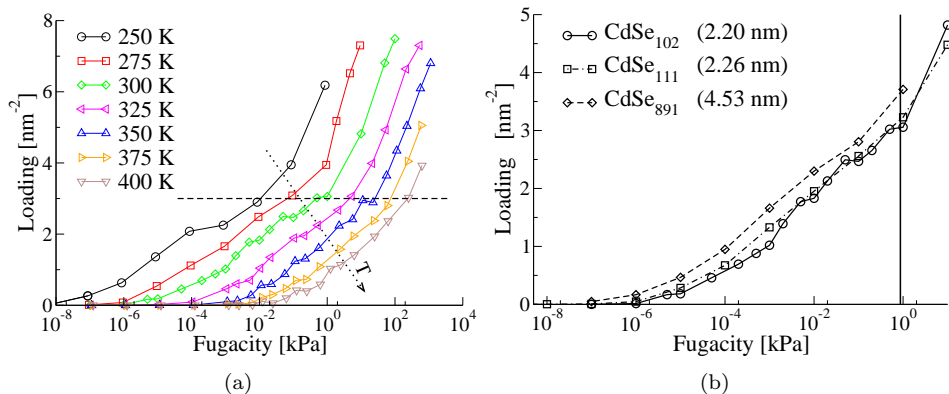


Figure 3.6: (a) Adsorption isotherms of C6NH₂ on (CdSe)₁₀₂ at different temperatures. (b) Adsorption isotherms of C6NH₂ on CdSe₁₀₂, CdSe₁₁₁ and CdSe₈₉₁ (2.20, 2.26 and 4.53 nm diameter, respectively) at $T = 300$ K; the isotherms are shown only for low loadings. The vertical line represents the saturated vapor pressure of hexylamine (0.87 kPa at 293.15 K).²⁴⁶ Lines serve as guide to the eye. The loading is defined as the number of adsorbed molecules divided by the surface area of a sphere with the corresponding diameter.

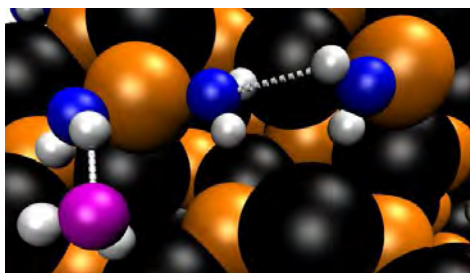


Figure 3.7: Fragment of a nanocrystal surface capped by amine ligands at high loading. Carbon chains are not shown for clarity. Black spheres represent Se atoms; orange – Cd; blue – N; white - H; the magenta sphere represents a nitrogen atom that is not adsorbed to a Cd surface site. White dotted lines represent (hypothetic) hydrogen bonds between amine headgroups. The two amine groups in the middle and top left are adsorbed to the same Cd atom.

face curvature. The calculated adsorption isotherms are shown in Fig. 3.6. As expected, the number of adsorbed ligands increases with increasing fugacity and decreasing temperature. The onset of the isotherm shifts to higher fugacities at higher temperatures: from 10^{-8} kPa at 250 K to 5×10^{-5} kPa at 450 K in Fig. 3.6(a). Note that in this regime fugacity is approximately equal to the partial pressure of the vapor. Thus, amine ligands are expected to desorb from the NC surface under UHV at moderate temperatures. As we can see in Fig. 3.6(b), the isotherms for the three different NCs considered here lie very close together. Therefore, the features discussed in the sequel are general and do not result from some particular surface properties of an individual NC.

The isotherms in Fig. 3.6(a) do not reach saturation despite high loadings.³ Recall from the previous section that a single amine molecule adsorbs with the negatively charged N atom to a surface Cd atom (*direct adsorption*), and one would therefore expect a maximum loading corresponding to the number of surface cations, which can be estimated as $3\text{--}4 \text{ nm}^{-2}$ from the coordination histograms of NCs. Instead, the isotherms in Fig. 3.6(a) become steeper at loadings around 3 nm^{-2} (shown as dashed line), and increase rapidly to much higher loadings. Notably, some isotherms in Fig. 3.6(a) reach the loading of 7 molecules per nm^2 corresponding to 106 adsorbed ligands on $(\text{CdSe})_{102}$, which is even more than the total number Cd atoms present. This clearly shows the existence of a binding mechanism that allows loadings beyond the limit of direct adsorption. We will show that this second mechanism (*indirect adsorption*) combines two effects: a second amine binds to an already occupied Cd surface site; and adsorption to even less favourable positions under formation of hydrogen bonds (HB) with other amines and surface Se atoms. A snapshot in Fig. 3.7 visualizes this motif. Consider the two amines that are adsorbed to a Cd atom on the left. The amine in the bottom left shown in magenta is not bound to any Cd atom; both its H atoms interact with Se surface atoms and the N atom forms an HB. We see that the two amine groups in the middle and on the right also form an HB.

To obtain additional direct evidence for the nature of indirect adsorption, we compare the radial distribution function $g(r)$ between N atoms of ligand headgroups at different loadings in Figs. 3.8(a) and 3.8(b). The peak of $g(r)$ close to 5 \AA is dominant in all cases. This value is, coincidentally, very close to the spacing between thiol headgroups in a self-assembled monolayer of alkylthiols on gold (111);¹⁷² however, the origin is different. The exact position of this peak is 4.95 \AA on $(\text{CdSe})_{102}$ and 4.65 \AA on the larger $(\text{CdSe})_{891}$. We relate these positions to the next-nearest neighbor distance in the CdSe wurtzite lattice (4.4 \AA) using a geometric model presented in Fig. 3.8(c). Consider a sphere with the same radius

³It is not possible to reach the actual saturation point in our simulations, because at high fugacities the simulation box will be completely filled with a liquid phase formed by capping molecules. We verified that this “condensation” never occurred in the reported simulations. From Fig. 3.6(b) we see that higher loadings ($> 3.5 \text{ molecules/nm}^{-2}$) only occur at fugacities higher than the saturated vapor pressure of C_6NH_2 , so that the vapour phase surrounding the NC is metastable in this range.

R as the NC, and two ligand headgroups adsorbed to two surface atoms with distance $R_1 = 4.4 \text{ \AA}$. Assume the distance R_2 between the two headgroups to be the same as the $g(r)$ peak position, and their separation from the NC surface is equal d . The distance d follows from the relation $\frac{R_2}{R_1} = \frac{R+d}{R}$. We obtain $d = 2.7 \text{ \AA}$ for $(\text{CdSe})_{102}$ and $d = 2.6 \text{ \AA}$ for $(\text{CdSe})_{891}$. This is, in fact, the typical Cd–N binding distance in our simulations. Therefore, we ascribe the main peak in Figs. 3.8(a) and 3.8(b) to direct adsorption.

At higher loadings, the first peak of the $g(r)$ between N atoms emerges at $r \approx 3 - 3.5 \text{ \AA}$. For $(\text{CdSe})_{102}$, this peak moves from 3.7 to 3.3 \AA at increasing loading (Fig. 3.8(a)); while for $(\text{CdSe})_{891}$ it remains at 3.7 \AA , and a shoulder forms at 3.2 \AA (Fig. 3.8(b)). We assign this peak to indirect adsorption since its position cannot be explained by the spacing between adjacent surface cations. Consider the first three peaks of the $g(r)$ between N and H atoms of different amine headgroups, which is shown in Fig. 3.8(d). The first peak at 2.3 \AA is not present at low loadings and increases with the number of adsorbed ligands. This peak is a fingerprint of the amine–amine HB, since we do not account for HB as a special interaction type in our model. The following peaks are broader. The second one (3.5–4 \AA) correlates with the first peak of the $g(r)$ between N atoms (Figs. 3.8(a) and 3.8(b)). It can be attributed to a pair of amine headgroups that are adsorbed to the same Cd atom: despite the close distance they cannot form an HB due to steric hindrance. The third peak at 5.5–6 \AA corresponds to amines bound to adjacent surface Cd atoms (direct adsorption) as discussed above.

The transition from direct to indirect adsorption occurs at realistic conditions (temperatures, fugacities); and it may be the reason for some observations reported earlier. We focus on two recent experimental observations. (1) Addition of a small amount of amines to a dispersion of bare CdSe NCs increases their PL QY,^{220–222} but this effect eventually reverses when more amines are added.^{220,221} (2) Increasing the temperature of a dispersion of amine-capped CdSe NCs leads to PL anti-quenching.¹⁹⁰ This optical transition occurs gradually within a range of 35 K. To the best of our knowledge, these phenomena are still lacking a microscopic explanation. Even though we are unable to directly establish a relation between adsorption and optical phenomena, our results enable us to speculate about the following explanation. Assume that direct adsorption of amines increases the PL QY of CdSe NCs, while indirectly adsorbed amines act as quenchers. With increasing concentration (and, hence, loading) we would then expect an increase of QY until the indirect adsorption starts. This may explain the experimentally observed PL QY increase upon addition of amines to washed NCs.^{220,221} As we can deduce from Fig. 3.6(a), the indirectly adsorbed amines gradually leave the surface at increasing temperature and constant concentration. This may also explain the change of optical properties reported in Ref.¹⁹⁰

We have analyzed the coordination of NC atoms as function of the number of adsorbed ligands. Recall that the number of surface defects (atoms with two NNbs) decreases during the relaxation in vacuum, while the number of interface

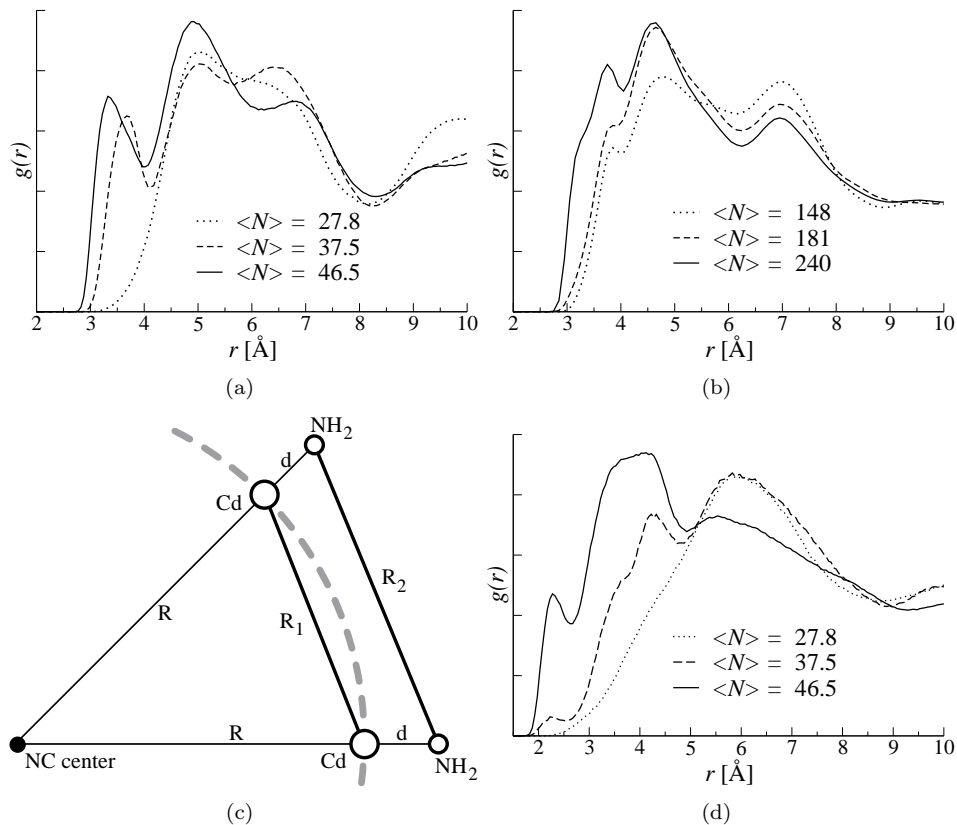


Figure 3.8: (a, b) Radial distribution function $g(r)$ between nitrogen atoms of C6NH₂ ligands adsorbed to (CdSe)₁₀₂ (a) and (CdSe)₈₉₁ (b), respectively. The three curves in each graph correspond to average numbers $\langle N \rangle$ of adsorbed capping molecules. (c) Geometric model for the main peak in (a, b). The dashed grey arc represents a spherical NC surface with radius R . Two adjacent Cd atoms have distance R_1 . To each of these atoms, an amine is adsorbed at Cd–N distance d ; the distance between them is R_2 . (d) Radial distribution function $g(r)$ between N and H atoms on different C6NH₂ capping molecules adsorbed to (CdSe)₁₀₂.

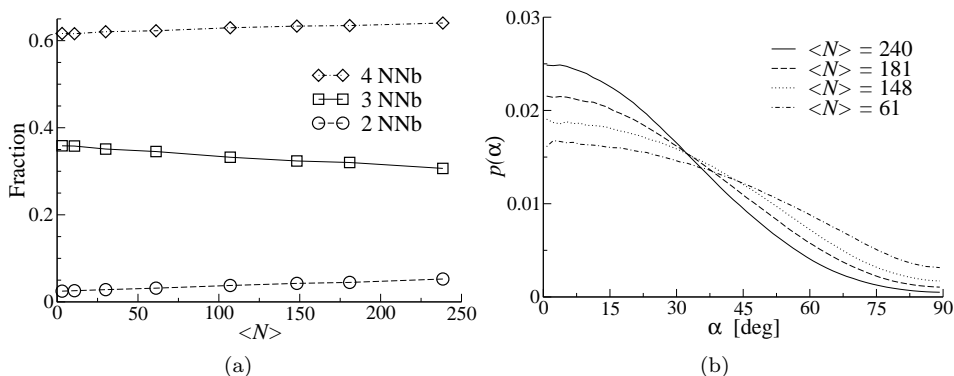


Figure 3.9: (a) Fraction of NC atoms with 2,3 and 4 nearest neighbors (NNb) in a $(\text{CdSe})_{891}$ NC as a function of the (average) number $\langle N \rangle$ of adsorbed C_6NH_2 molecules. (b) Orientational order parameter $p(\alpha)$ at four different C_6NH_2 loadings on a $(\text{CdSe})_{891}$ NC.

atoms (three NNbs) increases and the number of interior atoms (4 NNbs) decreases. Adsorption of surfactants has the opposite effect as we can see from Fig. 3.9(a). The number of surface defects increases proportionally to the number of adsorbed amine molecules; the fraction of interior atoms increases too (from 0.61 to 0.65 in Fig. 3.9(a)); and the number of interface atoms decreases, accordingly. While the relaxation of the outermost layer has been reported previously,²³⁰ this is to the best of our knowledge the first observation of the ligand-induced reconstruction of deeper layers. The increase of surface defects can be rationalized by the indirect adsorption: if two capping molecules adsorb to the same Cd atom, then it has at most two NNbs in the NC. However, the simultaneous increase of the number of interior atoms is highly non-trivial. This suggests that, (i) the NC relaxes back to the initial crystal structure under continuous interface thinning; and (ii) this occurs at room temperature.

The structure of the capping layer at different loadings can be described by the orientational order parameter $p(\alpha)$. Consider the angle α between the head-to-tail vector of a surfactant molecule and the surface normal. Small values of α correspond to ligands standing almost perpendicular to the surface, while value close to 90° describe ligands lying parallel to the surface. We define $p(\alpha)$ as the probability distribution of α divided by $\sin \alpha$, so that $p(\alpha)$ is constant for a random orientation. In Fig. 3.9(b), $p(\alpha)$ is plotted for four different loadings on $(\text{CdSe})_{891}$ at $T = 300$ K. This graph is representative for all systems considered in this work at all temperatures. With increasing loading, orientation of alkylamine ligands smoothly changes from more random to upright. We previously observed the same behaviour for alkylthiols adsorbed on Au NC, see Section 2.6.2 and Ref.¹⁵⁹

This indicates that the structure of a capping layer formed by linear surfactants depends primarily on the loading, and not on the precise details of the NC–ligand interaction.

3.6 Conclusions

Adsorption of different ligands (amine, thiol, thiolate, phosphine and phosphine oxide) to CdSe nanocrystals was studied using Molecular Dynamics and Monte Carlo simulations. Our interaction model was assembled from existing classical force fields for bulk materials, and we do not apply additional fitting of parameters. The binding energy of amines (86.8 kJ/mol) and phosphine oxides (313.6 kJ/mol) follows quantitatively from electrostatic interactions between partial charges on ligand molecules and anions and cations in the semiconductor core. This has an important consequence: the binding strength strongly depends on the relative dielectric constant of the medium. The binding energy of thiols can be explained in the same terms assuming that thiol ligands dissociate (33.8 and 1332 kJ/mol for an intact and dissociated thiol, respectively). Our binding energies of amine and thiolate are in good agreement with quantum chemical calculations and experimental measurements which do not rely on thiol-induced luminescence quenching. TBPO has the lowest binding specificity among the considered ligands.

Calculated adsorption isotherms of hexylamine suggest that amine molecules desorb from CdSe NCs under ultra-high vacuum. This process is facilitated by increasing the temperature. Comparing adsorption isotherms, simulation snapshots and radial distribution functions we conclude that the amine capping layer forms in two steps. At low loadings, amine headgroups bind directly to Cd atoms at the surface. At higher loadings, amines bind to already occupied Cd atoms and to less favourable Se sites. This indirect adsorption is supported by hydrogen bonds between amine headgroups. This mechanism can occur at ambient conditions, and may be the reason for earlier observed temperature or concentration induced changes in optical properties of NCs. Upon increasing surfactant coverage, the structure of the NC changes gradually toward the one of the bulk material: the crystalline interior becomes larger, the interface layer becomes thinner, and the number of (passivated) surface defects increases. This reconstruction of the interface occurs at ambient conditions.

Chapter 4

Interactions between Capped Nanocrystals

In this chapter, effective interactions between gold nanocrystals protected by capping molecules are studied using molecular simulations. We computed the potential of mean force for pairs and triplets of NCs of different size (1.8–3.7 nm) with varying ligand length (ethanethiol–dodecanethiol) in vacuum. Pair interactions are strongly attractive due to attractive van der Waals interactions between ligand molecules. Surprisingly, the equilibrium distance in vacuum always equals ca. 1.25 times the core diameter. Three-body interaction results in an energy penalty when the capping layers overlap pairwise. This effect contributes up to 20% to the total energy for short ligands. For longer ligands, the three-body effects are so large that formation of NC chains becomes energetically more favourable than close-packing of capped NCs at low concentrations, in line with experimental observations. To explain the equilibrium distance for two or more NCs, the Overlap Cone Model is introduced. This model is based on relatively simple ligand packing arguments. In particular, it can correctly explain why the equilibrium distance for a pair of capped NCs is always ≈ 1.25 times the core diameter independently on the ligand length. We make predictions for which ligands capped NCs self-assemble into highly stable 3D structures, and for which they form high-quality monolayers. We also show that incomplete capping layers promote sintering of NC cores, and that the presence of a good solvent results in purely repulsive interactions.

4.1 Introduction

Gold- and semiconductor nanocrystals (NCs) with specific size- and shape dependent optical and electrical behaviour are of growing importance in the fields of optics, electronics, catalysis, magnetic storage and biophysics.²⁴⁷ These NCs can self-assemble in a range of different 2D and 3D superstructures.^{49,62,63,65} NCs are

usually protected by an organic capping layer that prevents aggregation, *e.g.* gold NCs are often capped with alkylthiol molecules.³⁸ These capping molecules (also referred to as surfactants or ligands) play an important role in the self-assembly of NCs. The ratio between the core diameter (d_c) and surfactant chain length (L) determines the crystal structure of a Au NC superlattice.^{65,132} Capping exchange can alter the crystal structure of a binary superlattice.⁶⁸ Moreover, due to the attractive interactions between capping molecules, in binary NC systems crystal structures with high coordination form rather than the ones with a higher packing fraction.⁷⁰ The attraction between capped NCs is very strong; for example, a monolayer of Au NCs can form a self-supported membrane when dropcasted on a substrate with a hole up to 2 μm large.³² It is well-known that this attraction is at least one order of magnitude larger than the van der Waals (vdW) attractions between Au NC cores.^{32,130,133}

For the understanding of thermodynamic and kinetic properties of NCs, knowledge of the free energy or, equivalently, the potential of mean force (PMF) as a function of an appropriate order parameter is of vital importance.^{90,150} This would allow fabrication of novel materials and devices with tailor-made structural, mechanical and thermodynamic properties. The objective of this work is to study the effective interactions between capped NCs. Molecular simulation techniques provide an excellent tool for the computation of these, especially for nanoscale systems, as these techniques do not suffer from experimental limitations or from oversimplifications sometimes present in theories.⁸⁵ The computed PMFs for NCs in vacuum are useful for several purposes. First, they provide direct insight in the mechanical and thermodynamic stability of different self-assembled structures. Second, these effective interactions can be used to model mechanical properties of NC superstructures. Third, the PMF in vacuum can be used to describe capped NCs at the air-water interface, as NCs capped by hydrophobic ligands are hardly immersed in water at the surface.

Capped gold nanocrystals are a convenient system for molecular simulation studies. The binding of thiol headgroups to Au surfaces is better understood than for other NC-surfactant systems, as we can see from the previous two chapters. Several models have been successfully applied to describe the structure and thermodynamics of alkylthiol monolayers on flat Au(111)-surfaces^{159,192,233} and Au-NCs.^{131,137,159,233} It is important to note that the effective NC-NC interactions in a solvent are very different from the ones in vacuum due to solvent-capping layer interactions.¹²² The work of Patel *et al.*¹³⁹ focused on the PMF for very small capped NC cores (Au₃₈) for varying solvent quality, and it was found that the PMF can be tuned from strongly attractive to fully repulsive. Tay *et al.*¹³³ computed the PMF for only two selected systems in vacuum so that no definitive conclusions could be drawn concerning the general behaviour of the PMF. It is also not known whether thermodynamic properties of assemblies of capped NC can be described by pure pair interactions or whether many-body effects are important.

The aim of the present work is to systematically investigate the influence of

surfactant length, NC size, temperature and the completeness of the capping layer on the PMF. To the best of our knowledge, this is the first systematic study of these crucial parameters. We also quantify three-body effects, and discuss their importance for different systems. Based on the computed PMFs, we develop a coarse-grained NC–NC interaction potential. The Overlap Cone Model model is developed that explains our findings based on ligand packing arguments. We briefly address the efficiency of different computational methods to compute the PMF, and we compute the PMF for one system with a realistic explicit solvent (n-hexane).

4.2 Model and methods

In all simulations, the same united atom model is used for SH, CH₂ and CH₃ as in Section 2.2. Alkylthiols are labeled as “SC n ”, where n is the number of alkyl chain segments in the linear tail. Beads of different solvent and surfactant molecules interact with each other and with gold atoms via truncated and shifted Lennard-Jones (LJ) pair interactions. All LJ parameters are summarized in Table 2.1; note that the Au–S interaction is much stronger than other non-bonded interactions. We account for intramolecular bond stretching, bond bending and torsional interactions.⁹⁸ Additionally, we apply intramolecular LJ interaction between segments that are separated by more than three bonds.

The NC cores are modeled as rigid, close-packed icosahedra exposing only (111)-facets.¹²⁵ The maximal extent r_{\max} is defined as the center-to-corner distance, and the core diameter d_c is defined as twice the radius of gyration. Gold NCs are assumed to interact with each other via the Hamaker potential⁸⁸

$$U_{\text{Ham}}(r) = -\frac{A_{\text{Ham}}}{12} \left[\frac{d_c^2}{r^2 - d_c^2} + \frac{d_c^2}{r^2} + 2 \ln \left(1 - \frac{d_c^2}{r^2} \right) \right]. \quad (4.1)$$

The interaction constant A_{Ham} is 2 eV for gold in an apolar hydrocarbon medium.²⁴⁸

In all simulations periodic boundary conditions are imposed. The simulation box is chosen sufficiently large, so that capping layers of NCs do not interact with their periodic images. Unless stated differently, simulations are performed at constant temperature $T = 300$ K. An overview of all simulations including their length is given in Table 4.1.

4.2.1 Potential of mean force

Our aim is to determine the free energy, or, equivalently, the potential of mean force (PMF) as a function of nanocrystal–nanocrystal separation. Three methods for the PMF calculations are tested, and we use the most convenient one for each system. Two of them are constraint methods: one based on Monte Carlo (MC) and the other on Molecular Dynamics (MD). In both methods, the forces acting on the NC centers of mass are sampled. The third method involves averaging

System	Figure	Method	Length
Au ₁₄₇ (SC4) ₅₈	4.3, 4.4(a)	MD	5
Au ₁₄₇ (SC4) ₄₉	4.9	MD	5
Au ₁₄₇ (SC4) ₅₈ (hexane)	4.20(a)	MD	3
Au ₁₄₇ (SC8) ₅₈	4.4(a), 4.8(b)	MC	150000 (300000)
Au ₁₄₇ (SC8) ₅₈ ($T = 250$ K)	4.8(b)	MD	4 (14)
Au ₁₄₇ (SC8) ₅₈ ($T = 350$ K)	4.8(b)	MD	1 (3)
Au ₁₄₇ (SC8) ₅₈ ($T = 400$ K)	4.8(b)	MD	1 (3)
Au ₁₄₇ (SC12) ₅₈	4.4(a)	MD	10
Au ₅₆₁ (SC4) ₁₃₆	4.4(b)	MD	1 (3)
Au ₅₆₁ (SC4) ₁₁₄	4.9	MC	150000 (300000)
Au ₅₆₁ (SC4) ₁₃₆ ($T = 250$ K)	4.8(a)	MD	1 (3)
Au ₅₆₁ (SC4) ₁₃₆ ($T = 350$ K)	4.8(a)	MD	1 (3)
Au ₅₆₁ (SC8) ₁₃₆	4.4(b)	MC	150000 (300000)
Au ₅₆₁ (SC12) ₁₃₆	4.4(b)	MD	1 (3)
Au ₅₆₁ (SC4) ₁₃₆ - Au ₁₄₇ (SC4) ₅₈	4.5(b)	MC	100000 (500000)
Au ₅₆₁ (SC8) ₁₃₆ - Au ₁₄₇ (SC8) ₅₈	4.5(b)	MC	100000 (500000)
Au ₁₄₁₅ (SC2) ₂₄₂	4.5(a)	MD	1
Au ₁₄₁₅ (SC3) ₂₄₂	4.5(a)	MD	1
Au ₁₄₁₅ (SC6) ₂₄₂	4.5(a)	MD	1 (3)
Au ₁₄₁₅ (SC12) ₂₄₂	4.5(a)	MD	1
Au ₁₄₇ (SC4) ₅₈ 3-body	4.14(a), 4.14(c)	MC	150000 (500000)
Au ₁₄₇ (SC8) ₅₈ 3-body	4.14(b), 4.14(c)	MC	500000 (2000000)

Table 4.1: Overview of PMF calculations in this work. Simulation length is expressed in time [ns] for MD and the number of cycles for MC simulations, respectively. Numbers in brackets denote simulation lengths for close NC-NC separations where capping layers strongly overlap. A MC cycle consists of $N + 10$ steps, where N is the total number of (capping) molecules in the system. Unless stated differently, $T = 300$ K.

of non-reversible work performed during MD trajectories. The PMF can also be computed from unconstrained equilibrium MD/MC simulations such as umbrella sampling with multiple-histogram reweighting. See, e.g., Refs.^{249–251} for recent examples.

Consider two NCs at the fixed distance r . The mean force F_{mean} is defined as the average force between the two particles in direction of their connecting line:^{252,253}

$$F_{\text{mean}}(r) = \frac{1}{2} \left\langle \left(\vec{F}_2 - \vec{F}_1 \right) \cdot \vec{r}_u \right\rangle_{\text{NVT}} \quad (4.2)$$

where \vec{F}_1 and \vec{F}_2 are the total forces acting on the first and second NC core, respectively; $\vec{r}_u = \vec{r}/r$ is the unit vector connecting the two NCs, and angular brackets denote ensemble averages in the canonical ensemble. The potential of mean force is defined as

$$\phi_{\text{MF}}(r) = \int_r^\infty F_{\text{mean}}(s) ds. \quad (4.3)$$

The Helmholtz free energy $\mathcal{F}(r)$ is related to the PMF $\phi_{\text{MF}}(r)$ via¹⁵⁰

$$\mathcal{F}(r) = \phi_{\text{MF}}(r) - (d-1)k_B T \ln r + \text{constant}, \quad (4.4)$$

where d represents the dimensionality.

The mean force can be computed according to Eq. (4.2) using either constraint MC or MD simulations in the canonical ensemble¹. Eq. (4.3) is then used to calculate the PMF.

Monte Carlo simulations

The degrees of freedom of solvent and surfactant molecules are sampled using displacement,¹⁵² rotation²³⁹ and Configurational-bias Monte Carlo (CBMC) trial moves.^{153–156} The rotational degrees of freedom of the individual NCs are sampled using rotations of the NC or of the cluster defined as the NC with ligands adsorbed on its surface. The centers of mass of the NCs remain fixed during the simulation.

(Constraint) Molecular Dynamics simulations

The MD simulations are performed using the velocity Verlet (VV) algorithm.^{85,167} The only constraint on the system was applied to the NC–NC center of mass separation using the RATTLE algorithm,¹⁶⁹ the VV version of SHAKE.¹⁶⁸ Hereby, the NCs are “bonded” with a fixed length. The NC–NC bond can translate and rotate freely. The rotation of rigid NCs about their centers of mass is realized using quaternion rigid body dynamics.¹⁷⁰ The temperature is controlled using the Andersen thermostat.²³⁸

¹One can sample either forces acting on the NC cores or on the clusters defined as the NC and its capping layer. It is easy to show that both methods yield rigorously identical values for the mean force F_{mean} . The latter method yields faster convergence, especially at larger separations.

One may think that the rotational degrees of freedom of NCs are not sampled sufficiently in a constraint simulation at close distances, where the capping molecules on the two NCs interpenetrate. Indeed, in such a system a NC core is very unlikely to perform even one full rotation during typical simulation time. The computed F_{mean} may therefore depend on the initial configuration of the NC pair. To assess this issue, we performed a series of 10 simulations, where we (1) randomly rotated two capped NCs at a large distance; (2) pushed them together to a distance at which the capping layers significantly overlap; (3) equilibrated the systems using MC without NC rotations; and (4) computed the F_{mean} for each system with NC rotations. The results for all the ten systems are identical within error bars. We conclude that the limited sampling of NCs rotations does not influence the computed mean force.

Steered Molecular Dynamics simulations

Steered Molecular Dynamics (SMD) exploits Jarzynski’s equality^{254,255} that relates the equilibrium free energy difference $\Delta\mathcal{F}$ with the average irreversible work \mathcal{W} in a non-equilibrium system. In our case, a harmonic spring force with force constant k and equilibrium distance r_{SMD} acts in the direction of the line connecting the two NCs; r_{SMD} changes with constant velocity v . One can choose whether to pull the NCs apart ($v > 0$) or to push them together ($v < 0$). The free energy is then given by

$$\exp[-\Delta\mathcal{F}/k_B T] = \langle \exp[-\mathcal{W}/k_B T] \rangle, \quad (4.5)$$

where k_B is the Boltzmann constant and angular brackets denote an average over many non-equilibrium simulations that all start from different initial configurations sampled in the NVT-ensemble. A similar methodology has already been applied for determining the PMF between the starting and the end segment of an α -helix that was stretched as a function of time.^{256,257} For optimization purposes, one needs to tune k , v , and the number of simulations over which to average. This may be considered as a drawback of the method.

4.2.2 Sample preparation

The initial configurations for simulations in vacuum are prepared by a procedure similar to the one proposed in Ref.¹³¹ First, we generate a configuration with maximum surfactant coverage by a grand-canonical simulation of ethanethiol (SC2) on a pair of NCs. The Monte Carlo procedure described in Chapter 2 is used. Next, we perform simulations in the canonical ensemble at temperatures between 250 and 450 K. Such extensive equilibration is important due to the very slow diffusion of ligand headgroups on the NC surface. Finally, we exchange the SC2 ligand by the desired one using simulations in the semigrand ensemble,¹⁶⁶ and equilibrate further to allow for relaxation of alkyl tails. A typical snapshot of an equilibrated configuration is shown in Fig. 4.1. The headgroups are adsorbed to the surface

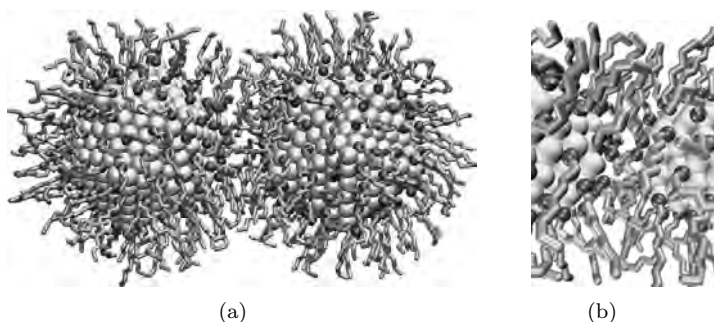


Figure 4.1: (a) A pair of Au_{561} nanocrystals at $r = 34 \text{ \AA}$ capped by 136 SC8 surfactant molecules each. Light grey spheres represent gold atoms; black spheres represent thiols headgroups; and grey lines represent alkyl tails. (b) Close-up of the “bottleneck” between NC surfaces. Note that the thiol capping molecules readily bend away from this bottleneck.

via the strong Au–S interaction. The hydrocarbon tails form a soft corona. We find that the maximum coverage on Au_{147} ($d_c = 1.8 \text{ nm}$), Au_{561} ($d_c = 2.7 \text{ nm}$) and Au_{1415} ($d_c = 3.7 \text{ nm}$) is 58, 136 and 242 alkythiol molecules, respectively, in good agreement with experiments.⁴⁷ This corresponds to one thiol headgroup per 1.6 surface Au atoms in the first case, 1.9 in the second case, and 2.0 in the third case. Compared to the value measured for an extended Au(111)–surface (one thiol headgroup per three surface atoms¹⁷¹), the packing of thiol headgroups on a NC is much denser due to the reduced steric repulsion of aliphatic tails.

4.2.3 Comparison of methods

We compared different methods for computing the PMF. We also tested a coarse-grained interaction potential between NCs and united atoms for MC.²⁵⁸ The computed PMFs are shown Fig. 4.2. All computations were performed on Intel Pentium 4 3.2 GHz desktop computers. Total computational times were 791 h for SMD (100 trajectories of 2.3 ns each); 125 h for constraint MD (60 separations of 1 ns each); 107 h for constraint MC (60 separations of 50000 cycles each); and 90 h would be required for same method with the same number of separations when using the coarse-grained potential of Ref.²⁵⁸ (Section 2.3 of the present thesis).

Constraint MD and MC have similar computational efficiency (*i.e.* accuracy vs CPU time) for simulations in vacuum, while SMD is a factor six slower. This is in line with a recent comparison of different techniques for PMF calculation, where constraint MD was found to be the method of choice.²⁵⁹ Furthermore, constraint methods allow to sample structural properties of the system. The re-

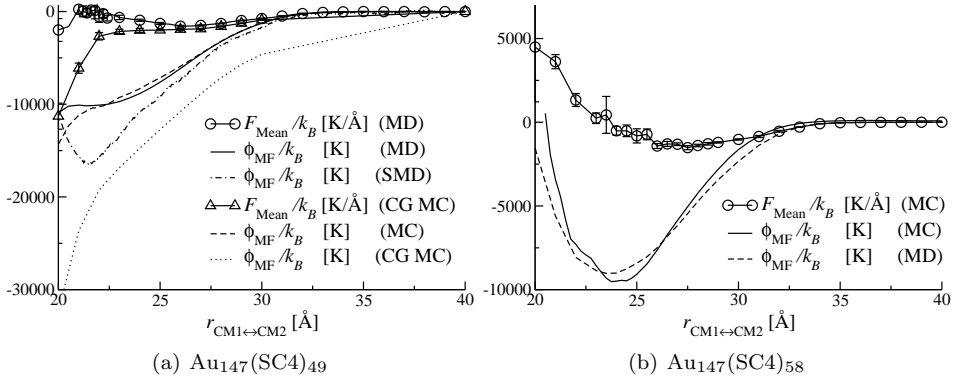


Figure 4.2: (a): Mean force F_{mean} and potential of mean force ϕ_{MF} as functions of the center of mass separation r between two Au_{147} nanocrystals capped by 49 SC4 molecules in vacuum computed using constraint MD (1 ns simulation time), compared with the same ϕ_{MF} computed using SMD (averaged over 100 simulations of 2.3 ns each); constraint MC (50000 cycles); and constraint MC with the coarse-grained NC-pseudo-atom potential (50000 cycles). (b): Mean force F_{mean} and potential of mean force ϕ_{MF} as functions of center of mass separation r between two Au_{147} nanocrystals capped by 58 SC4 molecules in vacuum computed using constraint MC (150000 cycles), compared with the same ϕ_{MF} computed using using constraint MD (1 ns simulation time). Note that F_{mean} computed using MD is equal to the MC result (within error bars) and is not shown.

cently developed effective NC–pseudo-atom interaction potential²⁵⁸ (Section 2.3) is not suited for MD because of discontinuities in the force, but it can be used in MC simulations (CG MC). The gain due to this coarse-grained potential is relatively small because most CPU time is spent on computing intermolecular interactions. This may be different however for larger NCs since the number of surfactants increases quadratically and the number of Au atoms cubically with d_c . This coarse-grained potential seems to underestimate the friction of thiol head groups on the NC surface, and therefore may yield a more attractive interaction at small distances, *c.f.* Fig. 4.2(a). We will show in Section 4.3.3 that the main issue with CG MC is the high sensitivity of the result with respect to the exact choice of the NC-radius in the coarse-grained model. At small NC separations, the PMF curve computed SMD is qualitatively different from the ones computed using constraint methods. We will show in Section 4.3.2 that the relaxation of interpenetrating capping layers occurs on time scales that are much larger than typical SMD simulation times.

MD calculations in explicit solvent were a factor five faster compared to the corresponding MC ones due to the use of an efficient neighbor list.²⁶⁰ Clearly, constraint MD is the method of choice in this case. The methods (MD or MC, simulation lengths) chosen for individual results in the remainder of this chapter are summarized in Table 4.1.

4.3 Pair interactions and the Golden Rule

In this section, our results on pair interactions between capped gold nanocrystals are presented. Fig. 4.3 shows as an example the potential of mean force between two $\text{Au}_{147}(\text{SC4})_{58}$ clusters. The left end of the horizontal axis is chosen as twice the center to corner distance r_{max} . We will call $2r_{\text{max}}$ the *fusion distance*. Note that $2r_{\text{max}} > d_c$ because the NC is not perfectly spherical (icosahedral). The PMF has a strong repulsion at distances close to the fusion distance followed by a very deep well of $\approx 30 k_B T$. Thus, in the hypothetical case when a pair of capped NCs moves freely in vacuum, a stable dimer would always be formed upon contact. The attraction ranges a few Å beyond $2r_{\text{max}}$ plus twice the ligand length (which is *ca.* 10 Å here). The Hamaker interaction between the gold cores is negligible compared to the total interaction; the PMF is dominated by interactions between capping molecules as found earlier in Ref.¹³³

In Fig. 4.4, we show the PMF for three different surfactants: SC4, SC8 and SC12 with a length $L \approx 0.5, 1$ and 1.5 nm, respectively. Surprisingly, the position of the potential minimum (determining the equilibrium distance of a NC dimer) remains constant with increasing surfactant chain length, while the total interaction becomes longer ranged and more attractive (from $30 k_B T$ for SC4 capped Au_{147} to $180 k_B T$ for SC12 capped Au_{561}). The ratio τ between the equilibrium NC center-to-center distance and d_c is in all cases ≈ 1.25 . Note that the separation between NC surfaces at the equilibrium distance is less than the length

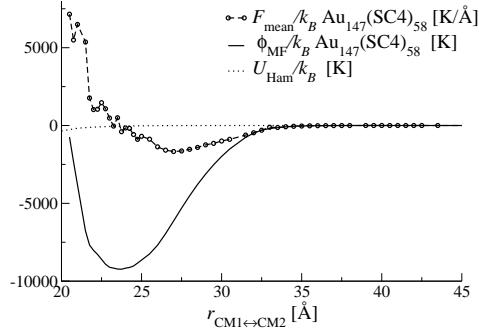


Figure 4.3: Mean force F_{mean} , potential of mean force ϕ_{MF} and Hamaker interaction energy U_{Ham} as functions of center of mass separation r between two Au₁₄₇ nanocrystals ($d_c = 1.8$ nm) capped by 58 butane-thiol molecules (SC4) each in vacuum, computed using constraint MD. The left end of the horizontal axis corresponds to the fusion distance ($2r_{\text{max}}$): twice the center to corner distance of a single NC.

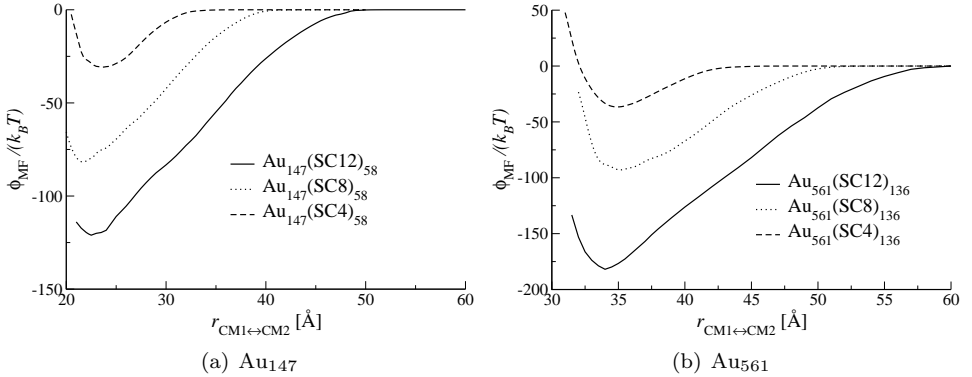


Figure 4.4: Potential of mean force ϕ_{MF} as a function of center of mass separation r between (a) two Au₁₄₇ nanocrystals ($d_c = 1.8$ nm) and (b) two Au₅₆₁ nanocrystals ($d_c = 2.7$ nm) capped by SC4, SC8 and SC12 in vacuum.

of a single capping molecule in a stretched conformation. Fig. 4.1(b) shows that this is possible because of the flexibility of aliphatic tails: the capping molecules located close to the NC–NC axis point in the direction perpendicular to this. Therefore, the alkyl tail length is not necessarily a restriction for NC spacing. We will come back to this issue in Section 4.5 where we will show that $\tau \approx 1.25$ is the distance at which the ligands of any length are packed very efficiently in the space between two NCs. Furthermore, the attractive parts of the three PMFs for different capping molecules on the same NC appear to be linear and parallel to each other. The values for the potential well depth are consistent with a previous MD study of $\text{Au}_{140}(\text{SC4})_{62}$ and $\text{Au}_{140}(\text{SC10})_{62}$.¹³³ In this study, well-depths of $45 k_B T$ and $145 k_B T$, respectively, were reported.

The PMFs for a larger NC Au_{1415} ($d_c=3.7$ nm) capped by short ligands SC2 and SC3 are compared to the ones for longer SC6 and SC12 capping molecules in Fig. 4.5(a). Note that a ligand should be at least $\frac{1.25d_c-d_c}{2} = 4.63$ Å long for the capping layers of two NCs to be in contact at NC–NC center-to-center distance of $r = 1.25d_c$. Both SC2 and SC3 are significantly shorter than this minimum length, and the spacing between the two NCs at the equilibrium distance for these short thiols equals 5 and 6.8 Å, respectively, which is in both cases approximately twice the ligand length. By contrast, the equilibrium distances for SC6 and SC12 (46.0 and 47.5 Å, respectively) are close to $1.25d_c = 46.9$ Å, and show a much weaker dependence on the chain length. We have also computed the PMF between a pair of NCs with different size $d_c^{(1)}$ and $d_c^{(2)}$ capped by the same ligand: $\text{Au}_{561}(\text{SC}n)_{136}$ – $\text{Au}_{147}(\text{SC}n)_{58}$, with $n = 4$ and 8. For such a dimer, it is natural to define an effective NC diameter $d_c^{\text{eff}} = \frac{1}{2} (d_c^{(1)} + d_c^{(2)})$. As we can see from Fig. 4.5(b), the location of the minimum again does not change with increasing chain length, and the ratio $\tau \approx 1.25$.

We summarize all PMFs presented earlier in Fig. 4.6. Note that in this figure, we plot ϕ_{MF} as function of τ . The potential minima of all PMFs lie at the line $\tau = 1.25 \pm 0.04$. Our scaling result implies a **Golden Rule**: “NC superstructures with τ close to 1.25 have an enhanced robustness and thermodynamic stability due to the large energetic contribution of the capping molecules.” Distances between adjacent capped NCs that are significantly smaller than twice the average surfactant length are often observed experimentally for thin NC films, with the ratio τ between 1.2 and 1.33.^{32,49,64,67,209,210,261,262} In Ref.,³² a monolayer of Au NCs with $d_c = 6$ nm capped by SC12 was shown to form a self-supported membrane when dropcasted on a substrate with an up to 2 μm large hole. The spacing between adjacent NCs was found to be 1.4 nm, which is less than a single surfactant chain length. This corresponds to $\tau = 1.23$, and this is an excellent example of a robust monolayer obeying the Golden Rule. In 3D-structures on the other hand, the typical distance between adjacent NCs depends on the ligand length due to the limited available volume, and our Golden Rule does not apply.^{65,134,263}

Fig. 4.6 reveals the impression that, in first approximation, the PMF well-depth is determined by the ligand length alone, and not by the NC size (and thus

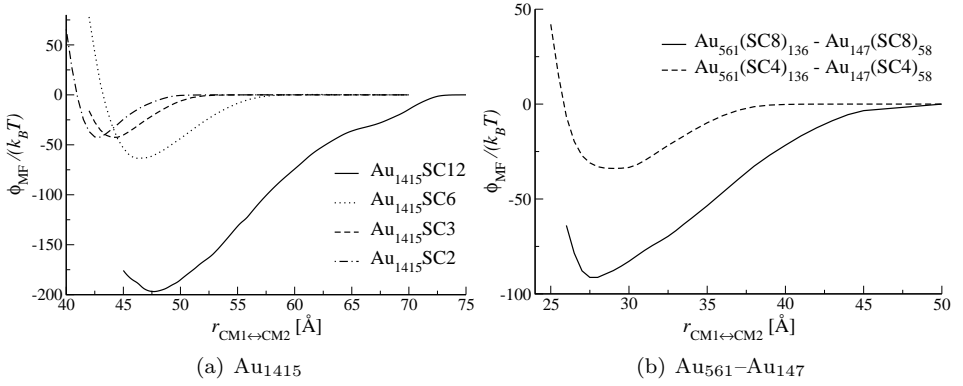


Figure 4.5: (a) Potential of mean force ϕ_{MF} as a function of center of mass separation r for Au_{1415} ($d_c=3.7$ nm) capped by SC2, SC3, SC6 and SC12. (b) $\phi_{\text{MF}}(r)$ between an Au_{561} and an Au_{147} nanocrystals capped by the same ligand.

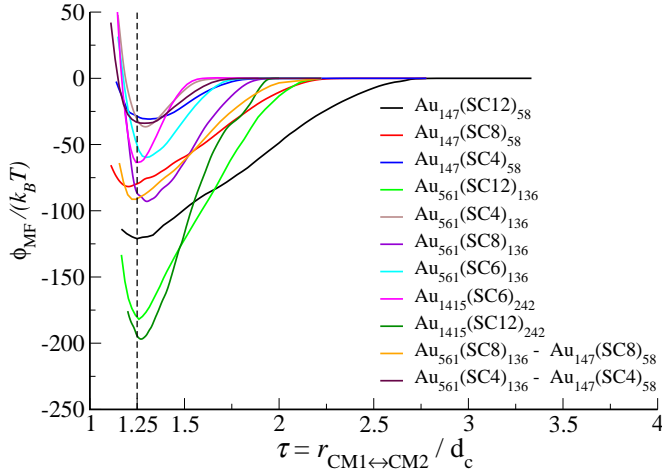


Figure 4.6: Potential of mean force ϕ_{MF} for different NC sizes and ligands as a function of center of mass separation r divided by the NC core diameter d_c . This ratio is referred to as τ in the main text. The three NCs Au_{147} , Au_{561} and Au_{1415} have core diameter $d_c = 1.8, 2.7$ and 3.7 nm, respectively; capping molecules range from butanethiol SC4 ($L \approx 0.5$ nm) to dodecanethiol SC12 ($L \approx 1.5$ nm). The vertical dashed line indicates $\tau = 1.25$, and serves as guide to the eye.

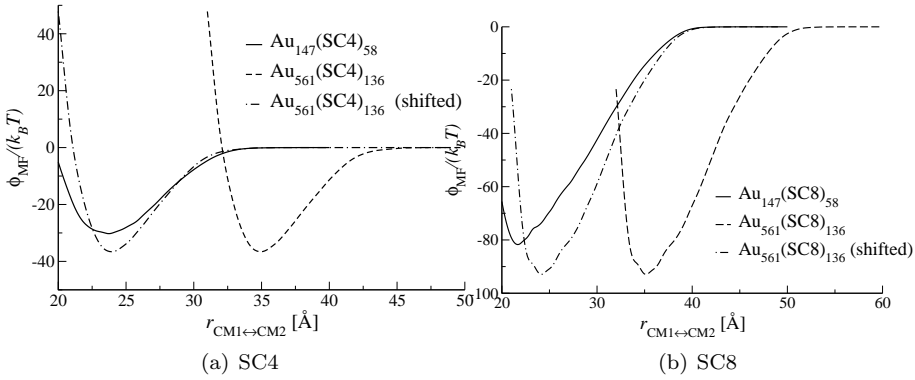


Figure 4.7: Potential of mean force ϕ_{MF} as a function of center of mass separation r between two Au_{147} nanocrystals ($d_c = 1.8$ nm) capped by SC4 (a) and SC8 (b) compared to the ϕ_{MF} between two Au_{561} nanocrystals ($d_c = 2.7$ nm) capped by the same surfactant in vacuum.

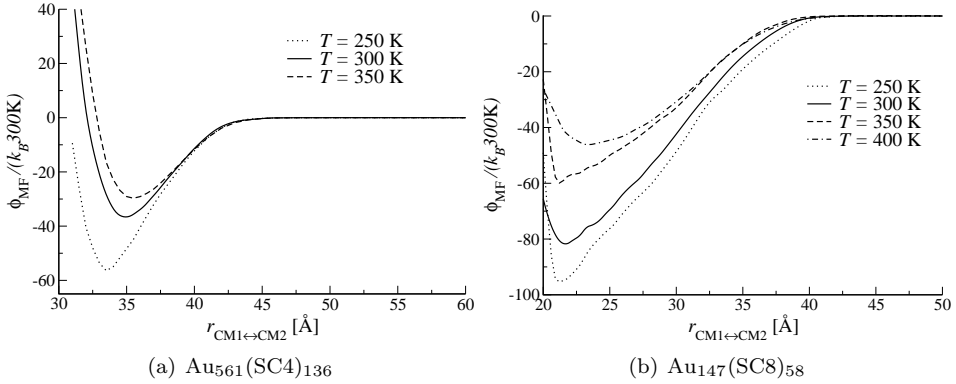


Figure 4.8: Potential of mean force ϕ_{MF} as a function of center of mass separation r between two SC4 capped Au_{561} nanocrystals (a) and two SC8 capped Au_{147} NCs (b) at different temperatures in vacuum. For a fair comparison, the PMF is divided by $k_B T$ at $T = 300$ K.

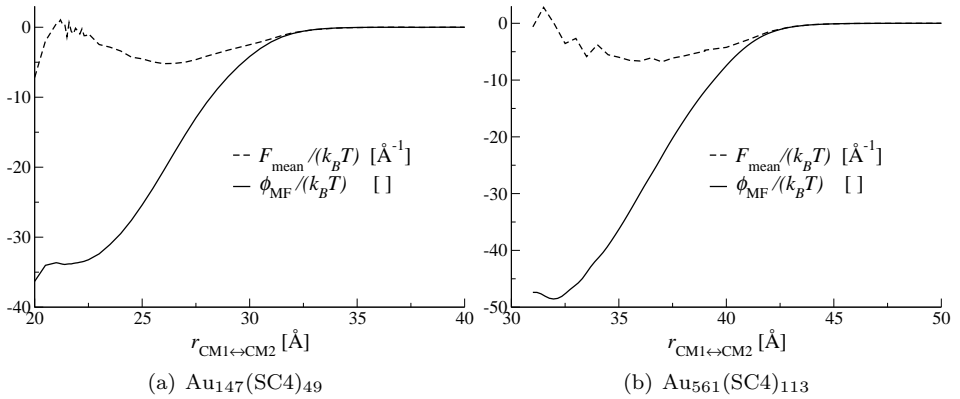


Figure 4.9: PMF $\phi_{MF}(r)$ between (a) two Au_{147} nanocrystals ($d_c = 1.8$ nm) capped by 49 SC4 molecules, and (b) between two Au_{561} nanocrystals ($d_c = 2.7$ nm) capped by 113 SC4 molecules in vacuum. In both cases, the number of surfactants is 15% smaller than in a full capping layer.

not by the number of capping molecules); the only exception is $\text{Au}_{147}(\text{SC12})_{58}$. A close comparison of the PMFs between two NCs of different size ($d_c = 1.8$ nm and 2.7 nm) capped by the same surfactant yields that for larger NCs, the repulsion is steeper compared to smaller ones, and the potential well is deeper and more narrow, see Fig. 4.7. These observations can be explained by the smaller surface curvature for the larger NC, yielding a smaller angle between adjacent surfactants and therefore a denser capping layer. For the same reason, the well-depth for $\text{Au}_{147}(\text{SC12})_{58}$ is much lower than for $\text{Au}_{561}(\text{SC12})_{136}$ and for $\text{Au}_{1415}(\text{SC12})_{242}$, see Fig. 4.6.

The PMF for a pair of $\text{Au}_{561}(\text{SC4})_{136}$ and for a pair of $\text{Au}_{147}(\text{SC8})_{58}$ clusters at different temperatures are shown in Fig. 4.8. The interaction becomes less attractive with increasing temperature while the equilibrium distance becomes slightly larger, which is due to the increasing entropic repulsion of the chains.¹²¹ Note the large difference in well-depth between $T = 250$ K and $T = 300$ K in Fig. 4.8(a) and between $T = 300$ K and $T = 350$ K in Fig. 4.8(b). This is caused by a transition inside the capping layer known as *chain melting*^{131,135,136} (see also Section 2.6 of this work).

In Ref.,⁴⁹ a 2D binary superlattice of decanethiol stabilized Au NCs of two different sizes was left for two weeks under ambient conditions. TEM images showed that smaller NCs started to sinter, while the larger ones remain intact. The authors suggest that this could be due to capping layer degradation. We mimic a partial evaporation of the surfactant from the capping layer by simulating nanocrystals capped by 15% less ligands with respect to a fully covered NC surface. The potential of mean force in Fig. 4.9 shows that the repulsive part

almost vanishes, and that the PMF even becomes attractive at separations very close to the fusion distance. Thus, incomplete capping layers bring the surfaces of the NCs into contact and even promote their fusion. This effect is more pronounced for smaller nanocrystals. For the larger NC, there is a small repulsive force close to the fusion distance, which is in line with the steeper short-range repulsion observed in Fig. 4.7.

4.3.1 Parameterization of effective NC pair interactions

To make the computed pair interactions applicable in further studies, it is desirable to develop an interaction model for capped Au NCs that depends on the core diameter d_c and the number of carbon atoms in the alkyl tail n . One can estimate the ligand length L by applying the commonly used empirical formula $L \approx (n+1) \times 1.2 \text{ \AA}$.^{65,132} In this section, we present a potential form that captures the basic properties of the effective interactions computed in Section 4.3. Note that we do not try to make a collective fit of all PMFs. We only consider here the case that the ligand is not too short: $L > (1.25d_c - d_c)/2$; and the temperature is $T = 300 \text{ K}$.

The values U_{\min} of the potential well-depth for different ligands SC n can be fitted to the empirical formula $U_{\min}/k_B T = -u_0(n+1)^2$, and the parameter $u_0 \approx 1.15$ is in first approximation NC size independent, see Fig. 4.10(a). In particular, the effective attraction scales quadratically with the number of beads in the capping molecule. We have shown earlier that the pre-factor u_0 decreases significantly with increasing temperature, see Fig. 4.8.

We suggest the following potential form for the two-body interactions:

$$\phi_{\text{MF}}^{2\text{body}}(r) = f_{\text{sm}}(r) (a(r - r_{\text{cut}}) + b \exp\{-c(r - r_{\min})\}); \quad (4.6a)$$

where $r_{\text{cut}} = 1.2d_c + 2L$ is the cut-off radius; the parameter c determines the repulsion steepness; the parameters a and b can be expressed in terms of c , the location $r_{\min} = 1.25d_c$ and the value U_{\min} of the potential minimum by

$$a = \frac{U_{\min}}{r_{\min} - r_{\text{cut}} + 1/c}, \quad b = \frac{a}{c} = \frac{U_{\min}}{(r_{\min} - r_{\text{cut}})c + 1}. \quad (4.6b)$$

The smoothing cut-off function is given by

$$f_{\text{sm}}(r) = \begin{cases} \exp\left(0.05 \frac{d_c (r_{\min} - r)}{(r - r_{\text{cut}})(r_{\min} - r_{\text{cut}})}\right) & r < r_{\text{cut}} \\ 0 & r \geq r_{\text{cut}}. \end{cases} \quad (4.6c)$$

When choosing $c = 0.55 \text{ \AA}^{-1}$, $r_{\min} = 1.25d_c$ and $U_{\min}/k_B T = -1.15(n+1)^2$, the potential Eq. 4.6 reproduces the following properties observed in Section 4.3:

- The equilibrium distance is for any ligand at $r_{\min} = 1.25d_c$.

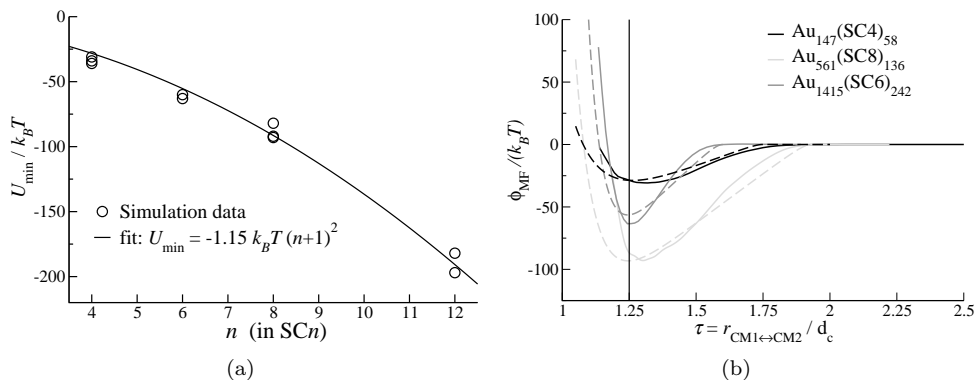


Figure 4.10: (a) Potential well depths U_{\min} from Fig. 4.6 plotted against the number n of carbon atoms in the ligand tail. The value for Au₁₄₇(SC12)₅₈ is omitted. (b) Some computed two-body PMFs from Fig. 4.6 (solid lines) and the potential Eq. (4.6) with the parameters corresponding to each system (dashed lines). As in Fig. 4.6, the scaled distance τ is used on the horizontal axis, and the vertical line indicates $\tau = 1.25$.

- The interaction ranges a few \AA beyond $r_{\text{ovrl}}^{2b} = d_c + 2L$ which is the NC diameter plus twice the ligand length; for $r > r_{\text{ovrl}}^{2b}$ the PMF smoothly approaches 0.
- The potential well-depth is $U_{\min}/k_B T = -1.15(n+1)^2$.
- The attractive part of the 2-body PMF is almost linear.
- The repulsion is steep in the range $1.1d_c < r < 1.25d_c$.

Moreover, both the potential and its derivative are continuous at the cut-off owing to the smoothing function f_{sm} . Three typical PMFs from Fig. 4.6 with different NC cores and ligands are compared to the potentials from Eq. (4.6) in Fig. 4.10(b). The agreement is reasonable when taking into account that we did not perform a collective fit. It can be seen on the example of Au₅₆₁(SC8) that the differences are mainly due to the small deviations of the imposed values for r_{\min} and U_{\min} from the computed ones.

4.3.2 Shape memory effects

To enable mutual interpenetration of two capping layers, several capping molecules have to change their conformation simultaneously. Some of these conformational changes will have high activation energies, and this results in very slow kinetics. We therefore investigate whether it is possible to find the equilibrium distance from *unconstrained* MD or MC simulations. We considered two systems:

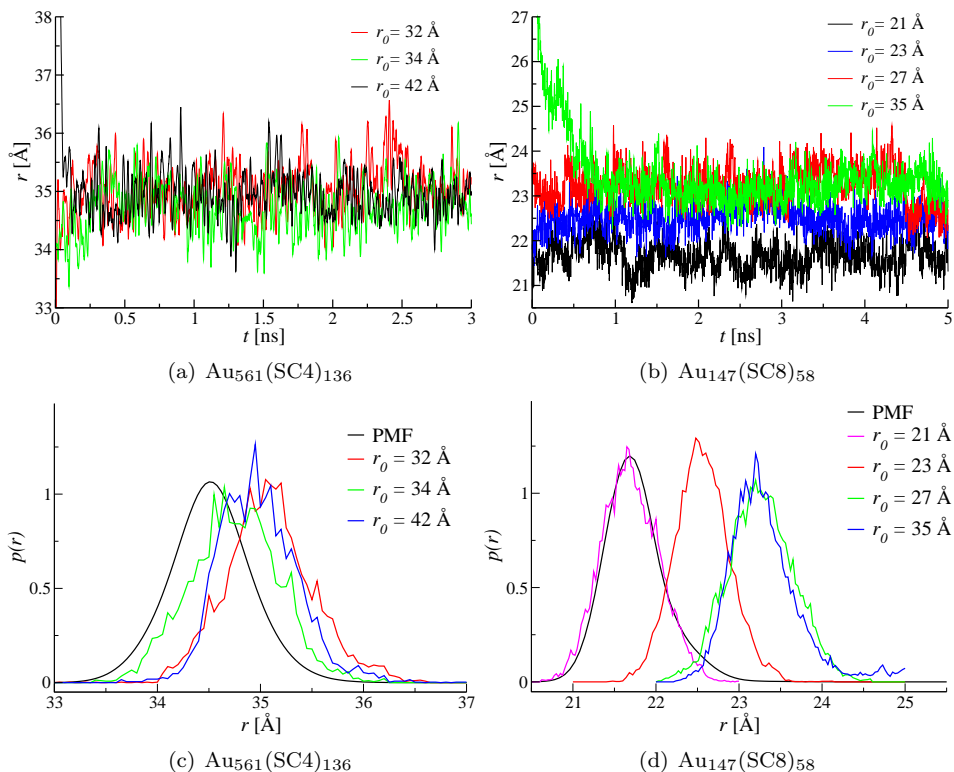


Figure 4.11: Top: Distance r between NC centers during unconstrained MD simulations starting from different initial distances r_0 for a pair of $\text{Au}_{561}(\text{SC4})_{136}$ clusters (left) and $\text{Au}_{147}(\text{SC8})_{58}$ clusters (right). Bottom: Distance probability distributions $p(r)$ computed from the PMF and unconstrained MD simulations starting from different NC separations.

$\text{Au}_{561}(\text{SC4})_{136}$ and $\text{Au}_{147}(\text{SC8})_{58}$. The starting configurations were chosen from well-equilibrated constraint simulations at different distances r_0 . We simulated the systems using unconstrained MD for 3 ns and 5 ns for $\text{Au}_{561}(\text{SC4})_{136}$ and $\text{Au}_{147}(\text{SC8})_{58}$, respectively. These simulation lengths are typical for simulations of capped NCs found in literature.^{132,133} After 100 ps, the two clusters reach a certain separation after which the distance between them is fluctuating around some average value, *c.f.* Figs. 4.11(a) and (b). In addition, there is no drift in energy, suggesting that the system is already in equilibrium.

We recorded the probability $p(r)$ of finding the two NC centers at a distance r , and compared it to the one calculated from the associated PMF $\phi_{\text{MF}}(r)$:

$$p(r) \propto r^2 \exp[-\phi_{\text{MF}}(r)/k_B T]. \quad (4.7)$$

The distributions for the $\text{Au}_{147}(\text{SC8})_{58}$ are clearly different for varying initial separations. The simulation starting closest to the equilibrium distance ($r_0 = 21 \text{ \AA}$) yields the distance probability distribution closest to the one calculated from the PMF, *c.f.* Fig. 4.11(d). This shows that several conformations of capping molecules and thus some NC separations cannot be reached in a feasible simulation time using unconstrained MD simulations. In a constraint simulation, on the other hand, the capping molecules are forced to find favourable conformations at all NC separations. Note that constraint MD and MC yield similar results even at short distances (see Fig. 4.2(b)) despite the different strategies for exploring the configuration space. We conclude that unconstrained brute-force simulations of ensembles of capped nanocrystals require very long simulation times to reproduce the equilibrium properties such as the equilibrium distance correctly. In practice, this observation is important for understanding mechanical properties of NC superstructures. These materials have *shape memory effects*: in response to an external perturbation, a restoring force is acting for a time period much longer than diffusion time². This restoring force, on the other hand, makes it very difficult to obtain accurate results using SMD, or with any other unconstrained method.

4.3.3 The trouble with coarse-grained NCs

In Section 4.2.3 we showed that the effective interaction computed using constraint MC with the coarse-grained NC–pseudoatom potential taken from Section 2.3 of this thesis is much more attractive than the one computed using a full-atom model. At first sight, this is somewhat surprising as the main contribution to PMF comes from the ligand–ligand interactions. Partially, the stronger attraction in the CG model can be explained by the missing friction of the headgroups on the surface, which is present in the rigid full-atom model. There is, however, another subtle detail.

We computed the PMF for the $\text{Au}_{147}(\text{SC4})_{58}$ pair, where we fixed the number of capping molecules and slightly changed the in-radius r_{in} of the icosahedron in the CG-potential from 6.5 to 6.3 \AA (see Fig. 2.2 in Section 2.3 for the definition of this parameter). The computed PMFs are shown in Fig. 4.12 together with the full-atom result from Fig. 4.3. The PMF for the CG NC with $r_{\text{in}} = 6.5 \text{ \AA}$ looks like the capping layer is incomplete (*c.f.* Fig. 4.9). The PMF corresponding to $r_{\text{in}} = 6.5 \text{ \AA}$ is similar to the one for the full-atom model, but still seems to underestimate the repulsion: the potential well-depth is both deeper and at a slightly smaller NC separation than in the full-atom model. Thus, a small difference in the mapping procedure of a full-atom NC on an effective icosahedron results in a large difference in the result.

²Consider a dumbbell with the same effective mass as a $\text{Au}_{147}(\text{SC8})_{58}$ –dimer and with a harmonic potential approximating the associated PMF around its well-depth. Within a 5 ns period, such a dumbbell would perform more than 20 full oscillations.

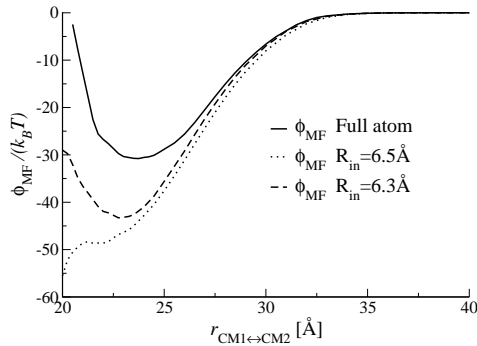


Figure 4.12: Potential of mean force ϕ_{MF} as a function of center of mass separation r between two Au_{147} nanocrystals capped 58 SC4 ligands each, computed using the full-atom model and the CG-model from Section 2.3 for two different values (6.3 and 6.5 Å) of the icosahedron in-radius.

As we have seen already and will discuss further in Section 4.5, the PMF is very sensitive to the coverage. When the number of capping molecules is kept constant, the coverage is determined by the surface area and, therefore, by the exact choice of the icosahedron size. It can be concluded that the main source of differences between results obtained using the CG and the full-atom models is the mapping procedure of a NC with atomic details on an effective icosahedron. To circumvent this problem, one should compute the (maximum) number of ligands for the CG model with the given r_{in} , and compute the PMF with this system.

4.4 Three-body effects

In Section 4.3, we have studied interactions between pairs of capped nanocrystals. The crucial question is, in which cases these pair potentials are sufficient to reasonably model large NC superstructures. We have found that, surprisingly, the equilibrium distance of NC dimers is independent from the ligand length L , and is $\approx 1.25d_c$, where d_c is the NC core diameter (see Fig. 4.6). By contrast, experiments show that the spacing between NCs in a 3D-superlattice systematically increases with increasing length of the capping molecules at constant core diameter.^{65,134,264} This indicates that pair-interactions alone may not be appropriate to describe 3D superstructures built from NCs with long capping molecules. On the other hand, pair potentials are sufficient to describe the energy of 1D superstructures (chains or rings) of capped NCs. In a similar fashion, a study of three-body interactions would allow us to apply the computed effective interactions to simulate 2D NC superstructures (monolayers). We are not aware of systematic experimental studies of monolayers made from Au NCs with constant core size

and varying ligand length. In Ref.⁶⁶ it was shown that the spacing between 5.8 nm Ag₂S NCs increases non-linearly with L ; and the spacing was almost the same for SC12 and SC14. This indicates that three-body effects may determine the spacing between NCs in a non-trivial way.

One of the difficulties in quantifying many-body effects is the number of internal coordinates involved. For a pair of (quasi-)isotropic objects (such as capped NCs in the present work), it is sufficient to consider the PMF as a function of only one parameter (here: NC center-to-center distance). In a system of three isotropic objects, one already needs three coordinates to describe all different configurations. If one wishes to explore all degrees of freedom of this system, the number of required simulations would increase cubically compared to a similar parameterization study of the corresponding two-body system. Without any additional information about the system, the computational costs required to parameterize three-body interactions are therefore much larger compared to a parameterization of isotropic pair-interactions. If a three-body contribution to the total energy is necessary, one has to find a suitable potential form to make the computed interactions applicable in practice. This task is immensely simplified when one knows the nature of the interaction *a priori*. For instance, the energy of three consecutive beads in a chain molecule can be often decomposed into two bond stretching and one bond bending potentials. Unfortunately, such knowledge is not available for most soft-matter systems. Currently, simulation and theoretical studies mainly show presence or absence of many-body effects in one specific arrangement.^{265–268} In Refs.,^{265,268} e.g., the three-body force in a triplet of star polymers and dendrimers, respectively, was studied. The three objects were placed in an equilateral triangle, and mean force was computed as a function of the side length. It was concluded in Refs.^{265,268} that three-body interactions are repulsive and have a significant contribution to the total energy. By contrast, an attractive three-body interaction was found for charged colloids in Ref.²⁶⁷

Our approach is to decompose the total interaction between three NCs into a sum of effective pair interactions. If no three-body effects are present, these pair interactions will be identical to the ones presented in Section 4.3. Our simulation setup is sketched in Fig. 4.13(a). The centers NC1, NC2 and NC3 of three capped NCs are constraint to the corners of an isosceles triangle, where the NC1–NC3 and NC2–NC3 distances (denoted by r_{13} and r_{23} , respectively) are equal. A typical simulation snapshot is shown in Fig. 4.13(b). The degrees of freedom of ligand molecules and rotational degrees of freedom of the NCs are sampled using MC in the NVT ensemble. The mean force $F_{\text{mean}}(r_{3C})$ between NC3 and the NC1–NC2 midpoint C is calculated from

$$F_{\text{mean}}(r_{3C}) = \frac{1}{2} \left\langle \left(\vec{F}_C - \vec{F}_3 \right) \cdot \vec{r}_u \right\rangle_{\text{NVT}} \quad (4.8)$$

where \vec{F}_C and \vec{F}_3 are the total forces acting on C and NC3, respectively; r_{3C} is the distance between the two points and $\vec{r}_u = \vec{r}_{3C}/r_{3C}$ is the unit vector between them. The angular brackets denote an average in the canonical ensemble. As

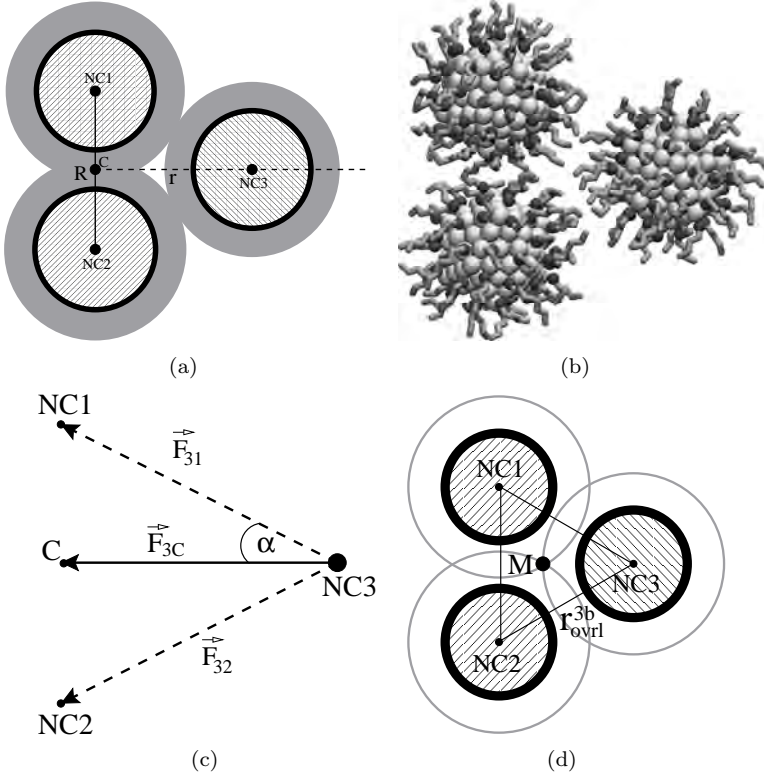


Figure 4.13: (a) The setup of a constraint simulation of three NCs. NC cores are represented by shaded circles; the capping layers by grey rings. The centers of mass of the three NCs are constraint at positions denoted by NC1, NC2 and NC3 respectively. The midpoint between NC1 and NC2 is labeled as C . In a series of simulations, the distance $R = R_{12}$ between NC1 and NC2 is kept constant, while the distance $r = r_{3C}$ between C and NC3 varies. (b) A simulation snapshot of a $\text{Au}_{147}(\text{SC4})_{58}$ triplet with $R = 24.5 \text{ \AA}$ and $r = 27 \text{ \AA}$. Representations same as in Fig. 4.1. (c) Forces in the 3-NC system that are used to quantify the three-body effects. The mean force between NC3 and C , $|\vec{F}_{3C}|$, is sampled from a constraint simulation as in (a). The effective forces between NC3 and NC1 (NC2) are denoted by \vec{F}_{31} (\vec{F}_{32}). If no three-body interactions are present in the system, then the magnitudes of these effective forces are equal to the two-body mean force F_{mean} at the corresponding distance, and $|\vec{F}_{3C}| = 2 |\vec{F}_{31}| \cos \alpha$. (d) Schematic representation of the triplet overlap distance r_{ovrl}^{3b} . The capping layer boundaries of the three NCs, represented by grey lines, intersect in the midpoint M of the equilateral triangle with corners in NC1, NC2 and NC3.

Table 4.2: Geometric data of the two NC systems described in the text. All distances are reported in Å.

	L	r_{ovrl}^{2b}	r_{ovrl}^{3b}	$r_{\text{eq}}^{2\text{body}}$
formula		$d_{\text{NC}} + 2L$	$\frac{\sqrt{3}}{2} r_{\text{ovrl}}^{2b}$	
Au ₁₄₇ (SC4) ₅₈	4.8	27.6	23.9	23.7
Au ₁₄₇ (SC8) ₅₈	9.6	37.2	32.2	21.6

shown in Fig. 4.13(c), this force can be decomposed into a vector sum of two forces \vec{F}_{13} and \vec{F}_{23} acting between NC1 and NC3, and NC2 and NC3, respectively. The forces \vec{F}_{13} and \vec{F}_{23} are equal in magnitude by symmetry, so that we can define the effective two-body force $F_{\text{eff}}(r_{13})$ in the three-body system as

$$F_{\text{eff}}(r_{13}) = |\vec{F}_{13}|(r_{13}) = |\vec{F}_{13}|(r_{23}) = \frac{F_{\text{mean}}(r_{3C})}{2 \cos \alpha} \quad (4.9)$$

with $r_{13} = \frac{r_{3C}}{\cos \alpha}$. As shown in Fig. 4.13(c), α is the angle between the points C , NC3 and NC1 (or NC2). We perform a series of simulations in which the distance R_{12} between NC1 and NC2 is kept constant, while r_{3C} is different in each simulation. Integrating the effective force $F_{\text{eff}}(r_{13})$ with respect to the distance r_{13} , we obtain the effective PMF $\phi_{\text{MF}}^{\text{eff}}(r_{13})$

$$\phi_{\text{MF}}^{\text{eff}}(r_{13}) = \int_{r_{13}}^{\infty} F_{\text{eff}}(r') dr'. \quad (4.10)$$

We consider two systems with the same NC ($d_c = 18$ Å) capped by butane- and octanethiol: Au₁₄₇(SC4)₅₈ and Au₁₄₇(SC8)₅₈. A typical simulation snapshot is shown in Fig. 4.13(c). The geometric properties of the two systems are characterized by the following distances, which are summarized in Table 4.2:

- Ligand length L ;
- NC core diameter $d_c = 18$ Å;
- Interpenetration distance $r_{\text{ovrl}}^{2b} = d_c + 2L$ between two NC centers, which is the center-to-center distance for a NC pair at which the two capping layers touch each other;
- Triplet interpenetration distance $r_{\text{ovrl}}^{3b} = \left(\frac{d_c}{2} + L\right) \sqrt{3}$ between two NC centers: if three NCs are arranged in an equilateral triangle, this would be the maximum side length at which the three capping layers overlap in the triangle midpoint (see Fig. 4.13(d));
- Equilibrium distance of the 2-body PMF $r_{\text{eq}}^{2\text{body}}$, taken from Fig. 4.6;

- Equilibrium distance of the effective 2-body PMF in the 3-body system, $r_{\text{eq}}^{\text{eff}}$.

The SC4 ligand is relatively short ($\approx 5 \text{ \AA}$), and the interpenetration range at the well-depth of the associated PMF is slightly smaller than one capping molecule. The second ligand (SC8) is two times longer than SC4, and has a very large interpenetration range of more than 1.5 capping molecules, see Fig. 4.6. For the SC4 ligand, we chose R_{12} separations of 23.5 and 24.5 \AA , which are both close to the dimer equilibrium distance $r_{\text{eq}}^{2\text{body}}$. For the longer SC8 ligand, we computed the effective pair interaction $\phi_{\text{MF}}^{\text{eff}}$ for $R_{12} = 23.5, 24.5, 26.0$ and 30.0 \AA .

The calculated effective forces F_{eff} and pair interactions $\phi_{\text{MF}}^{\text{eff}}$ for the two systems are shown in Fig. 4.14. If no 3-body effects were present, $\phi_{\text{MF}}^{\text{eff}}$ would be identical to the 2-body PMF $\phi_{\text{MF}}^{2\text{body}}$ from Section 4.3. The difference between $\phi_{\text{MF}}^{\text{eff}}$ and $\phi_{\text{MF}}^{2\text{body}}$ is in all cases very small for $r > r_{\text{ovr1}}^{2b}$, i.e. when the capping layer of NC3 does not overlap with the other two capping layers. For smaller r_{13} distances, the 3-body interaction becomes increasingly repulsive. In all cases, the equilibrium distance shifts towards larger separations.

In a $\text{Au}_{147}(\text{SC4})_{58}$ triplet, the effective interaction between NC pairs becomes 20% less attractive compared to the 2-body case. The location of the $\phi_{\text{MF}}^{\text{eff}}$ well-depth decreases by 1 \AA (4.2%) compared to $\phi_{\text{MF}}^{2\text{body}}$. The effective interactions $\phi_{\text{MF}}^{\text{eff}}$ computed for two different R_{12} separations lie within statistical accuracy. When a $\text{Au}_{147}(\text{SC4})_{58}$ triplet is arranged in an equilateral triangle with side length equal to $r_{\text{eq}}^{\text{eff}} \approx 24.7 \text{ \AA}$, the distance from each NC center to the midpoint of the triangle is $r_{\text{eq}}^{\text{eff}}/\sqrt{3} = 14.3 \text{ \AA}$. This is slightly larger than the distance $d_c/2 + L$ from a NC center to the capping layer boundary, so that there the three capping layers only overlap pairwise. On the other hand, in a triangle with side equal to $r_{\text{eq}}^{2\text{body}} \approx 23.7 \text{ \AA}$, the distance to the triangle midpoint would be 13.7 \AA , which is slightly smaller than $d_c/2 + L$. This would allow an overlap of the three capping layers. Thus, for the short ligand the shift of the equilibrium distance can be rationalized as avoiding a triplet overlap.

For a $\text{Au}_{147}(\text{SC8})_{58}$ system, the effective interactions corresponding to $R_{12} = 23.5, 24.5$ and 26.0 \AA are very similar. As expected, $\phi_{\text{MF}}^{\text{eff}}$ corresponding to $R_{12} = 30.0 \text{ \AA}$ lies between the one for $R_{12} = 26.0 \text{ \AA}$ and the two-body PMF $\phi_{\text{MF}}^{2\text{body}}$, as the three-body effects become weaker for increasing separation R_{12} between NC1 and NC2. The location of the $\phi_{\text{MF}}^{\text{eff}}$ well-depth increases by 3 \AA (14%) compared to $\phi_{\text{MF}}^{2\text{body}}$. The effective pair-interaction $\phi_{\text{MF}}^{\text{eff}}$ is up to $\approx 40\%$ less attractive than $\phi_{\text{MF}}^{2\text{body}}$. This may have a strong consequence for the formation of $\text{Au}_{147}(\text{SC8})_{58}$ aggregates at the air-water interface. In the pioneering study of Heath *et al.* it was observed that NCs capped by long ligands organize into linear structures at the air-water interface at low surface pressures, while foam-like structures form at higher surface pressures.⁶³ The authors of this study already speculated that effective three-NC interactions are responsible for such behaviour. Our work provides direct evidence for this speculation. This can be seen as follows. Consider

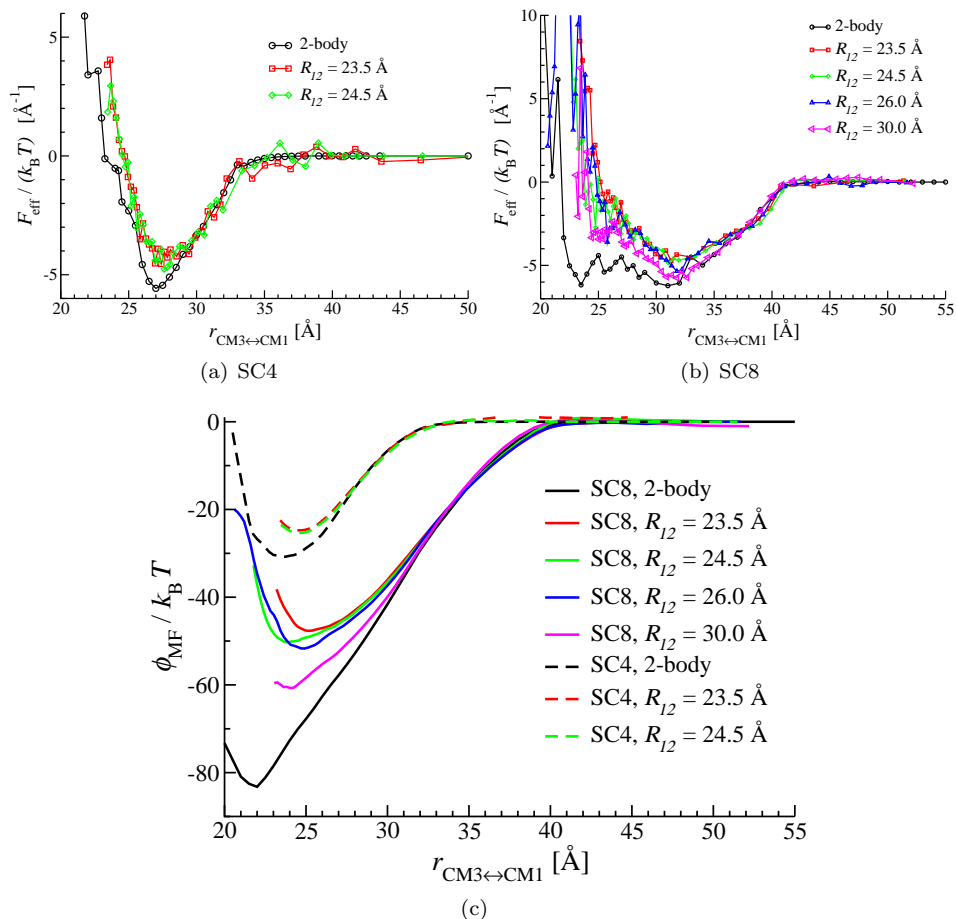


Figure 4.14: (a, b) Effective force F_{eff} in a three-NC system from Fig. 4.13 as a function of NC distance r_{13} in (a) $\text{Au}_{147}(\text{SC4})_{58}$, and (b) $\text{Au}_{147}(\text{SC8})_{58}$ triplets. (c) Effective pair potential $\phi_{\text{MF}}^{\text{eff}}$ in a three-NC system from Fig. 4.13 as a function of NC distance r_{13} in $\text{Au}_{147}(\text{SC4})_{58}$ and $\text{Au}_{147}(\text{SC8})_{58}$ triplets. The 2-body interactions are taken from Fig. 4.4(a).

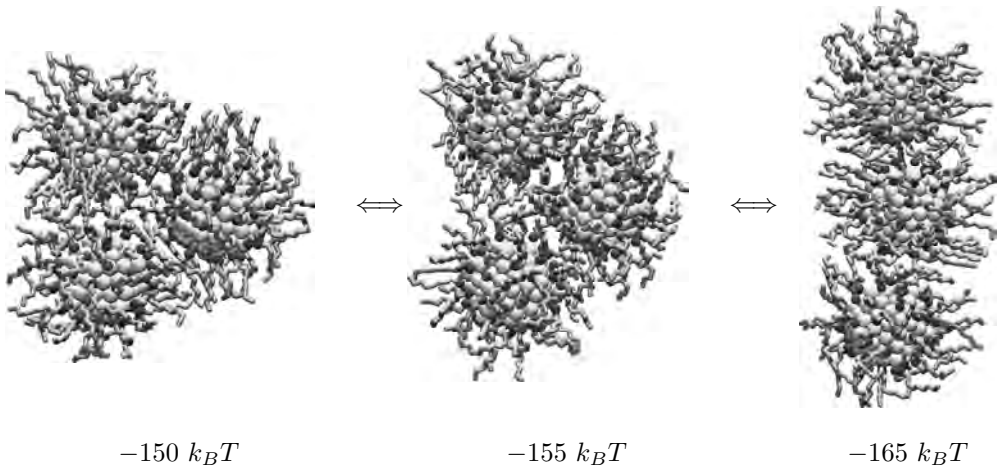


Figure 4.15: Three different configurations of a $\text{Au}_{147}(\text{SC8})_{58}$ triplet: equilateral triangle, chain and an intermediate configuration. The total interaction energies of the clusters are computed using Fig. 4.14(c).

two possible configurations for a triplet of $\text{Au}_{147}(\text{SC8})_{58}$ clusters: three in a row and equilateral triangle, each with energetically most favourable distances, see Fig. 4.15. In the first case, 3-body interactions are absent, and the total energy of this configuration is twice the well depth of $\phi_{\text{MF}}^{2\text{body}}$, which is $U_{\text{chain}}/k_B T \approx -165$. In the second case, the energy of the triplet is three times the well-depth of $\phi_{\text{MF}}^{\text{eff}}$. From the three PMFs corresponding to $R_{12} = 23.5, 24.5$ and 26.0 \AA we can make an estimate $U_{\text{triangle}}/k_B T = -150 \pm 5$. Once a triangle is formed, it can easily “straighten”, as shown in Fig. 4.15. To see this, consider a triangle with $R_{12} = 30 \text{ \AA}$, and $r_{13} = r_{23} = 24 \text{ \AA}$, which is a possible intermediate configuration between an equilateral triangle and a chain. From the effective interactions in Fig. 4.14(c), we can estimate the energy of this configuration as $\approx -155 k_B T$ (assuming a NC1–NC2 contribution of $35 k_B T$). Therefore, the linear arrangement of the triplet is energetically preferred over the triangle for long capping molecules. This is an interesting example of a spontaneous anisotropic assembly of isotropic entities.

Surprisingly, $r_{\text{eq}}^{\text{eff}}$ is the same for the two ligands despite the difference in length by 5 \AA . The question whether this agreement is coincidental or systematic cannot be answered with the available data; further investigation is necessary using both experiments and simulations. On one hand, the separation between SC4-capped NCs can be explained in terms of the avoiding of a triple overlap (see above). Independently from this argument, we will show in Section 4.5 that the three-body equilibrium distance for SC8-capped NCs can be understood as the densest possible packing of ligand chains. On the other hand, a “ligand-independent”

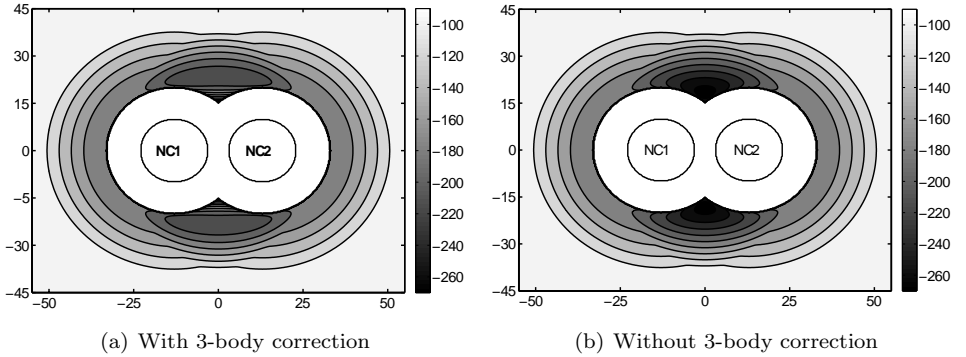


Figure 4.16: Potential energy surface of a $\text{Au}_{147}(\text{SC8})_{58}$ triplet as a function of position of the center of the third NC. The distance between the first and the second NC (NC1 and NC2) is fixed at $R_{12} = 26 \text{ \AA}$. The energy in units of $k_B T$ is computed (a) using the pair potential Eq. (4.6) with the 3-body correction of Eq. (4.11), and (b) using only the pair potential Eq. (4.6). The unit of distance is \AA . The inner white circles represent the cores of NC1 and NC2; the white rings around them are the regions that are not accessible to the center of the third NC due to core–core overlap. These regions should not be confused with the capping layers.

three-body equilibrium distance would be a possible continuation of the universal scaling for the two-body interactions found in Section 4.3.

4.4.1 Parameterization of triplet interactions

In Section 4.4 we have seen that three-body effects are not very large for a relatively short ligand $2L < 0.5d_c$. We feel that in this range they can either be neglected completely or considered implicitly by making the two-body interactions from Section 4.3.1 slightly less attractive. However, three-body effects for a long ligand are much larger than for a short one. If one either neglects them or replaces them by an effective pair interaction, it is expected that several important properties of the system will not be reproduced correctly. In this section, we present a model for effective interactions in a $\text{Au}_{147}(\text{SC8})_{58}$ triplet that captures our main findings from Section 4.4 on this system.

We propose the following correction term for each of the pair interactions ϕ_{MF} :

$$\begin{aligned} \phi_{\text{MF}}^{\text{eff}}(r_{ij}) - \phi_{\text{MF}}^{\text{2body}}(r_{ij}) = & \kappa (r_{\text{ovrl}}^{2b} - r_{ij})^3 (r_{\text{ovrl}}^{2b} - r_{ik})^2 (r_{\text{ovrl}}^{2b} - r_{jk})^2 \times \\ & \times \Theta(r_{\text{ovrl}}^{2b} - r_{ij}) \Theta(r_{\text{ovrl}}^{2b} - r_{ik}) \Theta(r_{\text{ovrl}}^{2b} - r_{jk}) \quad (4.11) \end{aligned}$$

where the indices i, j, k run over 1,2,3; and the Heaviside step function Θ is defined

as

$$\Theta(x) = \begin{cases} 1 & x > 0 \\ 0 & x < 0 \end{cases} \quad (4.12)$$

and the parameter $\kappa/k_B T \approx 3 \times 10^{-7} \text{ \AA}^{-7}$ for the $\text{Au}_{147}(\text{SC8})_{58}$ system that we studied in Section 4.4. This potential reproduces the following properties of the effective interaction in a $\text{Au}_{147}(\text{SC8})_{58}$ triplet:

- The three-body correction vanishes if any distance in a triplet becomes larger than $r_{\text{ovr1}}^{2b} = d_c + 2L$, which is guaranteed by the Θ -functions.
- The correction term becomes larger when each of the three distances becomes shorter.
- The equilibrium distance in an equilateral triangle increases by 4 \AA ; the potential well becomes 40% higher.

Moreover, the resulting potential and its derivatives are continuous.

A typical potential energy surface for the $\text{Au}_{147}(\text{SC8})_{58}$ triplet computed using Eq. 4.6 for $\phi_{\text{MF}}^{2\text{body}}$ and Eq. (4.11) for the 3-body correction is shown in Fig 4.16. Note that the 3-body correction term not only weakens the attraction, but also strongly deforms the low-energy regions. The minimum-energy region is parallel to the NC1–NC2 pair when the 3-body correction is added (see Fig. 4.16(a)), which is not the case without the correction term (see Fig. 4.4.1).

4.5 Equilibrium distance by optimal packing

In this section we will rationalize the scaling results for the equilibrium distance between capped NCs found in Sections 4.3 and 4.4. The variables of interest are the center to center distance r between a pair of NCs with diameter d_c , and ligand length L . Here, NC cores are considered as spheres of diameter d_c . It is convenient to introduce scaled variables $\tau = \frac{r}{d_c}$ and $\lambda = \frac{2L}{d_c}$. The goal of this section is to establish a relation for the equilibrium distance τ_{eq} of the form $\tau_{\text{eq}} = \tau_{\text{eq}}(\lambda)$.

The equilibrium distance between a pair of interacting capped NCs is the separation at which the total force on each NC vanishes. Given the strong vdW-attraction between capping layers in vacuum, the repulsive forces must also become very large at the equilibrium distance. This happens if one or more ligand molecules are over-compressed, as an alkane chain requires a certain minimum volume. If a capping molecule is confined into a too small volume, it exerts a large repulsive force. This observation suggests the following constituting equation for all packing models:

$$V_{\text{lig}}(\tau_{\text{eq}}, \lambda) = V_{\text{avail}}(\tau_{\text{eq}}, \lambda) \quad (4.13)$$

where V_{lig} is the volume required for a certain set of ligand molecules, and V_{avail} is the volume available to this set. First, one has to specify a relevant set of ligands

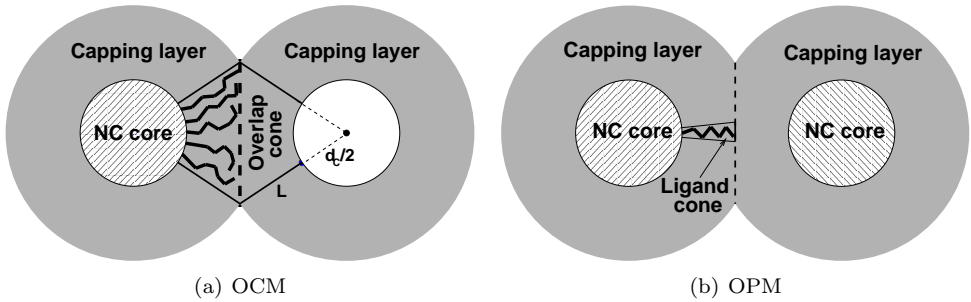


Figure 4.17: A sketch illustrating two ligand packing models. (a) The Overlap Cone Model (present work) defines the overlap cone first. It is then assumed that the ligands whose headgroups are adsorbed inside the overlap cone (represented by bold curved lines) lie completely inside the overlap cone. (b) The Optimal Packing Model (Ref.¹³²) assumes that each ligand (represented by the bold zigzag line) is confined into the ligand cone. The latter is a truncated cone limited by the ligand footprint on the NC core and the intersection plane dividing the two capping layers (represented by the dashed line in the figure), with the vertex in the corresponding core center.

and the volume to which they are confined. This task is highly non-trivial and not unambiguous. We will show in the sequel that this choice affects the prediction of a packing model, especially for $\lambda \geq 0.5$. Second, one has to formulate the two volumes in Eq. (4.13) as functions of τ and λ . This can be done either analytically or numerically. Finally, by solving Eq. (4.13) with respect to τ , we obtain $\tau_{\text{eq}}(\lambda)$.

We start with general considerations concerning V_{lig} . The number of ligand molecules on a metallic NC is limited by the repulsion between headgroups. Therefore, one introduces the *ligand footprint* A_0 which is the area on the NC surface occupied by one ligand. The volume V_1^0 of one single linear ligand is then $V_1^0 = LA_0$. In an ideal situation (denoted by 0), the total number of ligands N_{lig}^0 on a fully capped NC is the surface area of the NC sphere divided by the footprint:

$$N_{\text{lig}}^0 = \frac{\pi d_c^2}{A_0}. \quad (4.14)$$

The volume V_{lig}^0 of the ligands whose headgroups are adsorbed on a specific area A_{lig} is then given by

$$V_{\text{lig}}^0 = \frac{A_{\text{lig}}}{A_0} \times V_1^0 = A_{\text{lig}}L. \quad (4.15)$$

To adapt the model to more general systems, one has to introduce the density parameter ξ , which is the product of the relative grafting density and relative

ligand volume:

$$\xi = \frac{N_{\text{lig}}}{N_{\text{lig}}^0} \times \frac{V_1}{V_1^0}. \quad (4.16)$$

where N_{lig} is the actual number of capping molecules and V_1 is the actual ligand volume. Note that the inclusion of the parameter ξ is essential for branched ligands, as $\frac{V_1}{V_1^0} > 1$ in this case. The ligand volume V_{lig} is related to the ideal ligand volume V_{lig}^0 by

$$V_{\text{lig}} = \xi V_{\text{lig}}^0. \quad (4.17)$$

Fig. 4.1 shows the situation that ligands are relatively flexible, and that they are able to bend away from the “bottlenecks” between NC surfaces. The thiol headgroups, on the other hand, remain immobile as they are strongly adsorbed to the NC surface. We therefore propose the model sketched in Fig. 4.17(a). A pair of overlapping capping layers defines a circle in the intersection plane. By connecting this circle to each NC center, we obtain two *overlap cones* with volume V_{cone} each. Obviously, a part of each cone with volume $V_{\text{cone}}^{\text{core}}$ belongs to the corresponding NC core. The remaining volume $V_{\text{cone}} - V_{\text{cone}}^{\text{core}}$ is then available to capping molecules. The area of the NC surface inside each cone is denoted by $A_{\text{cone}}^{\text{core}}$. Our main assumption is that the ligands adsorbed on this surface lie inside an overlap cone. We will refer to this assumption as *Overlap Cone Model* (OCM). Equation (4.13) then becomes

$$V_{\text{lig}} = \xi A_{\text{cone}}^{\text{core}} L = V_{\text{cone}} - V_{\text{cone}}^{\text{core}} = V_{\text{avail}}. \quad (4.18)$$

It is important to note that both sides of this equation depend on the ligand length and the distance between NCs. Moreover, due to symmetry the OCM does not distinguish whether the ligand molecules belonging to one NC stay completely inside the corresponding cone or lie partly in the other cone.

For a pair of NCs with equal size, the three terms in Eq. (4.18) can be calculated using the formulae for solids of revolution:

$$\xi A_{\text{cone}}^{\text{core}} L = \frac{\pi d_c^3}{4} \lambda \xi \left(1 - \frac{\tau}{1 + \lambda} \right); \quad (4.19a)$$

$$V_{\text{cone}} = \frac{\pi d_c^3}{24} \tau \left((1 + \lambda)^2 - \tau^2 \right); \quad (4.19b)$$

$$V_{\text{cone}}^{\text{core}} = \frac{\pi d_c^3}{12} \left(1 - \frac{\tau}{1 + \lambda} \right). \quad (4.19c)$$

After dividing both sides by $\pi d_c^3/8$, Eq. (4.18) becomes

$$2\xi\lambda \left(1 - \frac{\tau}{1 + \lambda} \right) = \frac{1}{3}\tau \left((1 + \lambda)^2 - \tau^2 \right) - \frac{2}{3} + \frac{2}{3} \frac{\tau}{1 + \lambda}. \quad (4.20)$$

This is a cubic equation in τ , and it always has a trivial solution $\tau = 1 + \lambda$, i.e., when the two capping layers just touch each other. Indeed, in this case both

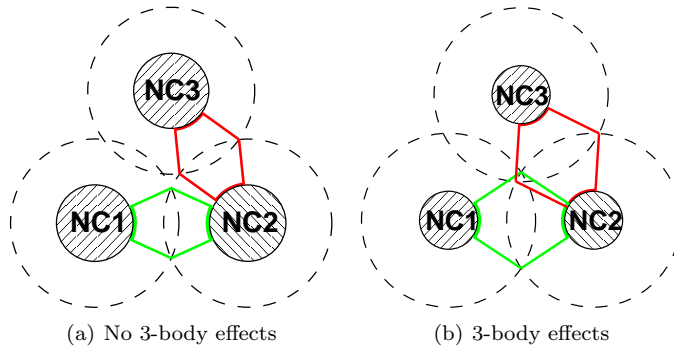


Figure 4.18: Three-body effects in the Overlap Cone Model. The three NCs are represented by shaded circles, their capping layers by the corresponding dashed circles. The overlap cones between NC1 and NC2 and between NC2 and NC3 are represented by light and dark lines respectively. In (a), these two overlap cones do not intersect, and they can be treated separately. In (b), the two overlap cones do intersect, so that both the intersection volume and the intersection NC surface area must be accounted for in Eq. (4.18). For clarity, the overlap cone between NC1 and NC3 as well as ligand molecules are not shown.

the cone volume V_{cone} and the corresponding surface A^{core} vanish. The relevant solution is

$$\tau_{\text{eq}} = -\frac{1+\lambda}{2} + \sqrt{\left(\frac{1+\lambda}{2}\right)^2 + \frac{6\xi\lambda+2}{1+\lambda}}, \quad (4.21)$$

while the third root of Eq. (4.20) is negative.

An important feature of the OCM is that it can account for many-body effects. When a capping layer of NC1 overlaps with capping layers of two other NCs, it may occur that the two overlap cones on NC1 intersect as in Fig. 4.18. In this case, some ligands on NC1 lie in two overlap cones simultaneously. Four-body effects arise in the same manner when four NCs are arranged in a tetrahedron. If one now wishes to express the volumes on both sides of Eq. (4.18) by combining expressions of Eq. (4.19), one has to subtract the double-counted intersection volume of the two cones on the right side, and the double-counted surface area on the left side of Eq. (4.20). Unlike the two-NC case, we were not able to calculate the corresponding integrals analytically. We have solved Eq. (4.18) numerically for a NC triplet arranged in an equilateral triangle, and for four NCs arranged in a regular tetrahedron. This numerical solution is shown in Fig. 4.19. The solution is identical to Eq. (4.21) for $\lambda \leq 0.39$, and then the aforementioned intersection of overlap cones occurs. For a tetrahedron, it is useful to consider the case when the ligands fill the whole space between NC cores (which holds for $\lambda \geq 0.54$). The

solution of Eq. (4.18) is then

$$\tau_{\text{eq}} = \sqrt[3]{\eta_{\text{tetr}}} \sqrt[3]{1 + 3\xi\lambda}, \quad (4.22)$$

where $\eta_{\text{tetr}} \approx 0.780$ is the atomic packing factor of a tetrahedron. Note that Eq. (4.22) is also a good (lower) approximation for τ_{eq} in the interval $0.39 < \lambda < 0.54$ with the maximum deviation from the exact solution being less than 0.01.

The Optimal Packing Model (OPM) of Landman and Luedtke¹³² makes different assumptions for the terms in Eq. (4.13). These authors consider a single ligand on the NC–NC line, and assume that it is confined to a truncated cone, as shown in Fig. 4.17(b). Per definition, such model does not account for many-body effects. In this situation, Eq. (4.13) becomes

$$V_{\text{lig}} = V_1 = \xi A_0 L = \frac{d_c}{6} A_0 (\tau^3 - 1) = V_{\text{avail}}. \quad (4.23)$$

The right part of this equation is the volume of the ligand cone (c.f. Fig. 4.17(b)). The only real solution of Eq. (4.23) is¹³²

$$\tau_{\text{eq}} = \sqrt[3]{1 + 3\xi\lambda}. \quad (4.24)$$

It should be noted that OPM reproduces very well experimental data on 3D-superlattices of capped Au NCs from Ref.⁶⁵ (for which it was developed). It is not clear, however, whether it is applicable to monolayers or small clusters of NCs. Coincidentally, Eq. (4.24) is identical to Eq. (4.22) with atomic packing factor of $\eta = 1$.

In Fig. 4.19, we plot our results from Sections 4.3 and 4.4 together with available experimental data on *monolayers* of capped gold and silver NCs, and we compare them to predictions of OCM and OPM. For both models, we consider the generic case $\xi = 1$. Both packing models predict equilibrium distances between NCs significantly smaller than $1 + \lambda$, implying a large interpenetration of capping layers. Consider first the 2-body OCM: τ_{eq} increases up to ≈ 1.25 until $\lambda \approx 0.75$ and then very slowly decreases. In particular, in the region $0.4 \leq \lambda \leq 1.5$ the value of τ_{eq} remains in the very narrow interval $1.2 < \tau < 1.25$. This explains the Golden Rule ($\tau \approx 1.25$) that we established in Section 4.3. The values of τ_{eq} predicted by the 3-body OCM become significantly higher than the ones predicted by the 2-body OCM for $\lambda > 0.65$, although they differ already for $\lambda > 0.39$. For a 3-body system, the OCM predicts a systematic increase of τ_{eq} up to $\lambda \approx 1.3$. The 4-body effects are even more pronounced.

The OCM reproduces both experimental and simulation data very well in the region $0.35 < \lambda < 0.6$. For $\lambda > 0.65$, the difference between 2-body and 3-body interactions becomes significant; this explains the discrepancies between our 2-body simulation results and experiments in this region. Apart from very small values of λ (Au₁₄₁₅SC2, Au₁₄₁₅SC3 and Au₅₆₁SC4), the OPM systematically overestimates the nearest-neighbor distance. The OPM also predicts a strong

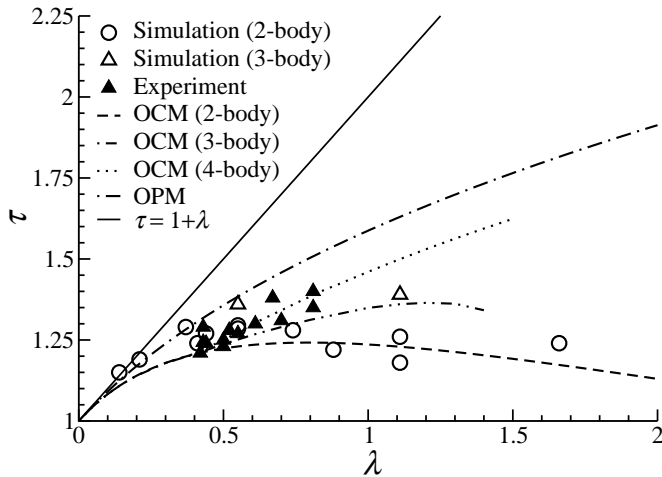


Figure 4.19: Scaled equilibrium distance τ versus scaled ligand length λ . Results of our 2-body (Section 4.3) and 3-body (Section 4.4) simulations together with experimental data from Refs.^{32,62,64,66,67,209,210,261} are compared with predictions of OCM (present work) and OPM (Ref.¹³²). The OCM data for two NCs were calculated using Eq. (4.21); the OCM data for three and four NCs were obtained by solving Eq. (4.18) numerically; the OPM data were calculated using Eq. (4.24). The distance $\tau = 1 + \lambda$ corresponds to the situation when the capping layers are in contact without overlapping.

monotonic increase of the equilibrium distance with ligand length, which was only found to be correct for 3D-structures.⁶⁵ However, the OPM provides no qualitative explanation for our numerical results on lower dimensional structures from Sections 4.3 and 4.4.

We now consider the dependence of τ_{eq} on the capping density ξ . In Section 4.3, we have shown that when the capping layer is partially degraded due to ligand evaporation ($\xi = 0.85$), then the effective interaction becomes even more attractive and the equilibrium distance shifts very close to the fusion distance τ_f . The latter is defined as the distance at which two NC cores touch each other; if the NC cores are not perfect spheres, τ_f is slightly larger than 1. For icosahedral NCs, $\tau_f \approx 1.1$. We considered the systems $\text{Au}_{147}\text{SC4}$ ($\lambda = 0.56$) and $\text{Au}_{561}\text{SC4}$ ($\lambda = 0.37$). The OCM yields for $\xi = 0.85$ the equilibrium distances in these systems $\tau_{\text{eq}} = 1.15$ and $\tau_{\text{eq}} = 1.13$, respectively; both alarmingly close to τ_f , in very good qualitative agreement with our simulation results. The estimates from the OPM (1.25 and 1.34), on the other hand, do not point to possible NC sintering.

In summary, the OCM quantitatively reproduces simulation and experimental data in the region $0.35 < \lambda < 0.6$; and it explains why the equilibrium distance in

a NC dimer is almost ligand length independent over a large range of λ . Moreover, the OCM explains the split between 2-body simulation results and experiments for $\lambda > 0.65$. In a few rare cases that involve a very short ligand, the OPM reproduces the observations quantitatively better than the OCM.

4.5.1 Implications for ligand design

We aim to combine the results of Sections 4.3, 4.4 and 4.5 with regard to ligand design for potential applications. Although the OCM is a purely geometric model, its results can be interpreted in terms of many-body interactions. We have seen in Section 4.4 that the shift of the equilibrium distance in a 3-NC system compared to a 2-NC case correlates with the strength of the repulsive three-body interaction. Thus, we can consider the difference between the 2-NC and 3-NC or 4-NC OCM predictions as a qualitative measure for an energetic penalty associated with formation of 2D or 3D structures, respectively. This loss should of course be compared to the energetic gain due to a large number of contacts between NCs. Fig. 4.15 shows that for long capping molecules the penalty may even overbalance the gain, so that self-assembly in 1D-structures becomes energetically preferred over 2D close-packed ones, as found experimentally.⁶³ In this section, we consider monodisperse NCs with $\xi = 1$ (linear ligands, full capping) capped by a surfactant with scaled length λ . To give also a concrete example, we will write in brackets the corresponding range of alkylthiol ligands for a NC with $d_c = 5$ nm.

First, consider short ligands $\lambda \leq 0.39$ (SC8 and shorter). The OCM predicts then the same equilibrium distance τ_{eq} (Eq. (4.21)) in 1D, 2D and 3D assemblies, and thus no significant many-body effects are present. In this range, the NC superstructures with maximum coordination are very stable energetically, and the Golden Rule applies. Superlattices may readily precipitate from NC dispersions even without solvent evaporation. These superlattices are expected to form via the classical nucleation and growth mechanisms.

Next, consider ligands with intermediate length $0.39 < \lambda \leq 0.65$ (SC9–SC12). In this regime, the OCM equilibrium distances between NCs in 1D and 2D aggregates are similar, while the spacing in 3D NC aggregates is predicted to be larger and to increase systematically with ligand length. In particular, for $\lambda > 0.54$ (SC11 and longer), the entire space between NC cores is filled by ligand chains and NC–NC spacing τ_{eq} in 3D-structures is predicted according to Eq. (4.22) with the suitable space filling factor η . The large difference between 2D and 3D allows us to estimate small to moderate three-NC interactions and large repulsive four-NC forces in this range of λ . Thus, the Golden Rule applies only to monolayers in this case, and they are energetically very stable.³² Due to the repulsive four-body interactions, the nucleation of 3D-superlattices is expected to be hindered in one direction, and their formation is predicted to occur via a layer-by-layer assembly. This may lead to a lattice distortion perpendicular to the substrate.

Finally, consider long ligands $0.65 < \lambda < 1.5$ (SC12–SC30). In this case,

the dependence of τ_{eq} on λ in 1D and 2D structures is non-monotonic. In 1D-structures, the Golden Rule $\tau_{\text{eq}} \approx 1.25$ is still obeyed. In 2D-structures, on the other hand, the spacing between NCs is larger; in particular, the values of τ_{eq} remain in the interval $1.3 \leq \tau \leq 1.35$ over a relatively broad range of ligand lengths $0.8 \leq \lambda \leq 1.5$ (SC16–SC30). This implies strong repulsive three-body interactions; as we have shown in Section 4.4, open 1D aggregates of NCs may even become energetically more favourable than 2D closed packed structures in this range of λ . This effect will inevitably introduce strain in NC superlattices, making the self-assembly into close-packed structures less favourable than more open and less ordered ones.⁶³

We conclude that the capping molecules with $\lambda \leq 0.39$ are particularly suitable for formation of stable, robust 3D structures. Ligands with intermediate length $0.39 < \lambda \leq 0.65$ are suited for creating stable close-packed monolayers. Long ligands can be used for spontaneous formation of open 1D structures like chains, rings or foams.

4.6 Effective interaction in a good solvent

We compute the potential of mean force between two $\text{Au}_{147}(\text{SC4})_{58}$ clusters in hexane solution, which is a widely used solvent in experiments. The number of solvent molecules is determined from a grand-canonical MC simulation (see Chapter 2 of the present thesis). The box size for the PMF computation is $80 \times 80 \times 120 \text{ \AA}^3$ with the NCs placed along the direction corresponding to the longest box-length. In this way we minimize the possible influence of periodic images of NCs. The PMF is shown in Fig. 4.20(a) and it features a steep short-range repulsion ranging roughly until the point where the capping layers detach ($r_d \approx 27 \text{ \AA}$). This repulsion is well approximated by the exponential function

$$\phi(r) = k_B T \exp[-\gamma(r - r_d)], \quad \text{with } \gamma = 0.55 \text{ \AA}^{-1}. \quad (4.25)$$

Beyond the interpenetration point, the PMF is positive with values below $1 k_B T$. The repulsive nature of the potential is a result of the well-known good solvent effect that we already observed in Section 2.5. The loss of solvent-solvent and solvent-surfactant interactions compensates for the attractive interactions between capping molecules.¹⁵⁹ What remains is entropic repulsion between capping molecules, and, to a small extent, depletion effects of the solvent. The form of the potential is very similar to the one suggested in Ref.²⁶³ for alkylthiol capped silver NCs in solution: $\phi(r) \propto \frac{d_c}{r-d_c} \exp[-\gamma r]$. In Ref.,¹³⁹ the PMF between much smaller capped Au–NCs in supercritical ethane has been calculated as a function of solvent density. It has been shown that with increasing density (solvent quality) the interaction turned from attractive to purely repulsive.

The structure of the solvent is described by the segment density shown in Fig. 4.20(b). The two black half-disks correspond to the NC cores. The almost white zones bordering those half-disks stem from the capping layers, which are

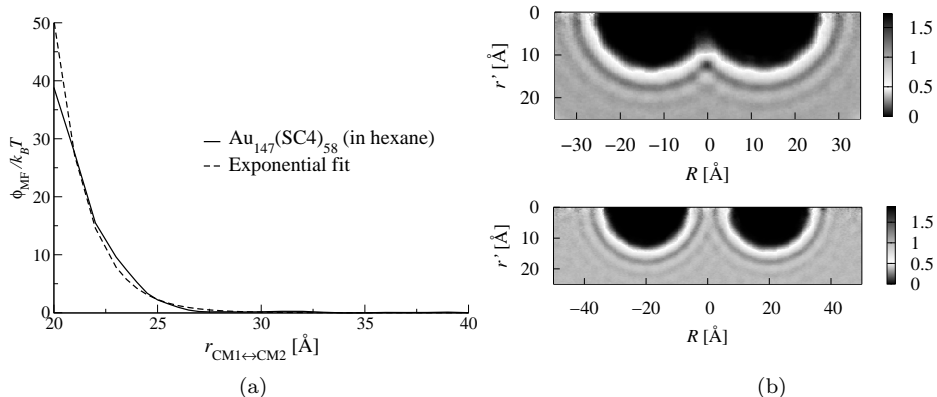


Figure 4.20: (a) Potential of mean force ϕ_{MF} as a function of center of mass separation r between two Au_{147} nanocrystals capped 58 SC4 molecules in explicit solvent (3440 n-hexane molecules). (b) Segment density map of hexane around a pair of $\text{Au}_{147}(\text{SC4})_{58}$ clusters constraint at $r = 25 \text{\AA}$ (top) and $r = 40 \text{\AA}$ (bottom). The horizontal axis R represents the line connecting the NC centers, the vertical axis r' represents the perpendicular direction. The density is averaged over the surface of the cylinder with the axis along R and radius r' ; and it is normalized by the density of bulk hexane.

interpenetrated by few solvent molecules. The two dark and one light ring around the NCs can be identified as the first and the second solvation shell with a depletion zone between them. At larger separations between NCs ($r = 40 \text{\AA}$), the first solvation shell remains intact. Strong interference occurs at closer distances ($r = 25 \text{\AA}$).

4.7 Conclusions

In summary, we have computed and parameterized the potential of mean force between alkylthiol capped gold nanocrystals using atomistic simulations. Constrained MD and MC are the methods of choice, and we have shown that unconstrained methods are impeded by the extremely slow capping layer reconstruction. The potential well-depth is of the order of tens to hundreds $k_B T$. The minimum of the two-body PMF lies at $\approx 1.25d_c$, suggesting a strong thermodynamic stability of NC structures with the ratio τ between the center-to-center distance and core diameter close to this value. The interaction becomes less attractive with increasing temperature without a significant increase of the equilibrium distance. NC superstructures with overlapping capping layers feature a shape memory. Sintering of NC cores can be promoted by incomplete capping layers. In a good solvent,

the PMF is purely repulsive, and the potential can be approximated by an exponential function.

We have also investigated three-body effects on interactions between capped NCs in vacuum. If the capping layers of three NCs overlap pairwise, a repulsive 3-body interaction is always present. Due to this interaction, the equilibrium distance in the two systems we studied shifted to $\approx 1.36d_c$. The contribution of three-body effects to the total interaction energy is 20% for a short ligand, and 40% for a long one. In the latter case, one-dimensional (rings or chains) or fractal aggregates of capped NCs at the air-water interface are energetically more favourable than two-dimensional ones (islands or close-packed monolayers). We have introduced the Overlap Cone Model to explain our findings. This model considers the equilibrium distance between capped NCs as effective packing of flexible alkylthiol ligand tails. The OCM agrees well with our simulation results as well as with available experimental data on monolayers of capped NCs. We conclude that packing of ligands determines the spacing between NCs in aggregates; and interactions between capping layers play a crucial role in thermodynamic behaviour and self-assembly of capped NCs.

Abbreviations

CBMC	Configurational-bias Monte Carlo
CG	Coarse-grained
DFT	Density Functional Theory
Eq.	Equation
Fig.	Figure
GCMC	Grand-canonical Monte Carlo
HK	Hautman-Klein (potential)
(HR) TEM	(High-resolution) transmission electron microscopy
Ih	Icosahedron
LJ	Lennard-Jones (potential)
MC	Monte Carlo
MD	Molecular dynamics
μVT	Grand-canonical ensemble
NC	Nanocrystal
NVT	Canonical ensemble
OCM	Overlap Cone Model
OPM	Optimal Packing Model
PL	Photoluminescence
PMF	Potential of mean force
QD	Quantum dot

QY Quantum yield

RDF Radial distribution function

Ref. Reference

RW Random walk

SAM Self-assembled monolayer

SMD Steered Molecular Dynamics

UHV Ultra-high vacuum

vdW van der Waals (interactions)

VV Velocity-Verlet (algorithm)

Bibliography

1. Arico, A.; Bruce, P.; Scrosati, B.; Tarascon, J.; Van Schalkwijk, W. *Nature Mater.* **2005**, *4*, 366-377.
2. Wang, J. *Electroanalysis* **2005**, *17*, 7-14.
3. Moriarty, P. *Rep. Prog. Phys.* **2001**, *64*, 297-381.
4. West, J.; Halas, N. *Annu. Rev. Biomed. Eng.* **2003**, *5*, 285-292.
5. Rodriguez-Hernandez, J.; Checot, F.; Gnanou, Y.; Lecommandoux, S. *Prog. Polym. Sci.* **2005**, *30*, 691-724.
6. Rose, H. H. *Sci. Technol. Adv. Mater.* **2008**, *9*, 014107.
7. Lifshitz, E.; Bashouti, M.; Kloper, V.; Kigel, A.; Eisen, M. S.; Berger, S. *Nano Lett.* **2003**, *3*, 857-862.
8. Martin, C. *Science* **1994**, *266*, 1961-1966.
9. Zhang, S. *Nat. Biotechnol.* **2003**, *21*, 1171-1178.
10. Martin, C. *Chem. Mater.* **1996**, *8*, 1739-1746.
11. Patzke, G.; Krumeich, F.; Nesper, R. *Angew. Chem. Int. Edit.* **2002**, *41*, 2446-2461.
12. Zhou, Y.; Wang, C.; Zhu, Y.; Chen, Z. *Chem. Mater.* **1999**, *11*, 2310.
13. Manna, L.; Scher, E. C.; Alivisatos, A. P. *J. Am. Chem. Soc.* **2000**, *122*, 12700-12706.
14. Duan, X.; Lieber, C. *Adv. Mater.* **2000**, *12*, 298-302.
15. Skrabalak, S. E.; Xia, Y. *ACS Nano* **2009**, *3*, 10-15.
16. Huczko, A. *Appl. Phys. A-Mater. Sci. Process.* **2000**, *70*, 365-376.
17. Wade, T. L.; Wegrowe, J. E. *Eur. Phys. J. - Appl. Phys* **2005**, *29*, 3-22.
18. Xu, X. D.; Wang, Y. C.; Liu, Z. F. *J. Cryst. Growth* **2005**, *285*, 372-379.
19. Jayasinghe, S. N. *Physica E* **2008**, *40*, 2911-2915.
20. Moore, G. E. *Electronics* **1965**, *38*, 82.
21. Alivisatos, A. P. *Science* **1996**, *271*, 933-937.
22. Yu, D.; Wang, C.; Guyot-Sionnest, P. *Science* **2003**, *300*, 1277-1280.
23. Remacle, F.; Beverly, K.; Heath, J.; Levine, R. *J. Phys. Chem. B* **2003**, *107*, 13892-13901.
24. Klein, D. L.; Roth, R.; Lim, A. K. L.; Alivisatos, A. P.; McEuen, P. L. *Nature* **1997**, *389*, 699-701.
25. Amlani, I.; Orlov, A.; Toth, G.; Bernstein, G.; Lent, C.; Snider, G. *Science* **1999**, *284*, 289-291.
26. Jain, P. K.; Huang, X.; El-Sayed, I. H.; El-Sayed, M. A. *Acc. Chem. Res.* **2008**, *41*, 1578-1586.

27. Hutchings, G. J.; Brust, M.; Schmidbaur, H. *Chem. Soc. Rev.* **2008**, *37*, 1759-1765.
28. Ghosh, S. K.; Pal, T. *Chem. Rev.* **2007**, *107*, 4797-4862.
29. Ghenciu, A. F. *Curr. Opin. Solid State Mat. Sci.* **2002**, *6*, 389-399.
30. Antolini, E. *J. Mater. Sci.* **2003**, *38*, 2995-3005.
31. Chan, K.-Y.; Ding, J.; Ren, J.; Cheng, S.; Tsang, K. Y. *J. Mater. Chem.* **2004**, *14*, 505-516.
32. Mueggenburg, K. E.; Lin, X.-M.; Goldsmith, R. H.; Jaeger, H. M. *Nat. Mater.* **2007**, *6*, 656-660.
33. Xia, H.; Wang, D. *Adv. Mater.* **2008**, *20*, 4253-4256.
34. Cheng, W.; Campolongo, M. J.; Cha, J. J.; Tan, S. J.; Umbach, C. C.; Muller, D. A.; Luo, D. *Nature Mater.* **2009**, *8*, 519-525.
35. Murray, C.; Sun, S.; Gaschler, W.; Doyle, H.; Betley, T.; Kagan, C. *IBM J. Res. & Dev.* **2001**, *45*, 47-56.
36. Jun, Y.-W.; Seo, J.-W.; Sang, J. O.; Cheon, J. *Coord. Chem. Rev.* **2005**, *249*, 1766-1775.
37. Kwon, S. G.; Hyeon, T. *Acc. Chem. Res.* **2008**, *41*, 1696-1709.
38. Brust, M.; Bethell, D.; Schiffrin, D. J.; Whyman, R. *J. Chem. Soc. Chem. Commun.* **1994**, 801-802.
39. Leff, D.; Brandt, L.; Heath, J. *Langmuir* **1996**, *12*, 4723-4730.
40. Hostetler, M.; Green, S.; Stokes, J.; Murray, R. *J. Am. Chem. Soc.* **1996**, *118*, 4212-4213.
41. Chen, S.; Kimura, K. *Langmuir* **1999**, *15*, 1075-1082.
42. Weare, W.; Reed, S.; Warner, M.; Hutchison, J. *J. Am. Chem. Soc.* **2000**, *122*, 12890-12891.
43. Stoeva, S.; Klabunde, K.; Sorensen, C.; Dragieva, I. *J. Am. Chem. Soc.* **2002**, *124*, 2305-2311.
44. Kim, Y.; Oh, S.; Crooks, R. *Chem. Mater.* **2004**, *16*, 167-172.
45. Hiramatsu, H.; Osterloh, F. *Chem. Mater.* **2004**, *16*, 2509-2511.
46. Sellers, H.; Ulman, A.; Shnidman, Y.; Eilers, J. E. *J. Am. Chem. Soc.* **1993**, *115*, 9389-9401.
47. Hostetler, M. J.; Wingate, J. E.; Zhong, C.; Harris, J. E.; Vachet, R. W.; Clark, M. R.; Londono, J. D.; Green, S. J.; Stokes, J. J.; Wignall, G. D.; Glish, G. L.; Porter, M. D.; Evans, N. D.; Murray, R. W. *Langmuir* **1998**, *14*, 17-30.
48. Fink, J.; Kiely, C. J.; Bethel, D.; Schiffrin, D. J. *Chem. Mater.* **1998**, *10*, 922-926.
49. Kiely, C. J.; Fink, J.; Brust, M.; Bethel, D.; Schiffrin, D. J. *Nature* **1998**, *396*, 444-446.
50. Murray, C. B.; Norris, D. J.; Bawendi, M. G. *J. Am. Chem. Soc.* **1993**, *115*, 8706-8715.
51. Talapin, D. V.; Rogach, A. L.; Kornowski, A.; Haase, M.; Weller, H. *Nano Lett.* **2001**, *1*, 207-211.
52. de Mello Donegà, C.; Hickey, S. G.; Wuister, S. F.; Vanmaekelbergh, D.; Meijerink, A. *J. Phys. Chem. B* **2003**, *107*, 489-496.
53. Liu, H.; Owen, J. S.; Alivisatos, A. P. *J. Am. Chem. Soc.* **2007**, *129*, 305-312.
54. Owen, J. S.; Park, J.; Trudeau, P.-E.; Alivisatos, A. P. *J. Am. Chem. Soc.* **2008**, *130*, 12279-12281.
55. Houtepen, A.; Koole, R.; Vanmaekelbergh, D.; Meeldijk, J.; Hickey, S. *J. Am. Chem. Soc.* **2006**, *128*, 6792-6793.
56. Wang, F.; Tang, R.; Buhro, W. E. *Nano Lett.* **2008**, *8*, 3521-3524.

57. Belman, N.; Israelachvili, J. N.; Li, Y.; Safinya, C. R.; Bernstein, J.; Golan, Y. *Nano Lett.* **2009**, *9*, 2088-2093.
58. Faraday, M. *Philos. Trans. R. Soc. London* **1857**, 145.
59. Alexander, A. E.; P., J. *Colloid Science*; Oxford University Press: London, United Kingdom, second ed.; 1950.
60. K. S. Birdi (editor in chief), *Handbook of Surface and Colloid Chemistry*; CRC press: Boca Raton, USA, third ed.; 2008.
61. Murray, C.; Kagan, C.; Bawendi, M. *Science* **1995**, *270*, 1335-1338.
62. Andres, R. P.; Bielefeld, J. D.; Henderson, J. I.; Janes, D. B.; Kolagunta, V. R.; Kubiak, C. P.; Mahoney, W. J.; Osifchin, R. G. *Science* **1996**, *273*, 1690-1693.
63. Heath, J. R.; Knobler, C. M.; Leff, D. V. *J. Phys. Chem. B* **1997**, *101*, 189-197.
64. Korgel, B. A.; Fitzmaurice, D. J. *Phys. Rev. Lett.* **1998**, *80*, 3531-3534.
65. Whetten, R. L.; Shafiqullin, M. N.; Khoury, J. T.; Schaaff, T. G.; Vezmar, I.; Alvarez, M. M.; Wilkinson, A. *Acc. Chem. Res.* **1999**, *32*, 397-406.
66. Pileni, M. P. *J. Phys. Chem. B* **2001**, *105*, 3358-3371.
67. Lin, X. M.; Jaeger, H. M.; Sorensen, C. M.; Klabunde, K. J. *J. Phys. Chem. B* **2001**, *105*, 3353-3357.
68. Shevchenko, E.; Talapin, D.; Kotov, N.; O'Brien, S.; Murray, C. *Nature* **2006**, *439*, 55-59.
69. Urban, J.; Talapin, D.; Shevchenko, E.; Kagan, C.; Murray, C. *Nature Mater.* **2007**, *6*, 115-121.
70. Chen, Z.; O'Brien, S. *ACS Nano* **2008**, *2*, 1219-1229.
71. Overgaag, K.; Evers, W.; de Nijs, B.; Koole, R.; Meeldijk, J.; Vanmaekelbergh, D. *J. Am. Chem. Soc.* **2008**, *130*, 7833-7835.
72. Pileni, M. P. *Acc. Chem. Res.* **2008**, *41*, 1799-1809.
73. Tao, A. R.; Huang, J.; Yang, P. *Acc. Chem. Res.* **2008**, *41*, 1662-1673.
74. Markovich, G.; Collier, C. P.; Heath, J. R. *Phys. Rev. Lett.* **1998**, *80*, 3807-3810.
75. Liljeroth, P.; Vanmaekelbergh, D.; Ruiz, V.; Kontturi, K.; Jiang, H.; Kauppinen, E.; Quinn, B. *J. Am. Chem. Soc.* **2004**, *126*, 7126-7132.
76. Fried, T.; Shemer, G.; Markovich, G. *Adv. Mater.* **2001**, *13*, 1158.
77. Terris, B. D.; Thomson, T. *J. Phys. D - Appl. Phys.* **2005**, *38*, R199-R222.
78. Sun, S. *Adv. Mater.* **2006**, *18*, 393-403.
79. Heath, J. *Nature* **2007**, *445*, 492-493.
80. Alder, B. J.; Wainwright, T. E. *J. Chem. Phys.* **1957**, *27*, 1208-1209.
81. Pusey, P. N.; Van Megen, W. *Nature* **1986**, *320*, 340-342.
82. Eldridge, M. D.; Madden, P. A.; Frenkel, D. *Nature* **1993**, *365*, 35-37.
83. Eldridge, M. D.; Madden, P. A.; Frenkel, D. *Mol. Phys.* **1993**, *80*, 987-995.
84. Pusey, P. N.; Poon, W. C. K.; Ilett, S. M.; Bartlett, P. *J. Phys. - Condes. Matter* **1994**, *6*, A29-A36.
85. Frenkel, D.; Smit, B. *Understanding Molecular Simulations*; Academic Press: San Diego, USA, second ed.; 2002.
86. Leunissen, M. E.; Christova, C. G.; Hynninen, A.-P.; Royall, C. P.; Campbell, A. I.; Imhof, A.; Dijkstra, M.; van Roij, R.; van Blaaderen, A. *Nature* **2005**, *437*, 235-240.

87. Hynninen, A. P.; Thijssen, J. H. J.; Vermolen, E. C. M.; Dijkstra, M.; van Blaaderen, A. *Nature Mater.* **2007**, *6*, 202-205.
88. Hamaker, H. C. *Physica* **1937**, *4*, 1058-1072.
89. Verwey, E. J. W.; Overbeek, J. T. G. *Theory of the Stability of Lyophobic Colloids*; Elsevier: Amsterdam, 1948.
90. Atkins, P.; de Paula, J. *Physical Chemistry*; Oxford University Press: New York, USA, eighth ed.; 2006.
91. Wesseling, P. *Principles of Computational Fluid Dynamics*; Springer Verlag: New York, first ed.; 2000.
92. Koch, W.; Holthausen, M. C. *A Chemist's Guide to Density Functional Theory*; Wiley-VCH: Weinheim, 2000.
93. Helgaker, T.; Klopper, W.; Tew, D. P. *Mol. Phys.* **2008**, *106*, 2107-2143.
94. Vlugt, T. J. H.; Malek, K.; Smit, B. Molecular simulation techniques using classical force fields. In *Computational Methods in Catalysis and Materials Science*; Sautet, P.; van Santen, R. A., Eds.; Wiley-VCH: Weinheim, 2009.
95. Forester, T. R.; Smith, W. "DL-POLY User Manual", 1995.
96. Allinger, N. L.; Yuh, Y. H.; Lii, J.-H. *J. Am. Chem. Soc.* **1989**, *111*, 8551-8566.
97. Martin, M. G.; Siepmann, J. I. *J. Phys. Chem. B* **1998**, *102*, 2569-2577.
98. Dubbeldam, D.; Calero, S.; Vlugt, T. J. H.; Krishna, R.; Maesen, T. L. M.; Smit, B. *J. Phys. Chem. B* **2004**, *108*, 12301-12313.
99. Field, M. J. *A Practical Introduction To The Simulation Of Molecular Systems*; Cambridge University Press: Cambridge, second ed.; 2007.
100. Mackerell Jr., A. D. *J. Comput. Chem.* **2004**, *25*, 1584-1604.
101. Chen, J.; Brooks III, C. L.; Khandogin, J. *Curr. Opin. Struc. Biol.* **2008**, *18*, 140-148.
102. Guvench, O.; MacKerell Jr., A. D. **2008**, *443*, 63-88.
103. Ryckaert, J.; McDonald, I.; Klein, M. *Mol. Phys.* **1989**, *67*, 957-979.
104. Polson, J.; Frenkel, D. *J. Chem. Phys.* **1999**, *111*, 1501-1510.
105. Khalili-Araghi, F.; Gumbart, J.; Wen, P.-C.; Sotomayor, M.; Tajkhorshid, E.; Schulten, K. *Curr. Opin. Struc. Biol.* **2009**, *19*, 128-137.
106. Vlugt, T. J. H.; van der Eerden, J. P. J. M.; Dijkstra, M.; Smit, B.; Frenkel, D. *Introduction to Molecular Simulation and Statistical Thermodynamics*; : Delft, The Netherlands, 2008 available from <http://www.phys.uu.nl/~vlugt/imsst>.
107. Paul, W.; Binder, K.; Kremer, K.; Heermann, D. W. *Macromolecules* **1991**, *24*, 6332-6334.
108. Tschop, W.; Kremer, K.; Batoulis, J.; Burger, T.; Hahn, O. *Acta Polymerica* **1998**, *49*, 61-74.
109. Klein, M. L.; Shinoda, W. *Science* **2008**, *321*, 798-800.
110. Marrink, S. J.; Risselada, H. J.; Yefimov, S.; Tieleman, D. P.; de Vries, A. H. *J. Phys. Chem. B* **2007**, *111*, 7812-7824.
111. Monticelli, L.; Kandasamy, S. K.; Periole, X.; Larson, R. G.; Tieleman, D. P.; Marrink, S.-J. *J. Chem. Theory Comput.* **2008**, *4*, 819-834.
112. Derjaguin, B.; Landau, L. *Acta Physico Chemica URSS* **1941**, *14*, 633.
113. Schneider, T.; Stoll, E. *Phys. Rev. B* **1978**, *17*, 1302-1322.
114. Ermak, D. L. *J. Chem. Phys.* **1975**, *62*, 4189-4196.

115. Hoogerbrugge, P.; Koelman, J. *Europhys. Lett.* **1992**, *19*, 155-160.
116. Koelman, J.; Hoogerbrugge, P. *Europhys. Lett.* **1993**, *21*, 363-368.
117. Landau, D. P.; Binder, K. *A Guide to Monte Carlo Simulations in Statistical Physics*; Cambridge University Press: Cambridge, UK, first ed.; 2000.
118. Vlugt-Wensink, K. D. F.; Vlugt, T. J. H.; Jiskoot, W.; Crommelin, D. J. A.; Verrijck, R.; Hennink, W. E. *J. Control. Release* **2006**, *111*, 117-127.
119. Smit, B., *J. Chem. Phys.* **1992**, *96*, 8639-8640.
120. Adhikari, N. P.; Peng, X. H.; Alizadeh, A.; Ganti, S.; Nayak, S. K.; Kumar, S. K. *Phys. Rev. Lett.* **2004**, *93*,.
121. Israelachvili, J. N. *Intermolecular and Surface Forces*; Academic Press: London, United Kingdom, second ed.; 1992.
122. Schapotschnikow, P.; Pool, R.; Vlugt, T. J. H. *Nano Lett.* **2008**, *8*, 2930-2934.
123. Cleveland, C. L.; Luedtke, W. D.; Landman, U. *Phys. Rev. Lett.* **1998**, *81*, 2036-2039.
124. Cleveland, C. L.; Luedtke, W. D.; Landman, U. *Phys. Rev. B* **1999**, *60*, 5065-5077.
125. Wang, Y.; Teitel, S.; Dellago, C. *Chem. Phys. Lett.* **2004**, *394*, 257-261.
126. Chui, Y. H.; Grochola, G.; Snook, I. K.; Russo, S. P. *Phys. Rev. B* **2007**, *75*, 033404.
127. Grünwald, M.; Rabani, E.; Dellago, C. *Phys. Rev. Lett.* **2006**, *96*, 255701.
128. Morgan, B. J.; Madden, P. A. *J. Phys. Chem. C* **2007**, *111*, 6724-6731.
129. Grünwald, M.; Dellago, C. *Nano Lett.* **2009**, *9*, 2099-2102.
130. Luedtke, W. D.; Landman, U. *J. Phys. Chem. B* **1996**, *100*, 13323-13329.
131. Luedtke, W. D.; Landman, U. *J. Phys. Chem. B* **1998**, *102*, 6566-6572.
132. Landman, U.; Luedtke, W. D. *Faraday Discuss.* **2004**, *125*, 1-22.
133. Tay, K.; Bresme, F. *Mol. Sim.* **2005**, *31*, 515-526.
134. Henry, A.-I.; Courty, A.; Pileni, M.-P.; Albouy, P.-A.; Israelachvili, J. *Nano Lett.* **2008**, *8*, 2000-2005.
135. Badia, A.; Gao, W.; Singh, V.; Demers, L.; Cuccia, L.; Reven, L. *Langmuir* **1996**, *12*, 1262-1269.
136. Badia, A.; Lennox, B.; Reven, L. *Acc. Chem. Res.* **2000**, *33*, 475-481.
137. Lal, M.; Plummer, M.; Richmond, N. J.; Smith, W. *J. Phys. Chem. B* **2004**, *108*, 6052-6061.
138. Henz, B. J.; Hawa, T.; Zachariah, M. R. *Langmuir* **2008**, *24*, 773-783.
139. Patel, N.; Egorov, S. A. *J. Chem. Phys.* **2007**, *126*, 054706.
140. Sear, R.; Chung, S.-M.; Markovich, G.; Gelbart, W.; Heath, J. *Phys. Rev. E* **1999**, *59*, R6255-R6258.
141. Wang, J.-C.; Neogi, P.; Forciniti, D. *J. Chem. Phys.* **2006**, *125*,.
142. Khan, S. J.; Pierce, F.; Sorensen, C. M.; Chakrabarti, A. *Langmuir* **2009**, *25*, 13861-13868.
143. de Gennes, P. G. *Adv. Colloid Interface Sci.* **1987**, *27*, 189-209.
144. Talapin, D. V.; Shevchenko, E. V.; Murray, C. B.; Titov, A. V.; Král, P. *Nano Lett.* **2007**, *7*, 1213-1219.
145. Rabani, E.; Reichman, D. R.; Geissler, P. L.; Brus, L. E. *Nature* **2003**, *426*, 271-274.
146. Sztrum, C. G.; Hod, O.; Rabani, E. *J. Phys. Chem. B* **2005**, *109*, 6741-6747.

147. Allen, M. P.; Tildesley, D. J. *Computer Simulation of Liquids*; Oxford University Press: Oxford, United Kingdom, first ed.; 1987.
148. Rapaport, D. C. *The Art of Molecular Dynamics Simulation*; Cambridge University Press: Cambridge, UK, second ed.; 2004.
149. Vlugt, T. J. H.; Martin, M. G.; Smit, B.; Siepmann, J. I.; Krishna, R. *Mol. Phys.* **1998**, *94*, 727-733.
150. Chandler, D., *Introduction to Modern Statistical Mechanics*; Oxford University Press: New York, USA, first ed.; 1987.
151. Manousiouthakis, V. I.; Deem, M. W. *J. Chem. Phys.* **1999**, *110*, 2753-2756.
152. Metropolis, N.; Rosenbluth, A. W.; Rosenbluth, M. N.; Teller, A. H.; Teller, E. *J. Chem. Phys.* **1953**, *21*, 1087-1092.
153. Siepmann, J. I.; Frenkel, D. *Mol. Phys.* **1992**, *75*, 59-70.
154. Frenkel, D.; Mooij, G. C. A. M.; Smit, B. *J. Phys.: Condens. Matter* **1992**, *4*, 3053-3076.
155. de Pablo, J. J.; Laso, M.; Suter, U. W. *J. Chem. Phys.* **1992**, *96*, 6157-6162.
156. Siepmann, J. I. Configurational-bias Monte Carlo: Background and Selected Applications. In *Computer simulation of biomolecular systems: theoretical and experimental applications*; Gunsteren, W. v.; Weiner, P.; Wilkinson, A., Eds.; Escom Science Publisher: Leiden, 1993.
157. Macedonia, M.; Maginn, E. *Mol. Phys.* **1999**, *96*, 1375 - 1390.
158. Shevade, A.; Zhou, J.; Zin, M.; Jiang, S. *Langmuir* **2001**, *17*, 7566-7572.
159. Pool, R.; Schapotschnikow, P.; Vlugt, T. J. H. *J. Phys. Chem. C* **2007**, *111*, 10201-10212.
160. Vlugt, T. J. H.; Krishna, R.; Smit, B. *J. Phys. Chem. B* **1999**, *103*, 1102-1118.
161. Martin, M. G.; Siepmann, J. I. *J. Phys. Chem. B* **1999**, *103*, 4508-4517.
162. Consta, S.; Wilding, N. B.; Frenkel, D.; Alexandrowicz, Z. *J. Chem. Phys.* **1999**, *110*, 3220-3228.
163. Consta, S.; Vlugt, T. J. H.; Hoeth, J. W.; Smit, B.; Frenkel, D. *Mol. Phys.* **1999**, *97*, 1243-1254.
164. Combe, N.; Vlugt, T. J. H.; Wolde, P. R. T.; Frenkel, D. *Mol. Phys.* **2003**, *101*, 1675-1682.
165. Mavrantzas, V. G.; Boone, T. D.; Zervopoulou, E.; Theodorou, D. N. *Macromolecules* **1999**, *32*, 5072-5096.
166. Kofke, D.; Glandt, E. *Mol. Phys.* **1988**, *64*, 1105-1131.
167. Swope, W. C.; Andersen, H. C.; Berens, P. H.; Wilson, K. R. *J. Chem. Phys.* **1982**, *76*, 637-649.
168. Ryckaert, J.-P.; Ciccotti, G.; Berendsen, H. J. C. *J. Comput. Phys.* **1977**, *23*, 327-341.
169. Andersen, H. C. *J. Comput. Phys.* **1983**, *52*, 24-34.
170. Miller, T.; Eleftheriou, M.; Pattnaik, P.; Ndrigano, A.; Newns, D.; Martyna, G. J. *Chem. Phys.* **2002**, *116*, 8649.
171. Ulman, A., *Chem. Rev.* **1996**, *96*, 1533-1554.
172. Schreiber, F., *Prog. Surf. Sci.* **2000**, *65*, 151-256.
173. Zhang, L.; Goddard, W.; Jiang, S. *J. Chem. Phys.* **2002**, *117*, 7342 - 7349.
174. Nuzzo, R. G.; Zegarski, B. R.; Dubois, L. H. *J. Am. Chem. Soc.* **1987**, *109*, 733-740.
175. Grönbeck, H.; Curioni, A.; Andreoni, W. *J. Am. Chem. Soc.* **2000**, *122*, 3839-3842.
176. Zhou, J. G.; Hagelberg, F. *Phys. Rev. Lett.* **2006**, *97*, 045505.

177. Cossaro, A.; Mazzarello, R.; Rousseau, R.; Casalis, L.; Verdini, A.; Kohlmeyer, A.; Floreano, L.; Scandolo, S.; Morgante, A.; Klein, M. L.; Scoles, G. *Science* **2008**, *321*, 943-946.
178. Mazzarello, R.; Cossaro, A.; Verdini, A.; Rousseau, R.; Casalis, L.; Danisman, M. F.; Floreano, L.; Scandolo, S.; Morgante, A.; Scoles, G. *Phys. Rev. Lett.* **2007**, *98*,.
179. Grönbeck, H.; Walter, M.; Häkkinen, H. *J. Am. Chem. Soc.* **2006**, *128*, 10268-10275.
180. Grönbeck, H.; Häkkinen, H.; Whetten, R. L. *J. Phys. Chem. C* **2008**, *112*, 15940-15942.
181. Grönbeck, H.; Häkkinen, H. *J. Phys. Chem. B* **2007**, *111*, 3325-3327.
182. Huang, W. J.; Sun, R.; Tao, J.; Menard, L. D.; Nuzzo, R. G.; Zuo, J. M. *Nat. Mater.* **2008**, *7*, 308-313.
183. Jiang, D.-e.; Luo, W.; Tiago, M. L.; Dai, S. *J. Phys. Chem. C* **2008**, *112*, 13905-13910.
184. Gao, Y.; Shao, N.; Zeng, X. C. *ACS Nano* **2008**, *2*, 1497-1503.
185. Walter, M.; Akola, J.; Lopez-Acevedo, O.; Jadzinsky, P. D.; Calero, G.; Ackerson, C. J.; Whetten, R. L.; Grönbeck, H.; Häkkinen, H. *Proc. Natl. Acad. Sci. USA* **2008**, *105*, 9157-9162.
186. Akola, J.; Walter, M.; Whetten, R. L.; Häkkinen, H.; Grönbeck, H. *J. Am. Chem. Soc.* **2008**, *130*, 3756.
187. Poirier, G.; Tarlov, M. *J. Phys. Chem.* **1995**, *99*, 10966-10970.
188. Poirier, G. E. *Langmuir* **1999**, *15*, 1167-1175.
189. Karpovich, D. S.; Blanchard, G. J. *Langmuir* **1994**, *10*, 3315-3322.
190. Wuister, S. F.; van Houselt, A.; de Mello Donegá, C.; Vanmaekelbergh, D.; Meijerink, A. *Angew. Chem. Int. Ed.* **2004**, *43*, 3029-3033.
191. Zhang, H.; Edwards, E. W.; Wang, D.; Möhwald, H. *Phys. Chem. Chem. Phys.* **2006**, *8*, 3288-3299.
192. Hautman, J.; Klein, M. *J. Chem. Phys.* **1989**, *91*, 4994 - 5001.
193. Siepmann, J. I.; McDonald, I. R. *Mol. Phys.* **1993**, *79*, 457-473.
194. Siepmann, J. I.; McDonald, I. R. *Mol. Phys.* **1992**, *75*, 255-259.
195. Siepmann, J. I.; McDonald, I. R. *Phys. Rev. Lett.* **1993**, *70*, 453-456.
196. Mizutani, W.; Ishida, T.; Tokumoto, H. *Appl. Surf. Sci.* **1998**, *132*, 792-796.
197. Vemparala, S.; Karki, B.; Kalia, R.; Nakano, A.; Vashishta, P. *J. Chem. Phys.* **2004**, *121*, 4323-4330.
198. Ryu, S.; Schatz, G. *J. Am. Chem. Soc.* **2006**, *128*, 11563-11573.
199. Mahaffy, R.; Bhatia, R.; Garrison, B. J. *J. Phys. Chem. B* **1997**, *101*, 771-773.
200. Marks, L. D. *Rep. Prog. Phys.* **1994**, *57*, 603-649.
201. Ascencio, J. A.; Gutiérrez-Wing, G.; Espinosa, M. E.; Martín, M.; Tehuacanero, S.; Zorrilla, C.; José-Ymacamán, M. *Surf. Sci.* **1998**, *396*, 349-368.
202. Jakubov, T. S.; Mainwaring, D. E. *Adsorption* **2008**, *14*, 727-732.
203. Rabani, E. *J. Chem. Phys.* **2002**, *116*, 258-262.
204. D. R. Lide (editor in chief), *Handbook of Chemistry and Physics*; CRC press: Boca Raton, USA, 76 ed.; 1995.
205. Barker, J.; Watts, R. *Chem. Phys. Lett.* **1969**, *3*, 144-145.
206. Martin, M. G.; Siepmann, J. I. *J. Am. Chem. Soc.* **1997**, *119*, 8921-8924.
207. Esselink, K.; Loyens, L.; Smit, B. *Phys. Rev. E* **1995**, *51*, 1560.

208. Snurr, R. Q.; Bell, A. T.; Theodorou, D. N. *J. Phys. Chem.* **1993**, *97*, 13742-13752.
209. Korgel, B. A.; Zaccheroni, N.; Fitzmaurice, D. *J. Am. Chem. Soc.* **1999**, *121*, 3533-3534.
210. Ellis, A. V.; D'Arcy-Gall, J.; Vijayamohan, K.; Goswami, R.; Ganesan, P. G.; Ryu, C.; Ramanath, G. *Thermochimica Acta* **2005**, *426*, 207-212.
211. Yin, Y.; Alivisatos, A. P. *Nature* **2005**, *437*, 664-670.
212. Peng, X.; Manna, L.; Yang, W.; Wickham, J.; Scher, E.; Kadavanich, A.; Alivisatos, A. *Nature* **2000**, *404*, 59-61.
213. Cho, K.-S.; Talapin, D. V.; Gaschler, W.; Murray, C. B. *J. Am. Chem. Soc.* **2005**, *127*, 7140-7147.
214. Peng, X. *Adv. Mater.* **2003**, *15*, 459-463.
215. Manna, L.; Milliron, D. J.; Meisel, A.; Scher, E. C.; Alivisatos, A. P. *Nat. Mater.* **2003**, *2*, 382-385.
216. Lu, W.; Fang, J.; Ding, Y.; Wang, Z. L. *J. Phys. Chem. B* **2005**, *109*, 19219-19222.
217. Wuister, S. F.; Swart, I.; van Driel, F.; Hickey, S. G.; de Mello Donegà, C. *Nano Lett.* **2003**, *3*, 503-507.
218. Talapin, D. V.; Rogach, A. L.; Mekis, I.; Haubold, S.; Kornowski, A.; Haase, M.; Weller, H. *Colloid Surf. A* **2002**, *202*, 145-154.
219. Qu, L.; Peng, X. *J. Am. Chem. Soc.* **2002**, *124*, 2049-2055.
220. Kalyuzhny, G.; Murray, R. W. *J. Phys. Chem. B* **2005**, *109*, 7012-7021.
221. Munro, A. M.; Plante, I. J.-L.; Ng, M. S.; Ginger, D. S. *J. Phys. Chem. C* **2007**, *111*, 6220-6227.
222. Ji, X.; Copenhaver, D.; Sichmeller, C.; Peng, X. *J. Am. Chem. Soc.* **2008**, *130*, 5726-5735.
223. Koole, R.; Schapotschnikow, P.; de Mello Donegà, C.; Vlugt, T. J. H.; Meijerink, A. *ACS Nano* **2008**, *2*, 1703-1714.
224. Wuister, S. F.; de Mello Donegà, C.; Meijerink, A. *J. Phys. Chem. B* **2004**, *108*, 17393-17397.
225. Aldana, J.; Lavelle, N.; Wang, Y.; Peng, X. *J. Am. Chem. Soc.* **2005**, *127*, 2496-2504.
226. Bullen, C.; Mulvaney, P. *Langmuir* **2006**, *22*, 3007-3013.
227. Munro, A. M.; Ginger, D. S. *Nano Lett.* **2008**, *8*, 2585-2590.
228. Puzder, A.; Williamson, A. J.; Zaitseva, N.; Galli, G.; Manna, L.; Alivisatos, A. P. *Nano Lett.* **2004**, *4*, 2361-2365.
229. Kilina, S.; Ivanov, S.; Tretiak, S. *J. Am. Chem. Soc.* **2009**, *131*, 7717-7726.
230. Csik, I.; Russo, S. P.; Mulvaney, P. *J. Phys. Chem. C* **2008**, *112*, 20413-20417.
231. Morgan, B. J.; Madden, P. A. *Phys. Chem. Chem. Phys.* **2007**, *9*, 2355-2361.
232. Rabani, E. *J. Chem. Phys.* **2001**, *115*, 1493-1497.
233. Schapotschnikow, P.; Pool, R.; Vlugt, T. J. H. *Comput. Phys. Commun.* **2007**, *177*, 154-157.
234. van Huis, M. A.; Kunneman, L. T.; Overgaag, K.; Xu, Q.; Pandraud, G.; Zandbergen, H. W.; Vanmaekelbergh, D. *Nano Lett.* **2008**, *8*, 3959-3963.
235. Wick, C. D.; Stubbs, J. M.; Rai, N.; Siepmann, J. I. *J. Phys. Chem. B* **2005**, *109*, 18974-18982.
236. Lubna, N.; Kamath, G.; Potoff, J. J.; Rai, N.; Siepmann, J. I. *J. Phys. Chem. B* **2005**, *109*, 24100-24107.
237. Todebush, P. M.; Liang, G.; Bowen, J. P. *Chirality* **2002**, *14*, 220-231.

238. Andersen, H. C., *J. Chem. Phys.* **1980**, *72*, 2384-2393.
239. Barker, J. A.; Watts, R. O. *Chem. Phys. Lett.* **1969**, *3*, 144-145.
240. Madras, N.; Sokal, A. D. *J. Stat. Phys.* **1988**, *50*, 109-186.
241. Schrier, J.; Wang, L.-W. *J. Phys. Chem. B* **2006**, *110*, 11982-11985.
242. Li, L.; Alivisatos, A. *Phys. Rev. Lett.* **2003**, *90*,.
243. Nann, T.; Schneider, J. *Chem. Phys. Lett.* **2004**, *384*, 150-152.
244. Shim, M.; Guyot-Sionnest, P. *J. Chem. Phys.* **1999**, *111*, 6955-6964.
245. Klokkenburg, M.; Houtepen, A. J.; Koole, R.; De Folter, J. W. J.; Ern , B. H.; Van Faassen, E.; Vanmaekelbergh, D. *Nano Lett.* **2007**, *7*, 2931-2936.
246. Dykij, J.; Svoboda, J.; Wilhoit, R. C.; Frenkel, M.; Hall, K. R. *Vapor pressure and antoine constants for nitrogen containing organic compounds*; Springer Verlag: New York, 2001.
247. Kinge, S.; Crego-Calama, M.; Reinhoudt, D. N. *Chem. Phys. Chem.* **2008**, *9*, 20-42.
248. Ederth, T. *Langmuir* **2001**, *17*, 3329-3340.
249. Wolf, M. G.; Jongejan, J. A.; Laman, J. D.; de Leeuw, S. W. *J. Am. Chem. Soc.* **2008**, *130*, 15772-15773.
250. Wolf, M. G.; Jongejan, J. A.; Laman, J. D.; de Leeuw, S. W. *J. Phys. Chem. B* **2008**, *112*, 13493-13498.
251. Vreede, J.; Wolf, M. G.; de Leeuw, S. W.; Bolhuis, P. G. *J. Phys. Chem. B* **2009**, *113*, 6484-6494.
252. Ciccotti, G.; Ferrario, M.; Hynes, J.; Kapral, R. *Chem. Phys.* **1989**, *129*, 241.
253. Gu rdia, E.; Rey, R.; Padr , J. *Chem. Phys.* **1991**, *155*, 187-195.
254. Jarzynski, C., *Phys. Rev. Lett.* **1997**, *78*, 2690-2693.
255. Jarzynski, C., *Phys. Rev. E* **1997**, *56*, 5018-5035.
256. Park, S.; Khalili-Araghi, F.; Tajkhorshid, E.; Schulten, K. *J. Chem. Phys.* **2003**, *119*, 3559-3566.
257. Park, S.; Schulten, K. *J. Chem. Phys.* **2004**, *120*, 5946-5961.
258. Schapotschnikow, P.; Pool, R.; Vlugt, T. J. H. *Mol. Phys.* **2007**, *105*, 3177-3184.
259. Trzesniak, D.; Kunz, A.-E.; Van Gunsteren, W. F. *Chem. Phys. Chem* **2007**, *8*, 162-169.
260. Bekker, H.; Dijkstra, E.; Renardus, M.; Berendsen, H. *Mol. Sim.* **1995**, *14*, 137-151.
261. Sigman Jr., M. B.; Saunders, A. E.; Korgel, B. A. *Langmuir* **2004**, *20*, 978-983.
262. Huang, S.; Minami, K.; Sakaue, H.; Shingubara, S.; Takahagi, T. *Langmuir* **2004**, *20*, 2274-2276.
263. Korgel, B. A.; Fullam, S.; Connolly, S.; Fitzmaurice, D. *J. Phys. Chem. B* **1998**, *102*, 8379-8388.
264. Martin, J. E.; Wilcoxon, J. P.; Odinek, J.; Provencio, P. *J. Phys. Chem. B* **2000**, *104*, 9475-9486.
265. von Ferber, C.; Jusufi, A.; Likos, C. N.; L wen, H.; Watzlawek, M. *Eur. Phys. J. E* **2000**, *2*, 311-318.
266. Dobnikar, J.; Brunner, M.; von Gr nberg, H. H.; Bechinger, C. *Phys. Rev. E* **2004**, *69*, 031402.
267. Russ, C.; von Gr nberg, H. H.; Dijkstra, M.; van Roij, R. *Phys. Rev. E* **2002**, *66*, 011402.
268. Terao, T. *Mol. Phys.* **2006**, *104*, 2507-2513.

Summary

The aim of this thesis is to study thermodynamic properties of *nanocrystals* (NCs) capped by organic ligands using molecular simulations. Nanocrystals are metallic or semiconductor crystallites of 2–10 nm size, consisting of hundreds to thousands of atoms. Due to their small size, they have unique properties that make them promising for various applications. Organic *ligands* are crucial for synthesis, stability and surface functionalization of nanocrystals. These ligands are, typically, linear molecules with a specific headgroup that binds to the NC and a hydrocarbon tail pointing outwards. Knowledge of microscopic properties such as interactions of capped NCs with each other and with the surrounding is essential for integration of NCs into novel materials and devices, especially when these devices are created by self-assembly. A brief survey of properties of nanocrystals, modeling in materials science, and molecular simulation techniques is given in Chapter 1.

In Chapter 2, we study the formation and structure of a capping layer composed from alkylthiol ligands on a gold NC and, for comparison, on a flat gold (111) surface. The questions we ask ourselves in this chapter are: (1) What are the similarities and differences between a monolayer of ligands on the surface of a tiny gold NC and on an extended flat (111) surface? (2) What is the role of a solvent? What do we lose if we ignore it in a simulation? (3) How can we exchange ligands in a capping layer? For studying the formation of a capping layer, we compute the *adsorption isotherms*: the number of adsorbed ligands as a function of ligand concentration at a fixed temperature. These isotherms provide an original tool for discovery in computer simulations. They reveal an intriguing phase behaviour on the flat gold (111) surface, which is fully absent on NCs due to the large surface curvature. This phase behaviour changes when a solvent is present. Two major solvent effects are: (1) competitive adsorption between ligands and solvent and (2) reduction of attractive interactions between aliphatic ligand tails. The surface curvature has major effects on the structure of the capping layer. On a flat Au (111) at ambient conditions, alkylthiols with more than six carbon atoms form *self-assembled monolayers* with both translational order of the headgroups on the surface and orientational order of the tails. However, on a curved NC surface, the translational order of headgroups is absent and they are packed much denser, and orientational order is frustrated and only present at low

temperatures. In systems dissolved in n-hexane, solvent layering is much stronger pronounced for a flat surface. Obviously, the solvent is able to penetrate into the capping layer on a NC at any coverage. We also study adsorption selectivity in a binary mixture of alkylthiols with different tail length. We find that the ligand with the longer tail is always preferred. This preferential adsorption is more pronounced on a flat surface than on a NC. Explicit solvent strongly reduces the selectivity, and for NCs in n-hexane the selectivity almost vanishes.

In Chapter 3, the attention is turned to semiconductor NCs. We study the commonly used cadmium selenide (CdSe) NCs. The origin and strength of interactions between these NCs and different ligands are currently poorly understood. When choosing a ligand for a specific application, experimentalists often have to rely on their intuition rather than profound knowledge. In this chapter, we shed some light on the following questions: (1) Why do the ligands bind to semiconductor NCs? (2) What does the bond strength depend on, and (how) is it possible to manipulate it? (3) How does the capping layer form (compared to, e.g., gold NCs from Chapter 2), and what is its influence on to the NC surface? We assemble a model from existing classical force fields for bulk materials without applying additional fitting of interaction parameters. The binding energies computed using this *ad hoc* approach are in a surprisingly good agreement with available quantum chemical calculations and experiments. The main contribution to the binding energy in our simulations originates from electrostatic interactions between partial charges of the ligand headgroup and anions and cations in the NC core. Thus, the binding energy always depends on the dielectric constant of a medium (such as a solvent used in an experiment). By correcting for this dielectric constant, a reasonable agreement with available experimental data is obtained. Not only do we validate our results, but we are also able to explain discrepancies between previous experimental and quantum chemical studies. We further investigate the formation of a hexylamine capping layer on CdSe NCs. As in Chapter 2, we do this by computing adsorption isotherms. This leads to several counterintuitive findings. The formation of a hexylamine capping layer occurs in two stages. In the first stage, the amines bind with the nitrogen atoms of their headgroups to surface Cd atoms. In the second stage, additional amines adsorb via a hydrogen bond with already adsorbed ligands. Although hydrogen bond formation is not surprising for these ligands, its effect on the capping layer formation has not been realized previously.

We return to gold nanocrystals capped by alkylthiols in Chapter 4. Knowledge on the details of the nanocrystal–nanocrystal interaction is of vital importance to derive a coarse-grained nanocrystal potential. Such a potential would allow the modelling of a large array of NCs to make predictions regarding their thermodynamic and mechanical properties. In Chapter 4, we develop such a potential from atomistic simulations, enabling its use in simulation studies of nanocrystal self-assembly and thus predict nanocrystal superstructure characteristics. Moreover, we study the dependence of the NC–NC interaction on several system parameters. The central finding is the scaling of the pair interaction: the equilibrium

distance in a pair of capped NCs is always ≈ 1.25 times the NC core diameter. This scaling is almost insensitive to polydispersity or to changes in temperature, NC size or ligand length. However, this relation breaks down for incomplete capping layers. We construct a geometric model (Overlap Cone Model) that explains the universal value of 1.25 based on ligand packing arguments. We also study triplets of NCs. Since the ligands require a certain space, it is not surprising that the equilibrium distance in a NC triplet becomes larger than in a pair of NCs, especially for long ligands. We find that a large energy penalty is associated with this increase in separation. This penalty can even be responsible for formation of NC chains instead of close-packed arrays. Based on the simulation results, we formulate the *Golden Rule*: a NC array will have an enhanced robustness if the distance between adjacent NCs is ≈ 1.25 times the NC core diameter. Combining our simulation and modeling results, we make predictions when the Golden Rule is actually obeyed. Thus, recommendations are made for the optimal choice of ligand for a desired NC superstructure. This is a small but important step towards rational computer-aided design of self-assembled structures.

Samenvatting

Nanokristallen zijn kristallen van een metaal of halfgeleider met een typische grootte van 2–10 nm. Omdat ze zo klein zijn hebben ze eigenschappen die heel anders zijn dan die van losse atomen of een bulkmateriaal. Organische liganden (capping moleculen) spelen een belangrijke rol tijdens de synthese en bij de stabilisering van nanokristallen. Kennis van de microscopische eigenschappen zoals de effectieve interacties van nanokristallen met elkaar en met de omgeving is van essentieel belang voor de toepassing van nanokristallen in nieuwe materialen, in het bijzonder wanneer deze materialen worden gemaakt door middel van zelf-assemblage. Het doel van dit proefschrift is het bestuderen van de thermodynamische eigenschappen van nanokristallen die met een laag organische moleculen zijn bedekt. Hiervoor worden moleculaire simulaties gebruikt. Een kort overzicht van de eigenschappen van nanokristallen, de verschillende manieren van modelleren in de materiaalkunde, en moleculaire simulatietechnieken wordt gepresenteerd in hoofdstuk 1.

In hoofdstuk 2 wordt de adsorptie en de structuur van een laag van alkylthiol moleculen aan goud nanokristallen en goud (111) oppervlakken bestudeerd. Hierbij spelen de volgende vragen een belangrijke rol: (1) Wat zijn de overeenkomsten en verschillen tussen een monolaag van liganden op het oppervlak van een klein nanokristal en op een vlak oppervlak? (2) Wat is de rol van een oplosmiddel? Welke details verliezen we als we het oplosmiddel negeren in een computersimulatie? (3) Hoe werkt de uitwisseling van liganden in een monolaag? Voor het bestuderen van de vorming van een monolaag werden *adsorptie isothermen* berekend; dit is het aantal geadsorbeerde liganden als functie van ligand concentratie in de bulk bij een constante temperatuur. Het is bijna onmogelijk om adsorptie isothermen experimenteel te meten voor deze systemen. Desondanks zijn berekende adsorptie isothermen een nuttig hulpmiddel om deze systemen te onderzoeken. Adsorptie isothermen onthullen een intrigerend fase gedrag van alkylthiolen op een vlak goud (111) oppervlak, dat op een nanokristal vanwege de grote kromming van het oppervlak volledig afwezig is. Dit fase gedrag verandert wanneer een oplosmiddel aanwezig is. Twee belangrijke effecten van het oplosmiddel zijn: (1) de concurrerende adsorptie tussen liganden en oplosmiddel en (2) de reductie van aantrekkende interacties tussen de staarten van de alifatische liganden. De kromming van het oppervlak heeft grote gevolgen voor de structuur van de laag van

capping moleculen. Op een vlak goud (111) oppervlak vormen alkylthiolen met meer dan zes koolstofatomen onder standaardomstandigheden *zelf-geassembleerde monolagen* met zowel translationele ordening van de kopgroepen op het oppervlak en oriëntationele ordening van de staarten. Op een gekromd oppervlak van een nanokristal is de translationele ordening van de kopgroepen grotendeels afwezig; ze zijn veel dichter gepakt en de oriëntationele ordening is gefrustreerd en alleen aanwezig bij lage temperatuur. Voor systemen met n-hexaan als oplosmiddel blijkt dat het oplosmiddel adsorbeert in lagen. Dit effect is veel sterker voor een vlak oppervlak dan voor een nanokristal. Het oplosmiddel is in staat om door te dringen in de capping laag van een nanokristal. De adsorptie-selectiviteit van een binair mengsel van alkylthiolen met verschillende staartlengtes werd bestudeerd. Het ligand met de langste staart wordt altijd bij voorkeur geadsorbeerd. Deze preferentiële adsorptie is meer nadrukkelijk aanwezig bij een vlak oppervlak dan op een nanokristal. Het toevoegen van een oplosmiddel in de simulaties vermindert de adsorptie-selectiviteit sterk; in het geval van nanokristallen omgeven door n-hexaan verdwijnt de adsorptie-selectiviteit vrijwel geheel.

In hoofdstuk 3 wordt de adsorptie van verschillende liganden op CdSe nanokristallen bestudeerd. De oorsprong en de sterkte van de interacties tussen deze nanokristallen en verschillende liganden zijn momenteel slecht begrepen. Om de sterkte van de adsorptie af te kunnen schatten moeten experimentalisten vaak vertrouwen op hun intuïtie. In dit hoofdstuk worden de volgende vragen onderzocht: (1) Waarom binden liganden om een halfgeleider nanokristal? (2) Waarvan hangt de bindingssterkte af, en (hoe) is het mogelijk om deze te manipuleren? (3) Hoe wordt de capping laag gevormd (in vergelijking met, bijvoorbeeld, de goud nanokristallen van hoofdstuk 2)? In de simulaties wordt een model gebruikt dat gebaseerd is op sterke elektrostatistische interacties tussen partieel geladen atomen van de liganden en de nanokristallen, alsmede zwakkere van de Waals interacties. Dit model werd niet ontwikkeld voor systemen bestaande uit nanokristallen en liganden. De berekende bindingsenergiën tussen de liganden en nanokristallen zijn in uitstekende overeenstemming met kwantummechanische en experimentele resultaten. De belangrijkste bijdrage tot de bindingsenergie in de simulaties komt van de elektrostatistische interacties tussen de kopgroepen van de liganden en de anionen en kationen in het nanokristal. Hierdoor is de bindingsenergie altijd afhankelijk van de diëlektrische constante van het medium (het oplosmiddel gebruikt in een experiment). Door te corrigeren voor deze diëlektrische constante wordt een goede overeenkomst met de beschikbare experimentele gegevens verkregen. Niet alleen worden hierdoor onze resultaten gevalideerd, maar hierdoor zijn ook verschillen tussen eerdere experimentele en kwantumchemische studies te verklaren. De vorming van een hexylamine capping laag op CdSe nanokristallen is bestudeerd. Zoals in hoofdstuk 2, wordt dit gedaan door het berekenen van adsorptie isothermen. Dit leidt tot een aantal tegenintuïtieve bevindingen. De vorming van een hexylamine capping laag gebeurt in twee stappen. In de eerste stap binden de stikstofatomen van de kopgroepen van de amines aan de Cd atomen van het oppervlak. In tweede stap adsorberen additionele aminen

via een waterstofbrug met reeds geadsorbeerd liganden. Hoewel de vorming van waterstofbruggen niet verwonderlijk is voor deze liganden is het effect ervan op de formatie van capping lagen nog niet eerder waargenomen.

In hoofdstuk 4 wordt de effectieve interactie tussen goud nanokristallen met een capping laag bestudeerd. Deze effectieve interacties zijn heel belangrijk om thermodynamische en mechanische eigenschappen van superstructuren bestaande uit nanokristallen te kunnen begrijpen. Het is verrassend dat de evenwichtsafstand tussen door alkylthiol beschermde nanokristallen niet van de lengte van het alkylthiol afhangt, maar altijd ongeveer gelijk is aan 1.25 keer de diameter van het nanokristal. Deze relatie is vrijwel onafhankelijk van de polydispersiteit, veranderingen in temperatuur, grootte van het nanokristal en lengte van het capping molecuul. Deze relatie gaat niet op indien de capping laag onvolledig is. Eveneens zijn de interacties tussen nanokristal drielingen bestudeerd. Omdat liganden een bepaalde ruimte vereisen is het niet verwonderlijk dat de evenwichtsafstand in een nanokristal drieling groter is dan die van een nanokristal paar, zeker voor lange liganden. Dit heeft een grote repulsieve interactie tot gevolg die zelfs kan leiden tot de vorming van ketens van nanokristallen in plaats van dicht gepakte structuren. Op basis van de resultaten van de simulaties kan de volgende zogenaamde *Gouden Regel* worden geformuleerd: een nanokristal-array zal een grotere robuustheid hebben als de afstand tussen aangrenzende nanokristallen ongeveer 1.25 maal de diameter van de kern van het nanokristal is. Het vergelijken van de resultaten van de simulaties en de Gouden Regel leidt tot een aantal interessante voorspellingen, bijvoorbeeld voor de optimale keuze van een ligand die nodig is voor de vorming van een bepaalde superstructuur van nanokristallen. Dit is een kleine maar belangrijke stap naar rationeel design van zelf-geassembleerde materialen.

Published Work

Chapter 2

- Schapotschnikow P, Pool R, Vlugt TJH “Selective adsorption of alkyl thiols on gold in different geometries” *Computer Physics Communications* 2007, Vol. 177, 154–157
- Pool R, Schapotschnikow P, Vlugt TJH “Solvent effects in the adsorption of alkyl thiols on gold structures: A molecular simulation study” *Journal of Physical Chemistry C* 2007, Vol. 111, 10201–10212
- Schapotschnikow P, Pool R, Vlugt TJH “Coarse-grained model for gold nanocrystals with an organic capping layer” *Molecular Physics* 2007, Vol. 105, 3177–3184 (Erratum in Vol.106, 963-964)

Chapter 3

Schapotschnikow P, Hommersom J, Vlugt TJH “Adsorption and binding of ligands to CdSe nanocrystals”, *Journal of Physical Chemistry C* 2009, Vol. 113, 12690–12698

Chapter 4

- Schapotschnikow P, Pool R, Vlugt TJH “Molecular simulations of interacting nanocrystals”, *Nano Letters* 2008, Vol. 8, 2930–2934
- Schapotschnikow P, Vlugt TJH “Understanding Interactions between Capped Nanocrystals: Three-Body and Chain Packing Effects”, *Journal of Chemical Physics* 2009, Vol. 131, 124705

Not included in this thesis

- Schapotschnikow P “Eigenvalue and nodal properties on quantum graph trees”, *Waves In Random And Complex Media* 2006, Vol. 16, 167–178
- Koole R, Schapotschnikow P, de Mello Donegà C, Vlught TJH, Meijerink A “Time-dependent photoluminescence spectroscopy as a tool to measure the ligand exchange kinetics on a quantum dot surface” *ACS Nano* 2008, Vol. 2, 1703–1714
- Schapotschnikow P, Gnutzmann S “Spectra of graphs and semi-conducting polymers”, in *Analysis On Graphs And Its Applications* (Editors: Exner P, Keating JP, Kuchment P, Sunada T, Teplyaev A), *Proceedings of Symposia in Pure Mathematics* 2008, Vol. 77, 691–705
- Schapotschnikow P, Vlught TJH “Soft hedgehogs on stiff carpets: A molecular simulation study of capped nanocrystals interacting with self-assembled monolayers of alkylthiols on Au (111) ”, submitted
- Schapotschnikow P, Gnutzmann S “Scaling of the HOMO-LUMO gap of conjugated oligomers derived from Molecular Orbital Theory”, in preparation
- Schapotschnikow P, van Huis MA, Vlught TJH, Zandbergen HW “Atomistic simulation study of bare and capped PbSe nanocrystals”, in preparation
- Zhao Y, Schapotschnikow P, de Mello Donegà C, Vlught TJH, Meijerink A “Time-dependent photoluminescence spectroscopy as a tool to measure the lipid exchange kinetics on a quantum dot micelle”, in preparation

Acknowledgments

First of all, I would like to thank my supervisor Dr. Thijs Vlugt. I really enjoyed working in your group for the last 3.5 years; and I learned a lot both from the scientific and from the private point of view. It was a brave decision to accept me for this PhD project, as I did not have any expertise in physical chemistry at all. Nevertheless, you did everything to make the start as smooth as possible, so that I could become productive after short time. I also appreciate a lot your engagement for me during the hard times of moving to Delft. In particular, I am very grateful that I was not forced to commute to Delft every day. My start would never be that smooth without Dr. René Pool. Thank you very much for explaining me all the details of the simulation work, for answering my nasty questions, for helping me to learn FORTRAN programming. And for the great fun we had working together (especially on the trip to Egypt).

I wish also to thank my collaborators on different projects. Rolf, Celso and Andries did the experiments on CdSe quantum dots with various ligands; my contribution to this project stimulated further work that resulted in Chapter 3 of this thesis. Tetsuya and Kourosh from the NRC Fuel Cell Research Institute in Vancouver for their kind invitation and the chance to learn about molecular simulations for fuel cell research. Orestis and Vlasis from Patras for their efforts to determine the structure of low-coverage self-assembled monolayers. Ahson, who brought me into simulations of capped nanorods. Marijn for the ongoing exciting work on PbSe quantum dots and for the pictures. At this point, I would also like to thank the students who decided to do their final projects under my supervision: Gaia, Ramon and Bob. It was a great opportunity for me, and I really learned a lot.

This work would be impossible without a healthy working environment. I am really indebted to all my office mates in these years: Bert, Linda, Konstantin and Mark in Utrecht; Shuai, Sukanya, Juan-Manuel, Xin, Elena and Kirill in Delft. The atmosphere was always friendly and professional; and it was a pleasure sharing the office with you guys. I am truly grateful to the Condensed Matter & Interfaces group at Utrecht University for their hospitality over the past two years. After the transition to Delft, I was still welcome to stay as an “academic visitor” for the remainder of my PhD project. This opportunity saved me a lot of travel to Delft, and enormously increased my productivity. In particular, I

would like to thank the Profs. Vanmaekelbergh and van der Eerden for fruitful discussions, and Stephan Zevenhuizen for his help with computers.

I would also like to thank my colleagues from the Process & Energy Department at the TU Delft for the nice working environment on the days when I was working in Delft. I would especially like to acknowledge my promoter Prof. Gross for his friendly attitude and interest in my research.

And of course I am endlessly grateful to my family, to my girl-friend Luba and to friends for their love and support.

Curriculum Vitae

The Author was born on 7.6.1982 in Odessa. In 1996 his family moved to Stuttgart, Germany. There he finished Karls gymnasium in 2000. In the same year, the Author began to study Mathematics for diploma with a minor in Chemistry at the Technische Universität München in Munich. He went for an Erasmus exchange program to Cardiff from October 2003 till September 2004. During this year, he successfully completed a Master program at the School of Computer Science; and in 2005 he graduated from Cardiff University with a Master of Philosophy degree. After returning from Cardiff in 2004, he continued his studies at TU Munich. The Author wrote his diploma thesis entitled "Spectra of Graphs and Semi-conducting Polymers" in Utrecht, in parallel with the work on the present PhD project. In 2008, he then graduated from TU Munich with distinction.

In May 2006, the Author began with the present PhD project at the Utrecht University, Condensed Matter & Interfaces group within the Debye Institute. He was transferred to TU Delft, Process & Energy Laboratory in October 2007, where his supervisor Thijs Vlugt received an associate professor position. Despite the technical and organizational problems during this transition, the research assignment was completed within three years, one year ahead of schedule. The results of the present thesis were presented by the Author at six major international conferences. The Fuel Cell Research Institute in Vancouver invited the author for a joint project, where he then went for two weeks in November 2008. The Author supervised three bachelor and one master project.